



# Excitonic processes and lasing in ZnO thin films and micro/nanostructures

Tashiro, Aika  
Adachi, Yutaka  
Uchino, Takashi

---

**(Citation)**

Journal of Applied Physics, 133(22):221101

**(Issue Date)**

2023-06-14

**(Resource Type)**

journal article

**(Version)**

Version of Record

**(Rights)**

© 2023 Author(s). Published under an exclusive license by AIP Publishing.  
This article may be downloaded for personal use only. Any other use requires prior permission of the author and AIP Publishing. This article appeared in Journal of Applied Physics 133, 221101 (2023) and may be found at at...




**(URL)**

<https://hdl.handle.net/20.500.14094/0100489945>



TUTORIAL | JUNE 08 2023

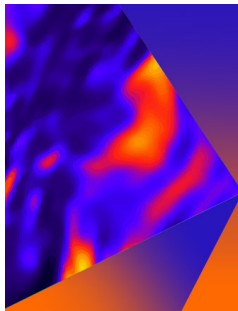
# Excitonic processes and lasing in ZnO thin films and micro/nanostructures FREE

Aika Tashiro; Yutaka Adachi ; Takashi Uchino  

 Check for updates

*J. Appl. Phys.* 133, 221101 (2023)

<https://doi.org/10.1063/5.0142719>



## Applied Physics Letters

Special Topic: Mid and Long Wavelength Infrared Photonics, Materials, and Devices

Submit Today



# Excitonic processes and lasing in ZnO thin films and micro/nanostructures

Cite as: J. Appl. Phys. **133**, 221101 (2023); doi: [10.1063/5.0142719](https://doi.org/10.1063/5.0142719)

Submitted: 16 January 2023 · Accepted: 19 May 2023 ·

Published Online: 8 June 2023



View Online



Export Citation



CrossMark

Aika Tashiro,<sup>1</sup> Yutaka Adachi,<sup>2</sup>  and Takashi Uchino<sup>1,a)</sup> 

## AFFILIATIONS

<sup>1</sup>Department of Chemistry, Graduate School of Science, Kobe University, Nada, Kobe 657-8501, Japan

<sup>2</sup>Optoelectronic Materials Group, Optical and Electronic Materials Unit, National Institute for Materials Science, Tsukuba, Ibaraki 305-0044, Japan

<sup>a)</sup>Author to whom correspondence should be addressed: [uchino@kobe-u.ac.jp](mailto:uchino@kobe-u.ac.jp)

## ABSTRACT

Low dimensional ZnO-based materials have drawn much attention for the past few decades due to their unique electronic and optical properties and potential applications in optoelectronic devices. In this Tutorial, we will cover the past and the latest developments in ZnO thin films and micro/nanostructures in terms of excitonic and related lasing processes. First, we give a brief overview of structural and band properties of ZnO along with the linear optical and excitonic properties. Second, we introduce a feedback mechanism for lasing in various forms of ZnO, ranging from nanoparticles to nanowires, nanodisks, and thin films. As for the feedback mechanism, detailed descriptions are given to random lasing, Fabry-Pérot lasing, and whispering gallery mode lasing. Third, we discuss possible gain mechanisms, i.e., excitonic gain and electron-hole plasma (EHP) gain, in ZnO. A special interest is also devoted to the Mott carrier density, which is a crucial parameter to distinguish between excitonic and EHP contributions to lasing. Lastly, recent developments on exciton-polariton lasers based on ZnO microcavities are introduced.

Published under an exclusive license by AIP Publishing. <https://doi.org/10.1063/5.0142719>

## I. INTRODUCTION

Since the middle of the last century, ZnO has received considerable interest for its interesting optical and electronic properties, such as a wide direct bandgap of 3.37 eV at room temperature and the native n-type conductivity.<sup>1,2</sup> In the early stage of the research, optical absorption, reflection, and emission characteristics have been extensively investigated using high-quality ZnO single crystals. It was revealed that ZnO exhibits various nonlinear phenomena under high electronic excitation, resulting in excitonic and electron-hole plasma (EHP) stimulated recombination processes, especially at cryogenic temperatures, as will be shown in detail in Secs. IV and V. In addition, its relatively high exciton binding energy  $E_X^b$  ( $E_X^b = 60$  meV)<sup>3,4</sup> allows us to anticipate the possibility of excitonic stimulated emission and lasing even at room temperature.

In the late 1990s and early 2000s, the progress of nanofabrication technologies enables the formation of a variety of ZnO-related micro/nanostructures, including epitaxial layers,<sup>5-8</sup> nanoparticles,<sup>9</sup> nanowires,<sup>10</sup> and quantum wells,<sup>11</sup> which allows us to observe room-temperature lasing with a narrow spectrum. Accordingly,

ZnO has attracted renewed and growing attention from the scientific community, leading to a remarkable recent progress in the field of nanowire photonics,<sup>12-14</sup> disordered photonics,<sup>15-17</sup> and polaritonic devices.<sup>18</sup>

The purpose of this Tutorial is to provide an overview of these past and upcoming fields such that readers may get a glimpse of the landscape of the excitonic processes and the related high-excitation phenomena including excitonic and EHP lasing in ZnO thin films and micro/nanostructures. The rest of the article is organized as follows. Section II reviews the basic structural and band properties of ZnO. Section III gives a brief explanation of the optical and excitonic properties. Sections IV and V discuss the feedback and gain mechanisms for lasing, respectively. Examples and recent developments of exciton-polariton lasers are provided in Sec. VI. Conclusions are given in Sec. VII. This Tutorial is by no means a comprehensive review on the structural, optical, and emission properties of ZnO micro/nanostructures, for which the readers are referred to existing and recent review articles<sup>2,19-26</sup> and books.<sup>27-30</sup>

07 June 2024 05:50:37

## II. BASIC STRUCTURAL AND BAND PROPERTIES

The ZnO wurtzite structure has a hexagonal unit cell with two lattice parameters,  $a$  and  $c$ , and belongs to the space group of  $C_{6v}^4(P6_3mc)$  [see Fig. 1(a)]. The lattice parameters have been extensively reported both experimentally<sup>31,32</sup> and theoretically,<sup>33,34</sup> as summarized in Table I, showing typical experimental values of 3.250 and 5.206 Å for  $a$  and  $c$ , respectively. The  $c/a$  parameter for the ideal hexagonal wurtzite structure has a value of 1.633. The  $c/a$  values obtained both experimentally and theoretically (see also Table I) are slightly lower than the ideal one due possibly to the ionicity of the ZnO crystal and the stability of the lattice.<sup>35</sup>

The electronic band structures of ZnO, which are nondegenerate at general  $k$  points for the Brillouin zone [see Fig. 1(b)], have been widely studied and reported in great detail.

The ZnO valence band structure probed by angle-resolved photoemission spectroscopy (ARPES)<sup>36</sup> in the  $\Gamma$ - $K$ - $M$  direction is shown in Fig. 2(a). A highly dispersive nature of the valence band is clearly recognized, showing the valence band maximum (VBM) at the binding energy  $E_B \sim -3.45$  eV. The observed valence band structure can be partitioned into three segments:<sup>36</sup> (i) the O- $p$  bands at  $-3.5$  eV  $< E_B < -7.5$  eV, (ii) the Zn- $s$ /O- $p$  band at  $-7.5$  eV  $< E_B < -9.5$  eV, which is formed due to hybridization between the empty  $s$  states of the Zn<sup>2+</sup> cation and the occupied  $p$  states of the O<sup>2-</sup> anion, and (iii) the Zn- $d$  bands at  $-10$  eV  $< E_B < -12$  eV.

To get more insight into the electronic band structure of ZnO, theoretical calculations are beneficial. From the density functional theory (DFT) point of view, however, the calculations of the band structure for ZnO are quite challenging. One of the difficulties arises from the presence of shallow Zn-3d states in ZnO, resulting in strong covalent hybridization with valence O-2p states.<sup>37</sup> The incomplete cancellation of self-interaction in DFT places all ZnO  $d$  bands too high in energy. Hence, the conventional DFT in its standard form with the local density approximation (LDA) leads to significantly underestimated (0.7–0.9 eV) bandgaps compared to typical experimental values at low temperatures ( $\sim 3.44$  eV<sup>19</sup>), and the position of the 3d cationic bands is about 3 eV higher than experimental results.<sup>38,39</sup> Recently, a rigorous and proven approach for calculating bandgaps of such computationally challenging systems as ZnO has been proposed through many-body perturbation theory or the GW approximation,<sup>37,40,41</sup> in which the electronic self-energy is written as a product of the Green's function  $G$  and the screened Coulomb interaction  $W$ .<sup>42,43</sup> Although the GW approach is not fully self-interaction free,<sup>36</sup> GW calculations can yield reasonable bandgaps and band structures comparable to experiments, as demonstrated in Figs. 2(a) and 2(b).<sup>36</sup> Note also that several other low computational cost methods including self-interaction-corrected pseudopotentials (SIC-PP),<sup>44</sup> a nonlocal semiempirical pseudopotential calculation (NL-EPM),<sup>45</sup> and the LDA + A-1/2 method,<sup>46</sup> which yield accuracy comparable to the state-of-the-art GW method, have also been proposed to calculate the band structures of ZnO.

We next take a closer look at the VBM at the  $\Gamma$  point. At the VBM, spin-orbit coupling (SOC) splits the atomic  $p$  level into two states, one being ( $j = 3/2$ ) fourfold and the other ( $j = 1/2$ ) doubly degenerate,<sup>47</sup> as shown in Fig. 3. The hexagonal crystal-field (CF)

further splits the  $j = 3/2$  level into two doubly degenerate states.<sup>47</sup> The resulting band edge structure results in three edges known as the A, B, C edges in order of increasing energy. Two of the three edges are characterized by  $\Gamma_7$  symmetry and the other by  $\Gamma_9$  symmetry. On the other hand, the lowest conduction state is of  $\Gamma_7$  symmetry. The transition from each of the A, B, C edges to the conduction band leads to the formation of three types of excitons, termed A-, B-, and C-excitons, respectively.

The ordering of the split levels below the VBM has been the subject of investigation for many years but is still a matter of controversy.<sup>35,48–50</sup> In most wurtzite crystals, the valence states are, in order of decreasing energy,  $\Gamma_9$ ,  $\Gamma_7$ , and  $\Gamma_7$  as observed for CdS and CdSe.<sup>47</sup> For ZnO, however, a reversed  $\Gamma_7$ - $\Gamma_9$ - $\Gamma_7$  ordering is proposed to occur due to a possible negative SOC.<sup>51–53</sup> Although some authors<sup>3,54–59</sup> still provide the interpretation and experimental signatures for the conventional  $\Gamma_9$ - $\Gamma_7$ - $\Gamma_7$  ordering, many of the experimental<sup>60–65</sup> and theoretical<sup>66–68</sup> studies support the reversed ordering. Note also that irrespective of the valence-band ordering, the A and B transitions are strongly dipole allowed for the electric-field vector perpendicular to the  $c$  axis ( $E \perp c$ ), whereas the C transition for light propagation parallel to the  $c$  axis ( $E \parallel c$ ), according to the symmetry selection rules.<sup>50,69</sup>

## III. OPTICAL AND EXCITONIC PROPERTIES

Optical and excitonic properties in ZnO have been investigated by various techniques, such as optical absorption,<sup>51,54,70</sup> optical reflection,<sup>3,4,51,54,56,60,71–74</sup> photoluminescence,<sup>4,75,76</sup> and cathodoluminescence spectroscopies.<sup>77,78</sup> In this section, we will focus on optical reflection, optical absorption, and photoluminescence properties, which are especially useful to characterize the band structures and related optical properties of semiconductors.

### A. Optical reflection

As mentioned in Sec. II, the polarization selection rules predict that A- and B-transitions are allowed for perpendicular polarization ( $E \perp c$ ), whereas C-transition for the parallel one ( $E \parallel c$ ) [see also Fig. 4(a)]. These three types of excitonic transitions were first observed from high-quality ZnO single crystals by Thomas<sup>51</sup> using reflection spectroscopy and later by many other researchers.<sup>3,4,54,56,58–60,71–74</sup> Figure 4(b) shows typical examples of low-temperature reflection spectra,<sup>58</sup> clearly showing changes in the reflectance depending on the polarization. The observed spectra are characterized by Lorentz-derivative-like shapes associated with A-, B-, and C-excitons, which are derived from band splitting under the action of CF and SOC interactions shown in Fig. 3. One also notices that the respective excitonic spectra demonstrate the signatures of the ground ( $n = 1$ ) and first excited ( $n = 2$ ) states. If it is assumed that the excitons have a hydrogen-like set of energy levels, the energy of the  $n$ th level relative to the ionization limit is given by<sup>50</sup>

$$E(n) = -\frac{E_x^b}{n^2}, \quad (1)$$

where  $n$  is an integer  $\geq 1$ . Hence, the exciton binding energy  $E_x^b$  can be obtained from the energy difference between the  $n = 1$  and  $n = 2$

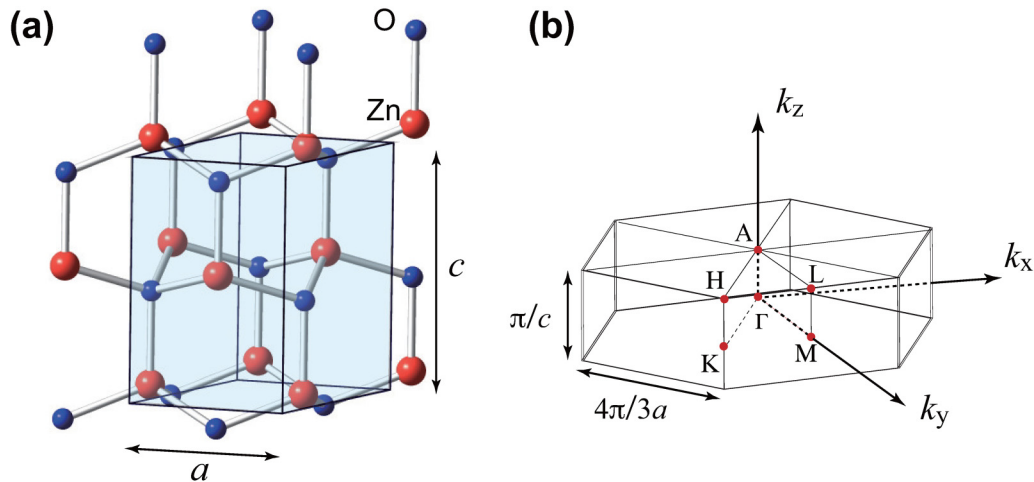


FIG. 1. (a) Crystal structure and (b) Brillouin zone of a wurtzite ZnO crystal.

states as follows:

$$E_x^b = \frac{4}{3}(E(2) - E(1)). \quad (2)$$

The observed energy difference,  $E(2) - E(1)$ , is practically the same ( $\sim 0.045$  eV<sup>3,4,56,59,72</sup>) for the A-, B-, and C- excitons, yielding a common value of  $E_x^b = 60$  meV for all three excitons. Using the reduced mass of exciton  $m_r^*$ , one can describe  $E_x^b$  as follows:<sup>51</sup>

$$\frac{1}{m_r^*} = \frac{1}{m_e^*} + \frac{1}{m_h^*}, \quad (3)$$

$$E_x^b = \frac{e^4 m_r^*}{2\hbar^2 (4\pi\epsilon_0\epsilon_r)^2} = 13.6 \frac{m_r^*}{m_0} \frac{1}{\epsilon_r^2} \text{ eV}, \quad (4)$$

where  $m_e^*$  ( $m_h^*$ ) is the electron (hole) effective mass,  $m_0$  is the free electron mass, and  $\epsilon_0$  and  $\epsilon_r$  are the dielectric constant of vacuum and the relative dielectric constant, respectively. Note that we use SI units throughout this tutorial. The static (or low-frequency) dielectric constant  $\epsilon_s$  ( $\epsilon_s \sim 8.5$ )<sup>79,80</sup> is often used as  $\epsilon_r$ .<sup>51</sup> However, it can

also be assumed that  $\epsilon_r$  is located in between  $\epsilon_s$  and a frequency  $\omega$  independent background dielectric constant  $\epsilon_\infty$  ( $\epsilon$  for  $\omega \rightarrow \infty$ ,  $\epsilon_\infty \sim 4$ <sup>80,81</sup>) as the polarization of the lattice may partially follow the motion of the electron and hole.<sup>82</sup> From  $E_x^b = 60$  meV and  $\epsilon_s = 8.5$  ( $\epsilon_\infty = 4$ ), one obtains a value of 0.32(0.07) for  $m_r^*/m_0$  from Eq. (4). It should be noted here that typical values of  $m_e^*$  and  $m_h^*$  are  $0.28m_0$  and  $0.59m_0$ , respectively.<sup>22,50</sup> It is hence most likely

07 June 2024 05:50:37

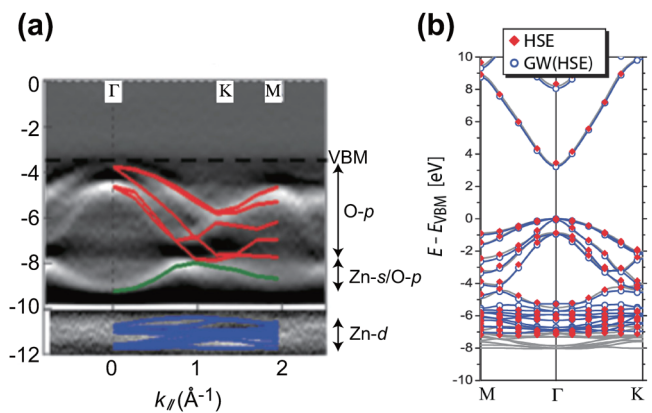


FIG. 2. (a) An example of angle-resolved photoemission spectroscopy (ARPES) measurements on a single crystalline Ga-doped ZnO (0001) sample (gray scale). The sample was kept at 100 K during the measurements. The theoretical band structure within the GW +  $V_d$ (GGA + U) scheme (red, green, and blue solid curves) below the valence band maximum (VBM) is also shown for comparison. (b) Comparison of ZnO band structures in different computational schemes. The gray band structure in the background shows the GW +  $V_d$ (GGA + U) result as a reference for the experimental band energies shown in (a). For the details of the computational schemes, see Ref. 36. Reproduced with permission from L. Y. Lim *et al.*, Phys. Rev. B **86**, 235113 (2012). Copyright 2012 the American Physical Society.

TABLE I. Experimental and theoretical lattice constants in wurtzite ZnO.

	$a$ (Å)	$c$ (Å)	$c/a$
Experiments	3.2497 <sup>a</sup>	5.206 <sup>a</sup>	1.602
	3.2496 <sup>b</sup>	5.2042 <sup>b</sup>	1.601
Theory	3.249 <sup>c</sup>	5.207 <sup>c</sup>	1.602
	3.249 <sup>c</sup>	5.232 <sup>d</sup>	1.616

<sup>a</sup>Ref. 31.

<sup>b</sup>Ref. 32.

<sup>c</sup>Ref. 33.

<sup>d</sup>Ref. 34.

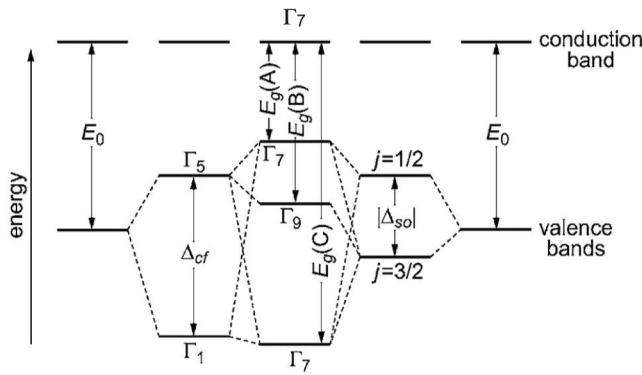


**FIG. 3.** Schematic energy-level diagram of band splitting under action of the crystal field ( $\Delta_{cf}$ , left) and spin-orbit ( $\Delta_{so}$ , right) interactions in wurtzite crystals, resulting in the reverse valence band ordering (middle). The gaps  $E_g(A)$ ,  $E_g(B)$ , and  $E_g(C)$  for A, B, and C excitons are indicated. Reproduced with permission from R. Laskowski and N. E. Christensen, *Phys. Rev. B* **73**, 045201 (2006). Copyright 2006 the American Physical Society.

that  $m_r^*/m_0$  lies around 0.19, meaning that  $\epsilon_r$  is estimated to be 6.56 from the relationship in Eq. (4). This  $\epsilon_r$  value is almost the middle between  $\epsilon_s \sim 8.5$  and  $\epsilon_\infty \sim 4$ , supporting the above assumption.

The hydrogen-like model also permits us to estimate the exciton Bohr radius in ZnO  $a_{\text{Bohr}}^{\text{ZnO}}$ ,<sup>51</sup> which is given as follows for  $m_r^* = 0.19m_0$  and  $\epsilon_r = 6.56$ :

$$a_{\text{Bohr}}^{\text{ZnO}} = \frac{4\pi\epsilon_0\epsilon_r\hbar^2}{m_r^*e^2} = \epsilon_r \frac{m_0}{m_r^*} a_{\text{Bohr}}^{\text{H}} = 1.83 \text{ nm}, \quad (5)$$

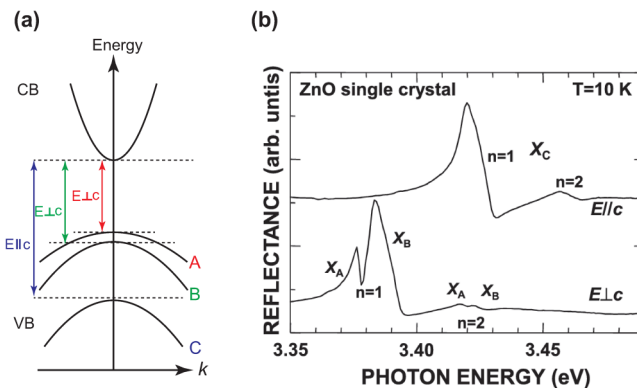


**FIG. 4.** (a) Schematic representation of conduction band (CB) and valence band (VB) of ZnO, showing the polarizations of the dominant transitions of A, B, and C excitons. (b) Representative polarized optical reflection spectra measured at 10 K for a high-quality bulk ZnO single crystal. Reproduced with permission from K. Hazu *et al.*, *J. Appl. Phys.* **111**, 093522 (2012). Copyright 2012 AIP Publishing LLC.

where  $a_{\text{Bohr}}^{\text{H}}$  is the hydrogen Bohr radius ( $a_{\text{Bohr}}^{\text{H}} = 0.053 \text{ nm}$ ). As will be shown in Sec. V, this value of  $a_{\text{Bohr}}^{\text{ZnO}}$  is somewhat, but not exactly, related to the Mott carrier density where the excitons cease to exist because of Coulomb-screening effects brought about by photogenerated electrons and holes.

## B. Optical absorption

The optical absorption spectra on ZnO single crystals yield excitonic features which are in good agreement with those obtained from reflection spectra in terms of the polarization characteristics and excitation energies.<sup>70</sup> Unlike the case of reflection measurements, however, the samples must be as thin as  $0.1 \mu\text{m}$  to obtain analyzable absorption spectra. Irrespective of this technical issue, there exists an advantage of the optical absorption spectroscopy in that the excitonic signatures can be clearly recognized from cryogenic to room temperature or above without substantially affected by thermal phonons.<sup>50,70,83</sup> It should be noted, however, that reports on the temperature dependence of the optical absorption spectra of ZnO are rather limited,<sup>70,84,85</sup> and no detailed and systematic temperature-dependent behavior of the excitonic absorptions has been published yet. Thus, in this Tutorial, we measured the temperature-dependent (5–300 K) optical absorption spectra of a ZnO thin film with a thickness  $d$  of 249 nm, which was grown by a pulsed laser deposition (PLD) method (for details, see the supplementary material), as shown in Fig. 5(a). The absorption spectrum measured at 5 K shows three major peaks at 3.371, 3.444, and 3.52 eV, in good agreement with those reported previously on single-crystal ZnO thin platelets grown by the vapor transport method.<sup>70</sup> One sees from the enlarged plot near the band edge [see the inset of Fig. 5(a)] that the peak at 3.371 eV is not symmetric, which is most likely due to the overlap of the A and B excitons.<sup>19,70</sup> The other high-energy peaks at 3.444 and 3.52 eV are attributed to exciton-one-phonon and exciton-two-phonon complexes, respectively,<sup>70</sup> although the C exciton may also contribute to the lower energy side of the 3.444-eV peak.<sup>19,70</sup> The appearance of the exciton-phonon complexes will ensure the high quality of the present PLD grown film. Since the excitonic absorptions are clearly identified in the low-temperature absorption measurement, the temperature-dependent change in the peak energy yields information about the temperature dependence of the bandgap energy, which is located above the A exciton peak by  $E_X^b = 60 \text{ meV}$ . Although similar information can be obtained from the temperature-dependent reflectance<sup>71</sup> and photoluminescence<sup>4,75</sup> spectra, the advantage of the optical absorption technique over the other methods is that the output data are directly used to identify the position of the free exciton peaks. In the present absorption spectra, the positions of the A and B excitons are not clearly resolved, as noted earlier. However, it can safely be assumed that the peak position of the 3.371-eV peak observed at 5 K represents that of the A exciton of our sample as this value is in reasonable agreement, within our spectral resolution ( $\sim 0.005 \text{ eV}$ ), with those reported previously for the free A-exciton in ZnO single crystals ( $FX_A^{n=1} = 3.3768\text{--}3.3781 \text{ eV}$ ).<sup>3,4,70</sup> Figure 5(b) shows the temperature-dependent variation of the A-exciton peak energy shown in Fig. 5(a). Although several equations have been proposed to represent the temperature dependence of the bandgap ( $E_g$ ) and free-exciton ( $E_{FX} = E_g - E_X^b$ ) energies in semiconductors,<sup>86–89</sup> we

07 June 2024 05:50:37

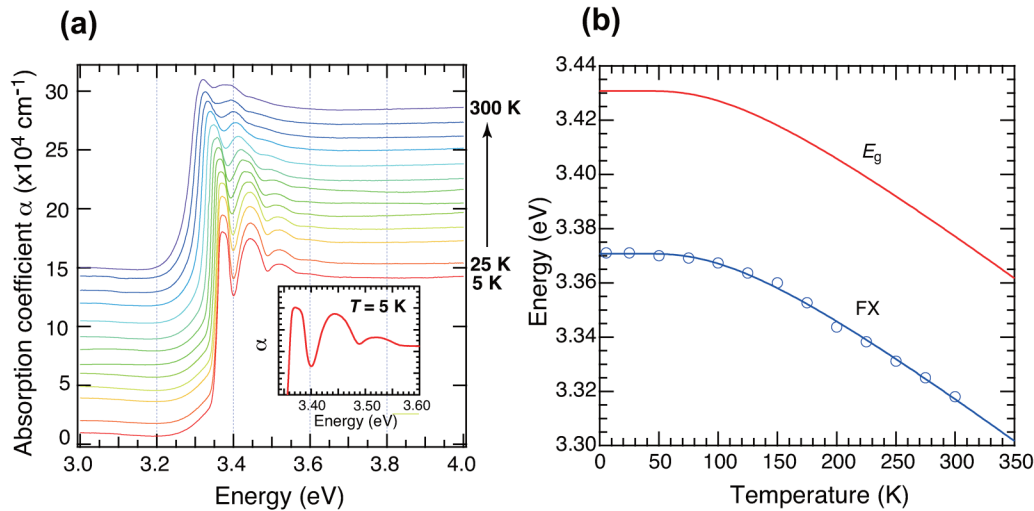


**FIG. 5.** (a) Absorption coefficient spectra for a 249-nm thick ZnO film measured at different temperatures from 5 to 300 K. In the temperature range from 25 to 300 K, spectra are shown in steps of 25 K. The inset shows a magnified view of the spectrum at 5 K. (b) Temperature-dependent change in the free exciton (FX) peak (blue open circles). The blue solid line represents the fit to Eq. (2). The red solid line is the temperature dependence of the bandgap  $E_g$  expected from Eq. (2) and  $E_X^0 = 60$  meV.

found that the observed temperature dependence can be best fitted to Bose–Einstein model,<sup>88</sup>

$$E_{\text{FX}}(T) = E_{\text{FX}}(0) - \frac{k}{\exp\left(\frac{\theta}{T}\right) - 1}, \quad (6)$$

rather than to the widely quoted Varshni formula,<sup>86</sup>

$$E_{\text{FX}}(T) = E_{\text{FX}}(0) - \frac{\alpha T^2}{T + \beta}, \quad (7)$$

where  $k$ ,  $\alpha$ , and  $\beta$  are the fitting constants and  $\theta$  is the parameter related to the average phonon frequency or the Einstein characteristic temperature. The fitted values of  $\theta$  and  $k$  in Eq. (6) are 349.4 K and 0.118, respectively, which are comparable to those obtained by photoluminescence<sup>71</sup> ( $\theta = 380$  K and  $k = 0.177$ ) and photoluminescence excitation<sup>90</sup> (240 K and  $k = 0.09$ ) measurements. From these fitted parameters in Eq. (6) and  $E_X^0 = 60$  meV, we can estimate the temperature dependence of the bandgap  $E_g(T)$ , as shown in the red solid curve in Fig. 5. This estimation yields the bandgap of 3.377 eV at 300 K, in reasonable agreement with the most accepted bandgap of  $\sim 3.37$  eV at room temperature.<sup>19</sup> This allows us to confirm that the measurement of optical absorption spectra is useful and effective to obtain the temperature dependence of the bandgap in ZnO.

### C. Photoluminescence

Photoluminescence (PL) of ZnO is very rich in structure and depends strongly on the size, shape, crystallinity, impurity, and surface states of the sample of interest. Although its surface sensitive nature often complicates the interpretation of the resulting PL spectra, it can

become a powerful method to assess surface phenomena and can be exploited for sensing applications, e.g., PL-based biosensors.<sup>91,92</sup>

The PL emissions of ZnO are usually categorized into two energy regimes: near band edge (NBE) ultraviolet (UV) and deep-level visible emissions. In the NBE UV spectral region, ZnO single crystals exhibit a number of emission lines, when probed at low temperatures, due not only to free exciton (FX) states, e.g., A- and B-excitons, but also to bond-exciton states, two electron satellite transitions of shallow bound excitons, and donor–acceptor pair recombinations (Fig. 6).<sup>4,19,49,93,94</sup> As for ZnO nanostructures, one also finds emissions of surface excitons (SX),<sup>95–97</sup> along with the controversial PL peak at 3.31 eV (Fig. 7, for details see Refs. 98–102). Respective UV emission peaks are often accompanied by longitudinal optical (LO) phonon replicas with an energy separation of  $\hbar\omega_{\text{LO}} \sim 72$  meV<sup>98–103</sup> (Figs. 7 and 8).

In general, the PL of the donor-bound excitons is the most intense PL band for temperatures  $T < \sim 10$  K, while the PL of the FX tends to dominate the spectrum at higher ( $T > \sim 200$  K) temperatures<sup>4,19,102,103</sup> (Figs. 7 and 8). These temperature-dependent changes in the PL spectra result from thermal activation of the donor-bound excitons into excited states where they behave as free excitons. Accordingly, at room temperature one finds one broad PL band due to the line broadening of the FX peak and its  $m\text{LO}$ -phonon ( $m = 1, 2, \dots$ ) replicas.<sup>104</sup> Typically, at room temperature, the NBE UV peak of ZnO films and nanostructures is located in the energy range from 3.15 to 3.30 eV,<sup>20,102,103,105–111</sup> whereas the bulk ZnO single crystal shows NBE PL emission peaking at 3.30–3.31 eV.<sup>22,104–110</sup> These NBE PL energies are slightly lower than the free exciton absorption energy obtained from the absorption measurement of ZnO at 295 K (3.32 eV),<sup>70</sup> as also shown in Fig. 5. This confirms that at room temperature, the spectral shape of the FX PL band is substantially affected by the presence of LO phonon replicas<sup>112</sup> and/or the effect of reabsorption.<sup>2,50</sup>

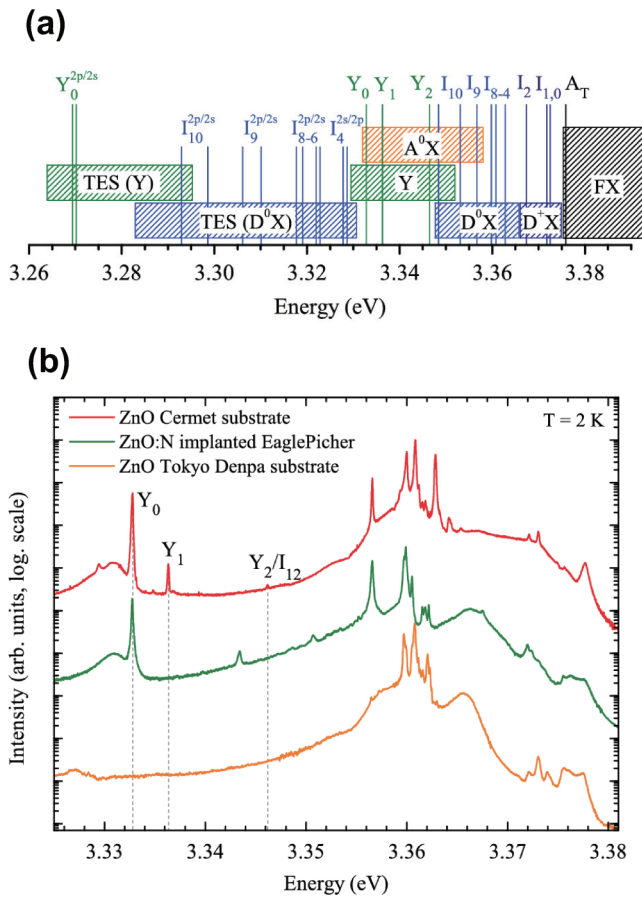


**FIG. 6.** (a) Schematic drawing of the energy ranges of various optical transitions of ZnO at low temperature. Selected transitions are indicated by vertical lines. The different areas mark the energy range of free excitons (FX), ionized donor bound excitons ( $D^+X$ ), neutral donor bound excitons ( $D^0X$ ), acceptor bound excitons ( $A^0X$ ), deeply bound excitons (Y), and two electron satellites (TES) of shallow and deeply bound excitons in their 2s and 2p states. (b) PL spectra of different ZnO crystals at  $T = 2$  K. Several narrow emission lines are visible in the spectral range 3.33 and 3.35 eV. The strongest peaks are the  $Y_0$  and the  $Y_1$  lines. The spectra are vertically shifted and normalized to the dominant bound exciton line. Reproduced with permission from M. R. Wagner *et al.*, Phys. Rev. B **84**, 035313 (2011). Copyright 2011 the American Physical Society.

The defect and impurity states in ZnO yield deep-level emission bands in the visible spectral region, showing blue, green, yellow, and orange/red PL bands.<sup>19,20</sup> There have been a huge number of studies on the emission properties of these deep-level PL bands, which are still a matter of intensive research.<sup>113–120</sup> The existence of deep-level emissions will have a negative effect on the stimulated emission although the ratio of the visible emission to the NBE emission decreases as the excitation density increases.<sup>108,121</sup> We do not give details here; the interested reader should consult Refs. 19, 20, 76, 92, and 122 for a review on the deep-level emissions in ZnO.

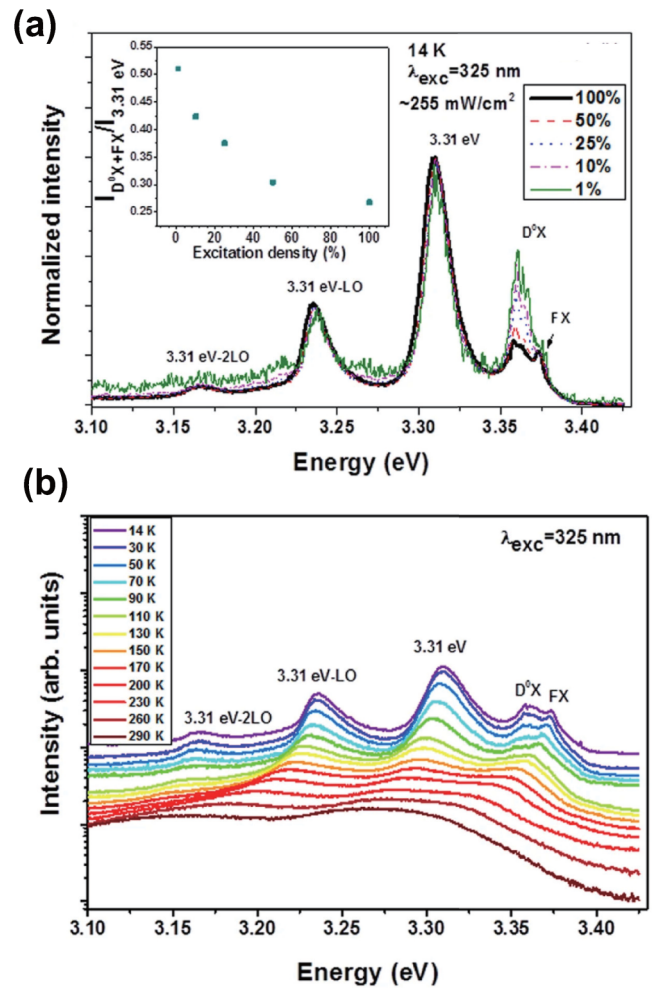


**FIG. 7.** (a) Excitation density dependence of the near band edge emission of the ZnO microrods recorded at 14 K. The inset depicts the ratio between the  $D^0X + FX$  and 3.31 eV emission intensity as a function of excitation power. (b) Temperature dependence of the near band edge emission. Reproduced with permission from J. Rodrigues *et al.*, Sci. Rep. **5**, 10783 (2015). Copyright 2015 Author(s), licensed under a Creative Commons Attribution (CC BY) Licence.

#### IV. FEEDBACK MECHANISM FOR LASING

The laser has had a tremendous impact on many different areas of science, including physics, chemistry, astronomy, biology, and medicine. Since the first demonstration of the laser in 1960, great progress in improving the extent of the spatial and temporal coherence of laser light has been made. Research is ongoing, especially in terms of the lasers with complex light patterns.<sup>123–126</sup> In general, three core elements are necessary for making a laser; that is, gain medium, a means to excite it, and an optical resonator for optical feedback. In ZnO-based laser, ZnO itself behaves both as a gain medium and as a resonator. It should be noted that its dimension and size are highly



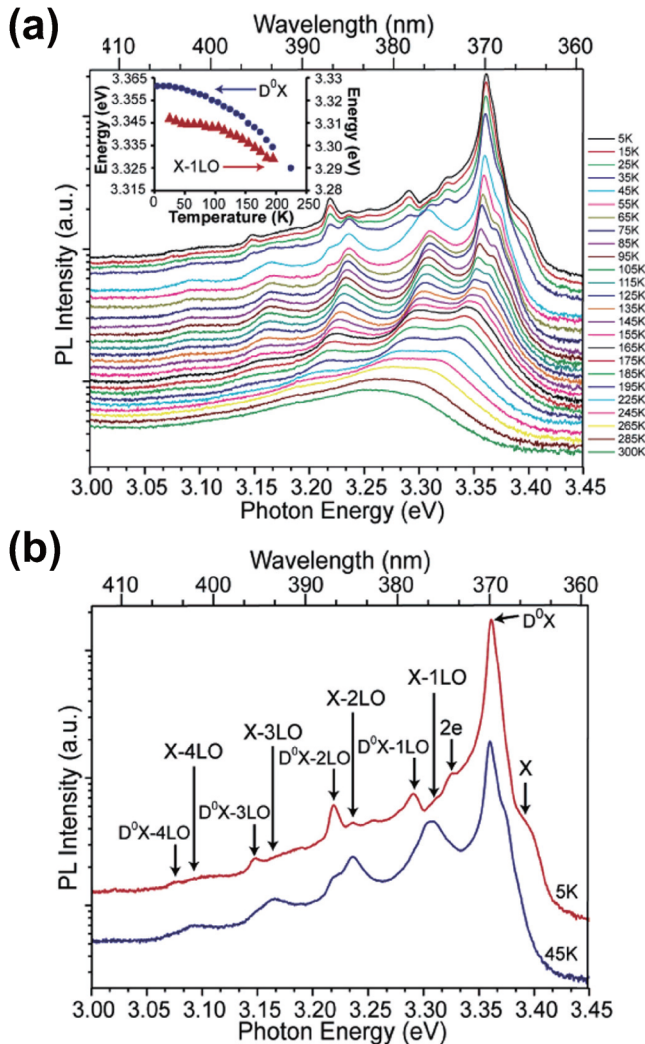


**FIG. 8.** (a) Log plot of the band edge emission of a single ZnO nanowire as a function of temperature (pump power  $\sim 50 \text{ W cm}^{-2}$ ). The inset plots the donor bound ( $D^0X$ ) and first-order free-exciton phonon replica (X-1LO) peaks as a function of temperature. (b) Zoom in of the 5 and 45 K spectra showing the excitonic fine structure. Reproduced with permission from D. J. Siribuly *et al.*, *J. Phys. Chem. B* **109**, 15213 (2005). Copyright 2005 American Chemical Society.

versatile, including nanoparticle, nanowire, nanoribbon, and thin film. Accordingly, two principal feedback mechanisms, i.e., random lasing and microcavity lasing, are observed in ZnO micro/nanostructures depending on their morphologies.

### A. Random lasing

As mentioned above, an optical resonator is one important element in achieving laser action. An optical resonator or cavity is a system in which light at certain frequencies is continuously reflected back and forth without escaping, building up power in the process.<sup>127</sup>

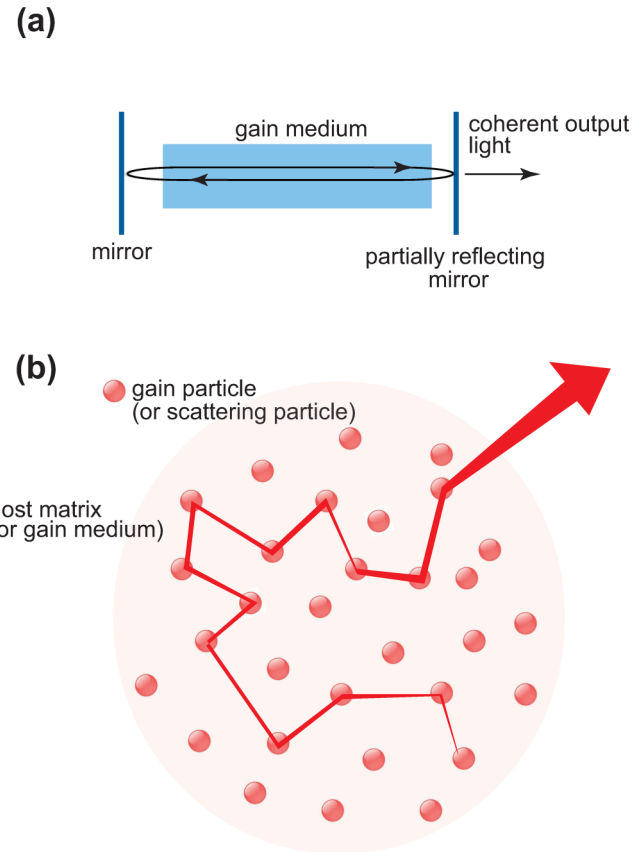


**FIG. 9.** Schematic illustration of two different feedback mechanisms: (a) a conventional Fabry-Pérot resonator, (b) a random laser cavity.

For this purpose, a two-mirror cavity is conventionally employed [Fig. 9(a)]. In random lasers, however, a completely different feedback mechanism, i.e., multiple scattering, is used to realize optical feedback [Fig. 9(b)]. Thus, random lasers, along with recently emerged plasmon lasers<sup>128</sup> and topological lasers,<sup>129,130</sup> have been considered a paradigmatic phenomenon of laser systems, opening up a new perspective in the photonics in disordered media.<sup>124,131–136</sup> During the last several decades, random lasing action has been demonstrated in a variety of random media, as described in recent review articles.<sup>137–140</sup> Among other experiments on random lasers, the results reported by the group of Cao *et al.* on ZnO polycrystalline films<sup>141</sup> and nanoparticles<sup>9,142</sup> are worth mentioning, in that they first observed the narrow and intense lasing peaks with the linewidth less than 0.3 nm under pulsed laser pumping (Fig. 10). These phenomena give evidence for the light amplification through a coherent feedback of the interference effects, hence stimulating further investigations into random lasers and related disordered photonics<sup>16,143</sup> in terms, for example, of mode localization and interaction,<sup>144–146</sup> mode-locking,<sup>147,148</sup> and controlling directionality.<sup>149</sup>

In discussing the nature of light scattering in a three-dimensional (3D) system, it is useful to define the following length scales (Fig. 11):<sup>131</sup>

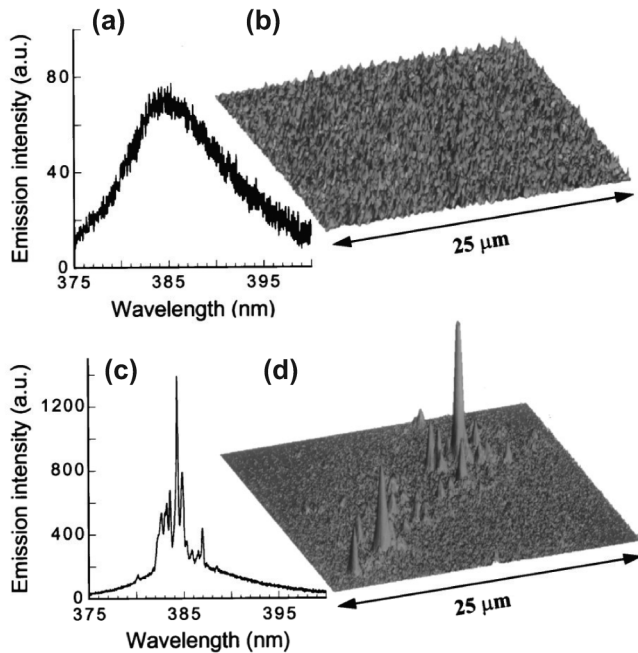


**FIG. 10.** Random laser action from a ZnO powder film at different pump power. [(a) and (c)] The measured spectra of emission. [(b) and (d)] The measured spatial distribution of emission intensity in the film. The incident pump pulse energy is 5.2 nJ for (a) and (b) and 12.5 nJ for (c) and (d). Reproduced with permission from H. Cao *et al.*, Phys. Rev. Lett. **84**, 5584 (2000). Copyright 2000 the American Physical Society.

*Scattering mean free path* ( $l_s$ )—an average distance that photons travel between two successive scattering events.

*Transport mean free path* ( $l_t$ )—an average distance over which the direction of propagation of waves is randomized by scattering.

*Gain length* ( $l_g$ )—a distance over which the intensity optical signal is amplified by a factor  $e \approx 2.72$  in a gain medium without scattering.

*Amplification length* ( $l_a$ )—a root mean square distance between the beginning and ending point for paths of length  $l_g$  in a gain medium with scattering. In the limit without scattering,  $l_a = l_g$ . In the presence of scattering,  $l_a$  becomes shorter than  $l_g$ , leading to a higher effective gain coefficient.

The above length scales are related to each other as follows:

$$l_t = \frac{l_s}{1 - \langle \cos\theta \rangle}, \quad (8)$$

$$l_a = \sqrt{\frac{l_t l_g}{3}}, \quad (9)$$

where  $\langle \cos\theta \rangle$  is the average cosine of the scattering angle.

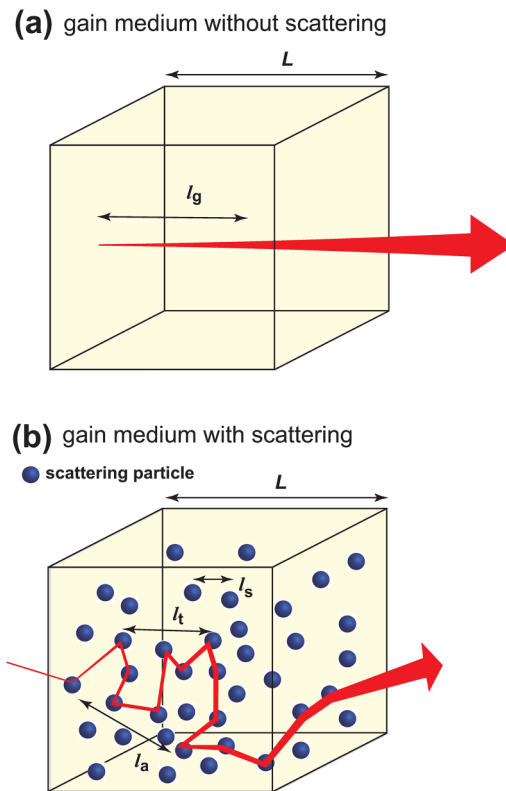


**FIG. 11.** Light propagation in a three-dimensional gain medium with length of  $L$  (a) without and (b) with scattering. In (a), gain length  $l_g$  is defined as a distance that optical signal has to travel to achieve amplification by a factor of  $e \approx 2.72$ . In (b), scattering mean free path  $l_s$ , transport mean free path  $l_t$ , and amplification length  $l_a$  are schematically shown.

Depending on the relative magnitude of these characteristic length scales, scattering phenomena of light with wavelength  $\lambda$  in 3D medium with size  $L$  can be classified into three regimes: (i) the ballistic regime,  $L < l_s$ , (ii) the diffusive regime,  $\lambda < l_t < L$ , and (iii) the localization regime,  $l_s < \lambda$ . Practically, light scattering in the diffusive and localization regimes is a main concern for both experimentalists and theorists.

### 1. Localization regime

In the localization regime, strong photon localization in confined space can be realized. This is analog to the electronic Anderson localization proposed by Philip Anderson<sup>150</sup> to explain the metal-insulator transition in condensed matter systems. Although Anderson-like light localization was once recognized as one potential mechanism for the narrow laser spikes observed in random laser systems, no such light localization in the sense of an Anderson localization has been realized in ZnO nanoparticle-based random lasers, as will be shown in Subsection IV A 2. Generally, Anderson-like light localization requires a special design of scattering media, such as 2D<sup>151</sup> or 3D<sup>152</sup> photonic crystals, a disordered

07 June 2024 05:50:37

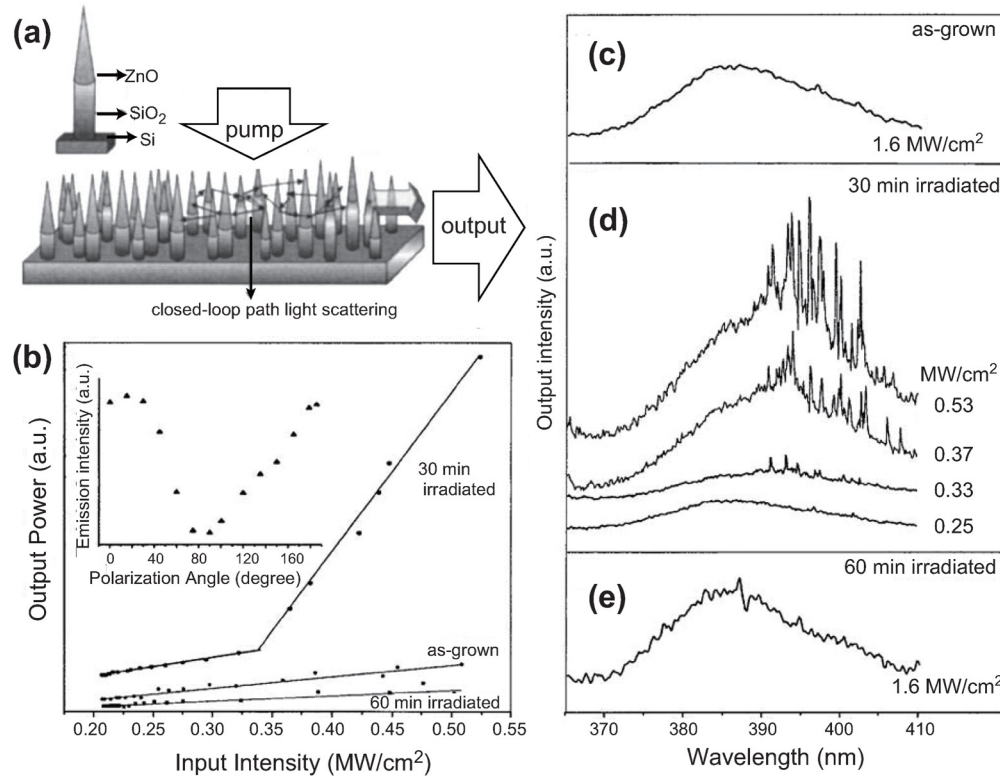


**FIG. 12.** (a) Schematic diagram of the laser measurement setup for the ZnO nanoneedle arrays. (b) Light-light curves of the samples after various ion irradiation times. The inset shows the maximum emission intensity of the TE mode as a function of polarization angles. (c) Emission spectrum of the as-grown ZnO thin film under a pump power of  $1.6 \text{ MW cm}^{-2}$ . (d) Evolution of emission spectra of the 30-min irradiated sample under different pump intensities. (e) Emission spectrum of the sample irradiated for 60 min under a pump power of  $1.6 \text{ MW cm}^{-2}$ . Reproduced with permission from S. P. Lau *et al.*, *Appl. Phys. Lett.* **87**, 013104 (2005). Copyright 2005 AIP Publishing LLC.

07 June 2024 05:50:37

photonic-crystal waveguide,<sup>153</sup> a planar nanophotonic network,<sup>154</sup> and a randomly spaced air-grooves,<sup>155</sup> to satisfy the condition  $l_s < \lambda$ .

## 2. Diffusive regime

As noted earlier, random lasing spikes were first observed in ZnO polycrystalline films<sup>141</sup> and nanoparticles<sup>9,142</sup> with particles sizes of 50–150 nm (Fig. 10). The demonstration of the sharp lasing spikes indicates that the observed lasing behavior arises from resonant (coherent) feedback.<sup>131,134</sup> These ZnO nanoaggregates are especially suitable for resonant feedback due to their relatively high refractive index of  $\sim 2.3$  in the near band edge region, providing efficient scattering for coherent random lasing. In addition to ZnO nanoparticle, ZnO nanoneedle arrays (the diameter of the stem part is  $\sim 100$  nm) grown perpendicular to a planar substrate have been shown to demonstrate sharp lasing spikes due to in-plane light scattering (Fig. 12).<sup>156</sup> It should be noted that in closely packed monodisperse ZnO powders with size  $d$  of  $\sim 140$  nm, the transport mean free path  $l_t$  is estimated to be  $1.2 \mu\text{m}$  for  $\lambda = 400$  nm.<sup>157</sup> When  $d$  decreased,  $l_t$  further increased. Thus, the light scattering responsible for the random lasing spikes in the ZnO

particles will not occur in the localized regime ( $l_s < \lambda$ ) but in the diffusive regime ( $\lambda < l_t < L$ ). In the diffusive regime, the optical modes are expected to be broad and overlap spectrally and spatially. The resulting feedback would be nonresonant, and hence the emission spectrum will narrow continuously toward the center of the gain spectra with increasing pumping intensity,<sup>131,133</sup> generally resulting in the amplified spontaneous emission (ASE). ASE is a light emission process in which spontaneously emitted photons are amplified by stimulated emission as they travel through a gain medium without coherent feedback.<sup>158</sup> Such incoherent random lasing was indeed observed in powders of  $\text{NdAl}_3(\text{BO}_3)_4$ ,  $\text{NdSc}_3(\text{BO}_3)_4$ , and  $\text{Nd:Sr}_5(\text{PO}_4)_3\text{F}$  laser crystals<sup>159</sup> and  $\text{LiF}$ <sup>160</sup> and  $\text{MgO}$ <sup>161–163</sup> powders with color centers. Therefore, it has been an open question as to why narrow coherent lasing spikes are observed in diffusive ZnO particle systems, and different scenarios have been proposed for the origin. One is a model based on the formation of ring-shaped resonators with the index of refraction larger than average, leading to local cavities (local modes).<sup>164,165</sup> Another is a model based on the formation of open modes where spontaneously emitted photons accumulate gain along very long trajectories.<sup>166,167</sup> The resulting “lucky photons” accumulate enough gain to activate a

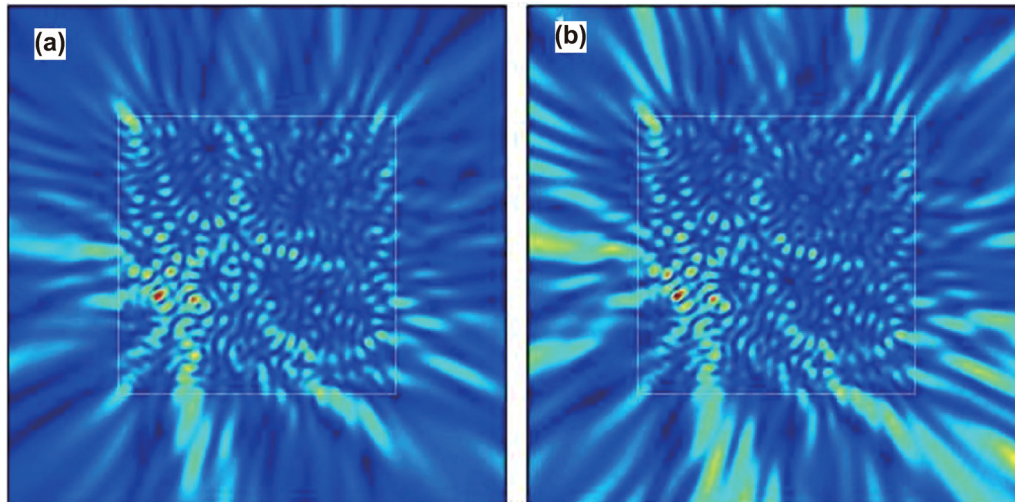


**FIG. 13.** (a) Spatial distribution of the amplitude of a lasing mode in the diffusive regime. (b) Spatial distribution of the field amplitude after the pump has been stopped and the polarization term has been set to zero. The system consists of 896 circular scatterers contained in a square box of size  $L = 5 \mu\text{m}$  and optical index  $n = 1$ . The radius  $r$  and  $n$  of the scatterers are  $r = 60 \text{ nm}$  and  $n = 1.25$ , respectively. Reproduced with permission from J. Andreasen *et al.*, *Adv. Opt. Photonics* **3**, 88 (2011). Copyright 2011 Optical Society of America.

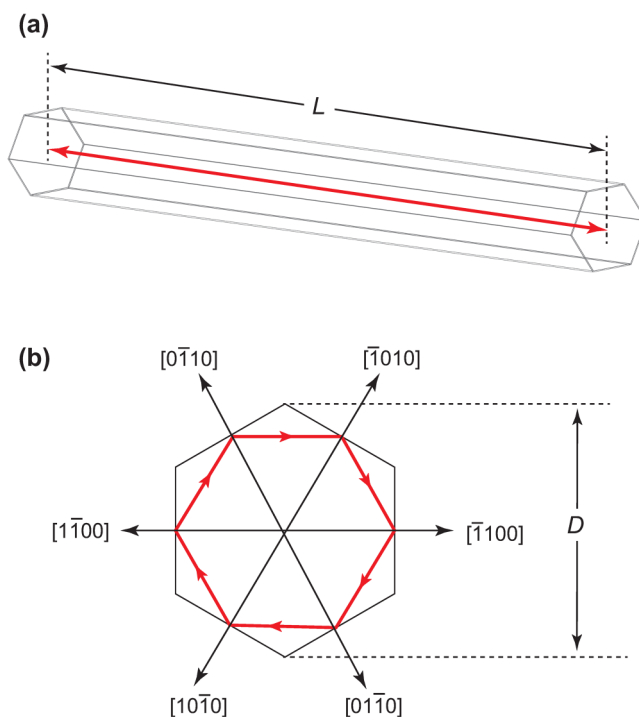


**FIG. 14.** Schematic illustration of (a) a Fabry-Pérot nanowire cavity and (b) a hexagonal whispering gallery mode cavity.

new lasing mode with a different wavelength after each excitation shot, giving rise to random spikes in the emission spectrum. Later, it has been found from a full solution of Maxwell's equations including a polarization term due to the atomic population inversion that even in the diffusive and weak scattering regimes, modes expand over the whole sample and overlap both spatially and spectrally (Fig. 13), leading to resonant feedback with spectrally narrow emission.<sup>168,169</sup> It is, hence, of interest to investigate which mode, local or open mode, is responsible for the lasing spikes observed in diffusive random systems. The answer to this question is not straightforward and will depend strongly on the experimental system. As far as the ZnO nanoparticle powders are concerned, Fallert and co-workers<sup>170</sup> have demonstrated that strongly localized random lasing modes co-exist with modes of much larger spatial extension. They<sup>170</sup> have shown that the extended modes are primarily found in the spectral region where the gain is expected to be highest, whereas the strongly localized modes are found in regions where the available gains are lower. This observation is consistent with the prediction that localized modes have a lower loss rate than that of extended modes.<sup>134</sup> Hence, it is most likely that both extended and localized modes in diffusive random systems can contribute to the occurrence of narrow lasing spikes. The relative dominance of these two modes will be governed by the spatial distribution of gain and loss in the random system of interest.

## B. Microcavity lasing

One of the biggest advantages of ZnO is that it can be grown in the shape of optical cavity, including nanorods, nanowires, nanoribbons, nanocombs, nanosaws, and nanotetrapods.<sup>171–173</sup> These intriguing ZnO micro/nanostructures can be prepared by both gas-phase<sup>174–178</sup> and solution-phase<sup>179–184</sup> methods. Among

other techniques, the vapor-liquid-solid (VLS) growth method has achieved the most success in producing optical cavities in relatively large quantities.<sup>174–176</sup> As for microcavity lasing, 1D microrod and 2D microdisk structures are of particular interest.<sup>12,103,185,186</sup> In microcavity lasers, the micro/nanostructure itself acts both as an optical cavity and as a gain medium, providing an ideal experimental platform for the development of miniature-cavity-based optoelectronic devices.<sup>187–189</sup> Depending on the resonant cavity structures, microcavity lasing can be classified into two groups. The first is Fabry-Pérot (F-P) lasing observed in nanorods [Fig. 14(a)]

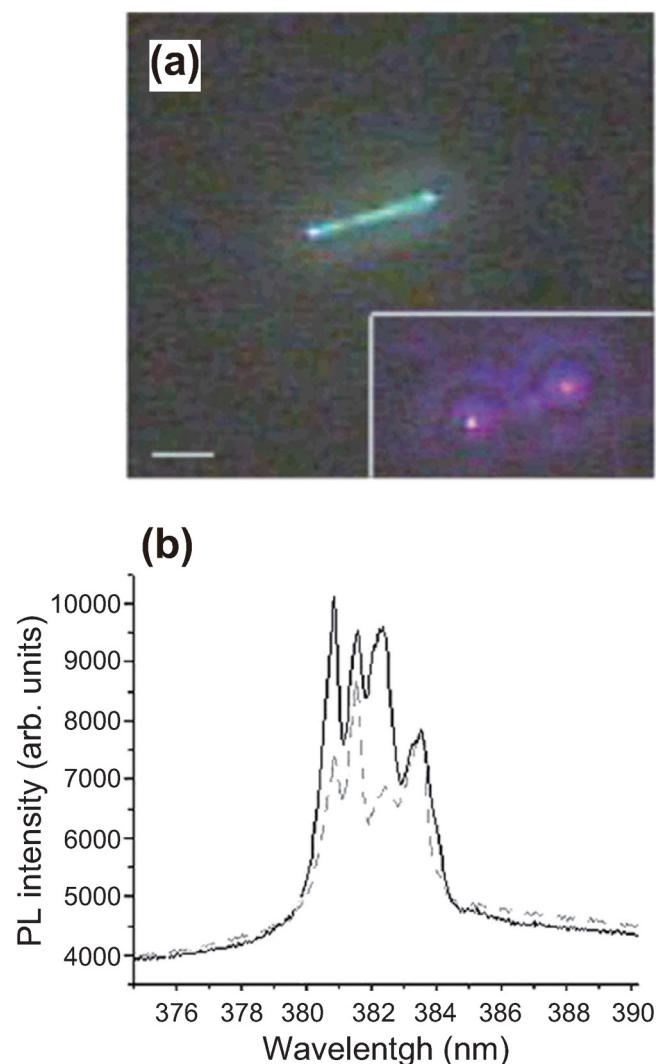


**FIG. 15.** (a) Far-field image and (b) PL spectrum of an individual ZnO nanowire under unpolarized continuous wave excitation at 325 nm. Inset: UV-stimulated emission image of the nanowire with pulsed excitation. Reproduced with permission from C. Johnson *et al.*, *J. Phys. Chem. B* **107**, 8816 (2003). Copyright 2003 American Chemical Society.

with diameters and lengths of  $\sim 50 - \sim 500$  nm and  $\sim 1 - \sim 100$   $\mu\text{m}$ , respectively, where light is amplified along the two end planes of the nanorod perpendicular to the nanorod axis.<sup>13,190,191</sup> The second is whispering gallery mode (WGM) lasing [Fig. 14(b)] observed in ZnO nanorods and nanodisks with cross-sectional

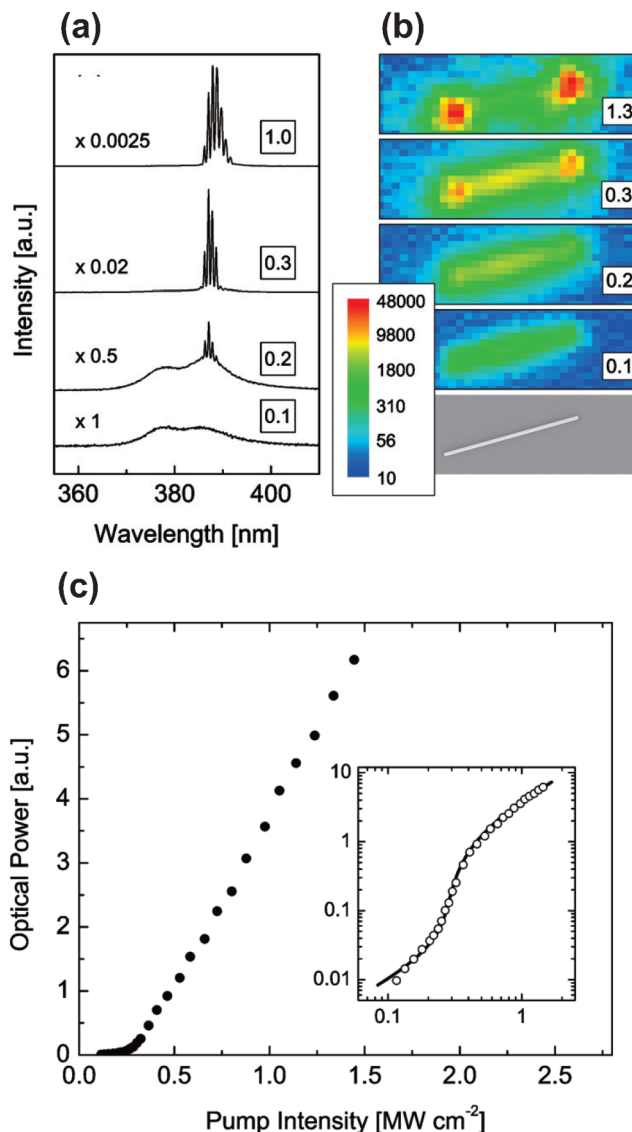


**FIG. 16.** Laser oscillation in ZnO nanowires. (a) Output spectra vs pump intensity of a  $12.2\text{-}\mu\text{m}$  long 250 nm diameter ZnO nanowire. (b) SEM image and CCD images, under different pump intensities, for the same nanowire as in (a). The labels indicate the pump intensity in units of  $\text{MW cm}^{-2}$ . The color scale indicates the number of counts. (c) Pump intensity dependence of the total output power (circles) for the same nanowire. The optical power was collected from the scattered light at one of the nanowire ends. The inset shows the same data on a log-log scale. Reproduced with permission from M. A. Zimmler *et al.*, *Appl. Phys. Lett.* **93**, 051101 (2008). Copyright 2008 AIP Publishing LLC.

07 June 2024 05:50:37

diameters greater than  $\sim 1 \mu\text{m}$ ,<sup>192–197</sup> where light propagates circularly in the cavity due to the multiple total reflection at the inner walls of ZnO cross section.

### 1. Fabry-Pérot (F-P) lasing

In 2001, Huang *et al.* reported a room-temperature optically pumped laser from ZnO single-crystalline nanowire arrays.<sup>10</sup> This

is the first experimental demonstration of nanowire lasers without any fabricated mirror. The advantage of FP microlasers is that by designing the compositional, geometrical, and structural parameters of the nanostructures, it is possible to control the lasing characteristics, for example, Q factor, lasing threshold, number of modes, and lasing wavelengths.

In the nanowire cavity, lasing occurs when the round-trip gain compensates the total cavity losses,<sup>188</sup>

$$\Gamma g_{th} > \alpha_m + a_p = \frac{1}{2L} \ln\left(\frac{1}{R_1 R_2}\right) + a_p, \quad (10)$$

where  $\Gamma$  is the confinement factor,  $g_{th}$  is the threshold gain,  $\alpha_m$  is the mirror loss,  $\alpha_p$  is the propagation loss, and  $R_i$  ( $i = 1, 2$ ) is the effective reflectivity at the ZnO/air boundary of the two end-facets ( $R \approx 15.5\%$ ).  $\Gamma g_{th}$  is commonly referred to as the modal gain, meaning that the percentage power increase per unit length along the propagation direction gained by the waveguide mode from the active region.<sup>191</sup> In nanowire lasers,  $\alpha_m$  is much larger than  $a_p$  due to the smaller cavity length and the smaller reflection coefficient. Hence, it follows that  $\Gamma g_{th}$  as well as Q factor is strongly dependent on both  $L$  and the nanowire diameter  $D$  as  $R$  is a strong function not only of the mode type and lasing frequency but also of  $D$ .<sup>191,198</sup> The exact determination of the modal gain is quite challenging for microcavities. Richters *et al.*<sup>199</sup> determined experimentally the modal gain of single-ZnO nano- and microwires using the variable-stripe-length (VLS) method and found that it reaches a maximum value of  $5000 \text{ cm}^{-1}$  with increasing  $D$  up to  $1.2 \mu\text{m}$ . For the experimental details of the VLS technique, see Refs. 200 and 201.

The Q factor of a nanowire with the cavity length  $L$  is described by<sup>202</sup>

$$Q = \frac{2\pi n' L}{\lambda(1 - \sqrt{R_1 R_2})}, \quad (11)$$

where  $n'$  is the real part of the refractive index and  $\lambda$  is the lasing wavelength. The Q factor obtained from Eq. (11) is an ideal upper limit value provided that the optical absorption and scattering inside the cavity are neglected. For a nanowire with a length of  $10 \mu\text{m}$ , Eq. (11) yields the Q factor of  $\sim 500$  at  $\lambda = 350 \text{ nm}$ . This estimated Q factor is in reasonable agreement with the observed value obtained from the full width at the half maximum  $\delta\lambda$  (FWHM) of the lasing spike peaking at  $\lambda$  ( $Q = \lambda/\delta\lambda$ ) in high-quality ZnO nanowires.<sup>103</sup> Since the report on the ZnO nanowire lasers, optically excited laser action has been demonstrated for a variety of ZnO micro/nanostructures, such as nanoribbons,<sup>203</sup> nanobelts,<sup>204</sup> and tetrapods.<sup>205</sup> In ZnO nanoribbons, pseudo-rectangular cross sections lead to excellent microcavities with a high Q factor of  $\sim 3000$ .<sup>203</sup>

For the confined modes in a rectangular nanowire with dimensions  $L_x$ ,  $L_y$ ,  $L_z$  and perfect conducting surfaces, the dispersion relation between the photon energy  $\hbar\omega$  and the wave vector components,  $k_i$  ( $i = x, y, z$ ), is expressed by<sup>13</sup>

$$\hbar\omega = \frac{\hbar c}{n'(\omega, n_p)} \sqrt{k_x^2 + k_y^2 + k_z^2}, \quad (12)$$

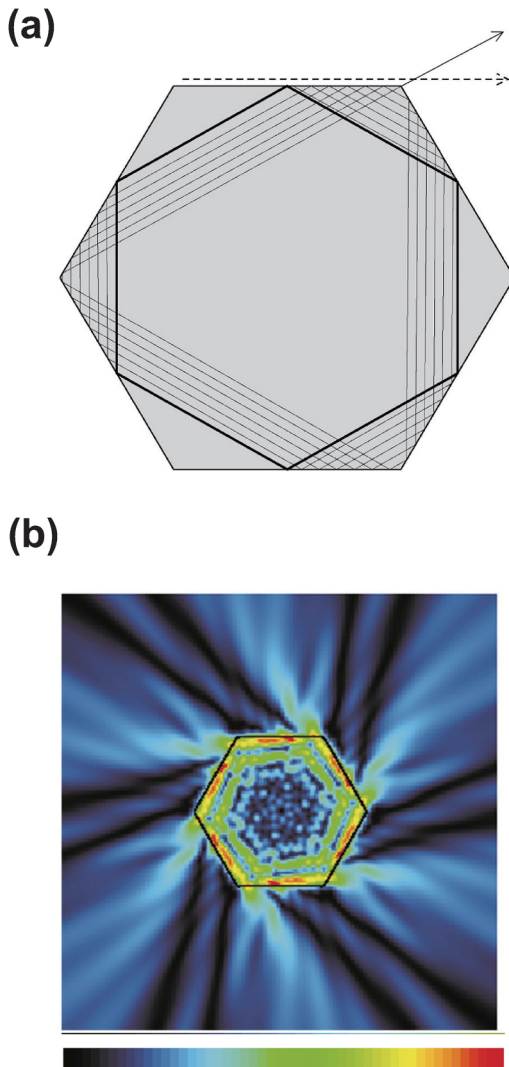


**FIG. 17.** (a) Semiclassical ray model of a hexagonal dielectric resonator. Thick line marks a member of the family of long-lived rays; other members are obtained by shifting the ray along the boundary (not shown). The thin line marks a ray with slightly different angle of incidence. The arrows indicate emission due to pseudointegrable dynamics (thin) and boundary waves (dashed). (b) An example of the calculated near field intensity pattern. Reproduced with permission from J. Wiersig, Phys. Rev. A **67**, 023807 (2003). Copyright 2003 the American Physical Society.

07 June 2024 05:50:37

$$k_{x,y,z} = m_{x,y,z} \frac{\pi}{L_{x,y,z}}, \quad (13)$$

where  $n_p$  is the density of the free electron-hole pairs,  $m_x(m_y)$  and  $m_z$  are the quantum numbers in the lateral and long directions, respectively. We should note that when the dielectric function  $\epsilon_r(\omega)$ , which is equal to the square of  $n'$ , is reduced to the background dielectric constant  $\epsilon_\infty$ , a purely photonic (or linear) dispersion relation is obtained. On the other hand, if the frequency- and density-dependence of  $n'(\omega, n_p)$  is calculated theoretically, one can predict the dispersion curve for a given wire dimension with a

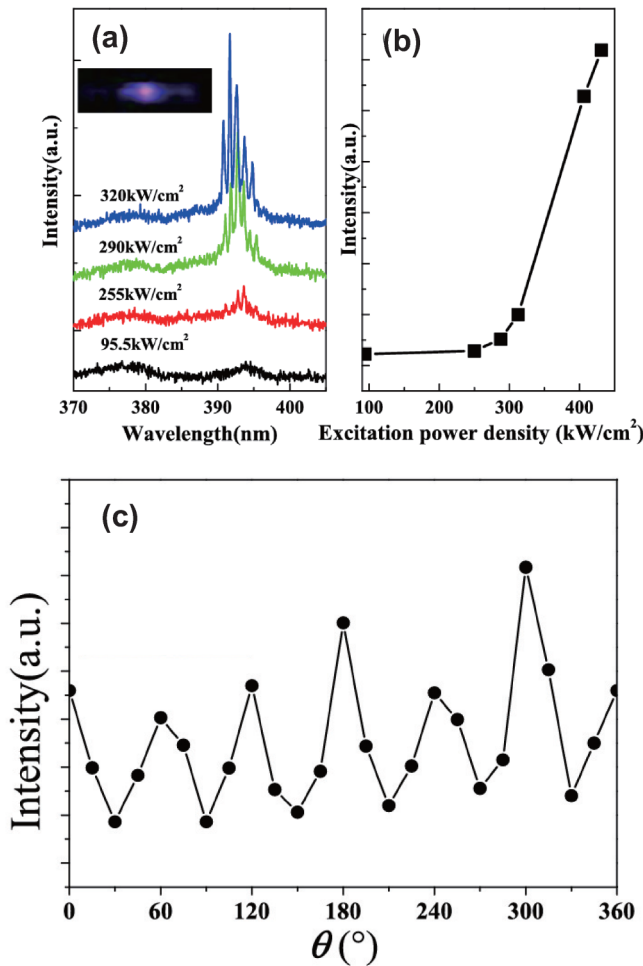


**FIG. 18.** (a) Emission spectra of the ZnO microrod ( $D = 6.67 \mu\text{m}$ ) excited by a Nd:YAG laser with different excitation power density. The inset is the far-field image of the lasing ZnO microrod taken by a digital camera. (b) The relationship between output lasing. (c) The far-field lasing intensity distribution around the  $c$ -axis of the hexagonal ZnO microrod with the diagonal of  $6.67 \mu\text{m}$ . Reproduced with permission from J. Dai *et al.*, *Appl. Phys. Lett.* **95**, 241110 (2009). Copyright 2009 AIP Publishing LLC.

certain carrier density. This calculation was indeed carried out by Versteegh *et al.*<sup>206</sup> based on quantum many-body theory, which has been useful to understand the origin of the optical gain in ZnO nanowires, as will be discussed in Sec. V. For real ZnO nanowires, it can safely be assumed that the allowed quantum number for  $m_x(m_y)$  is 1 or 2, whereas much larger quantum numbers are possible for  $m_z$ . If we plot the dispersion curve as a function of  $k_z$ , the resulting energy levels become discrete for  $L_z$  less than  $\sim 200 \mu\text{m}$ ,<sup>13</sup> whereas they will form a quasi-continuum line for sufficiently long nanowires.<sup>191</sup> The wavelength spacing  $\Delta\lambda$  between individual modes for a F-P cavity with the cavity length  $L$  is given by<sup>202,207,208</sup>

$$\Delta\lambda = \frac{\lambda^2}{2L \left( n' - \lambda \frac{dn'}{d\lambda} \right)}. \quad (14)$$

In analyzing the F-P modes using Eq. (14), it is often assumed that  $\frac{dn'}{d\lambda}$  is constant in the observed wavelength region, showing a linear relationship between a series of  $\Delta\lambda$  and  $1/L$ .<sup>191</sup> However, such a linear behavior does not necessarily hold when the dispersion effect of  $\frac{dn'}{d\lambda}$  cannot be neglected. Zalamai *et al.*<sup>209</sup> observed the cavity mode spectra for ZnO microcavities with a length of  $12 \mu\text{m}$ , and they obtained the first-order dispersion  $\lambda \frac{dn'}{d\lambda}$  from the position of lasing modes using the data of  $n'$  at different wavelengths.

As for Zn-based nanowire lasers, it is possible to observe lasing characteristics of a single ZnO nanowire (Fig. 15).<sup>207,208,210</sup> Figure 16 shows the pump-intensity-dependent PL spectra of these ZnO nanowires under excitation with the third harmonic (355 nm) of a nanosecond pulsed Nd:YAG laser.<sup>208</sup> For pump intensity  $I_{\text{ex}} \leq 200 \text{ kW cm}^{-2}$ , the spectra are broad and featureless, centered around 382 nm and with an FWHM of 19.3 nm [Fig. 16(a)]. In this regime, light is emitted essentially isotropically along the nanowire

07 June 2024 05:50:37

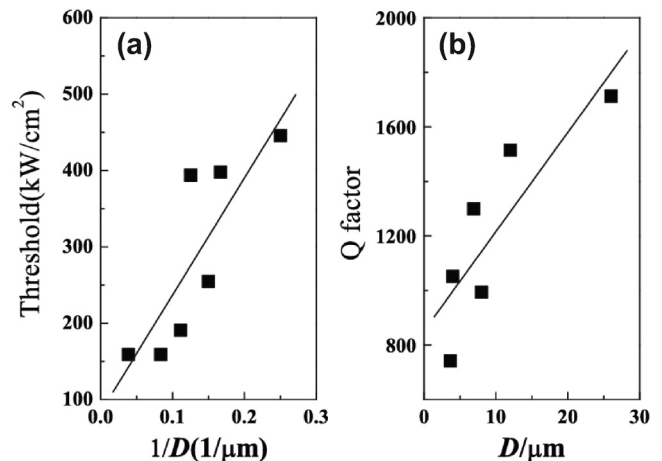


**FIG. 19.** The dependence of (a) the lasing threshold and (b) the Q factor on the diagonal of the hexagonal ZnO microrods. Reproduced with permission from J. Dai *et al.*, *Appl. Phys. Lett.* **95**, 241110 (2009). Copyright 2009 AIP Publishing LLC.

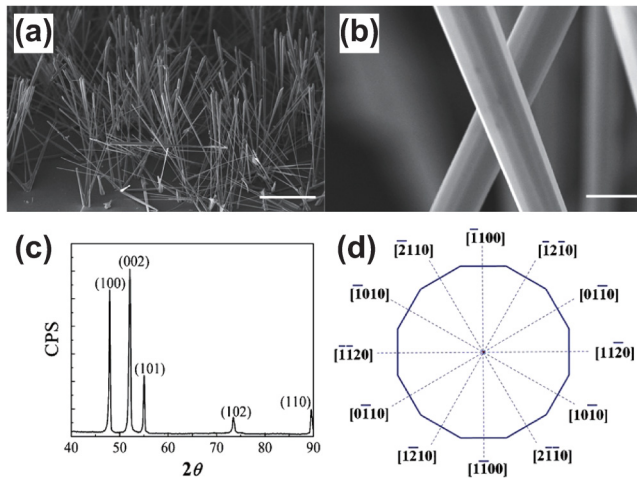


**FIG. 20.** (a) SEM image of the size view of ZnO dodecagonal microrods (the substrate is  $60^\circ$  tilted to the sample platform), the scale bar is  $200\ \mu\text{m}$ . (b) The enlarged SEM image of the microrods with higher magnification, the scale bar is  $5\ \mu\text{m}$ . (c) XRD pattern for the bulk of ZnO dodecagonal microrods. (d) 12 crystal facets for dodecagonal microrods. Reproduced with permission from J. Dai *et al.*, *Appl. Phys. Lett.* **97**, 011101 (2010). Copyright 2010 AIP Publishing LLC.

[Fig. 16(b)], and the output power depends linearly on the excitation intensity [Fig. 16(c)], showing the occurrence of spontaneous emission. In the pump intensity region from 200 to  $300\ \text{kW cm}^{-2}$ , the spectra consist of a broad emission with the addition of sharp (FWHM  $\sim 0.4\ \text{nm}$ ) emission lines. In this regime, population inversion starts building up, leading to ASE along the nanowire at wavelengths corresponding to the enhanced emission from the nanowire ends [Fig. 16(b)]. Furthermore, the output power exhibits a superlinear increase with pump intensity [Fig. 16(c)], which is the expected behavior as the laser threshold is approached.<sup>211</sup> For  $I_{\text{ex}} > 300\ \text{kW cm}^{-2}$ , the spectra are dominated by sharp emission lines with intensity that is orders of magnitude greater than the spontaneous emission background. Thus, in general, the threshold in semiconductor lasers is “softer” than that in other lasers due to the small cavity volume and to the relatively high levels of spontaneous emission.<sup>211</sup>

Recently, it has been shown that through the coupling between metal surface plasmon modes and FP modes of ZnO, surface plasmonic lasers are realized.<sup>212,213</sup> In comparison to the conventional photonic laser, the plasmonic cavities exhibit ultra-small modal volume  $V_m \sim \lambda^3/10 - \lambda^3/1000$ , which enables the control of the strong light-matter interaction in a variety of linear and nonlinear optical process, and the generation of extremely intense optical fields. Sidiropoulos *et al.*<sup>212</sup> observed the emission pulses shorter than  $800\ \text{fs}$  from hybrid plasmonic zinc oxide (ZnO) nanowire ( $5 < L < 20\ \mu\text{m}$ ,  $100 < D < 300\ \text{nm}$ ) lasers. In such plasmonic lasers, the atomic smoothness of the metallic film is crucial for reducing the modal volume and plasmonic losses.<sup>214</sup> Graphene/ZnO hybrid microcavity has also been shown to be useful to realize plasmon coupled F-P lasing, resulting in the lowered lasing

threshold and the remarkably enhanced lasing intensity.<sup>215</sup> Chou *et al.*<sup>216</sup> recently investigated ZnO plasmonic nanolasers on a pseudowedge surface plasmon waveguide formed on a high-quality Ag crystal carved with a subwavelength metallic grating, which allows them to shorten the effective cavity length and to realize single longitudinal-mode lasing.

Compared with optically pumped lasing, reports on the electrically pumped nanolasers are rather few. This is mainly due to the fact that stable and reproducible production of p-type ZnO nanostructures is still challenging for ZnO micro/nanostructures with a p-n homojunction. Note, however, that Chu *et al.*<sup>217</sup> successfully demonstrated electrically driven FP lasing from n-type ZnO

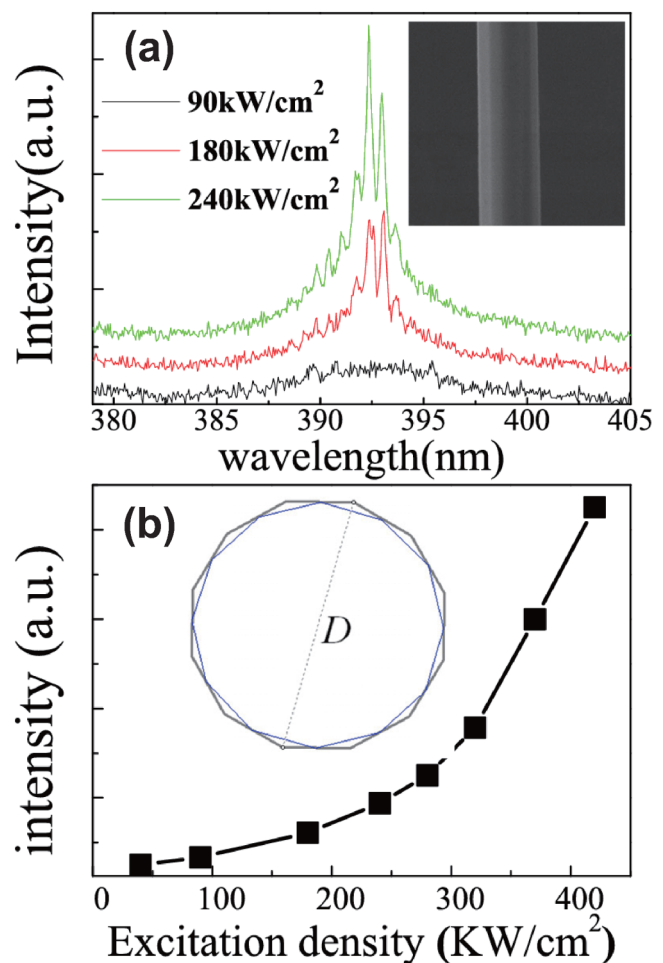


**FIG. 21.** (a) Exciton lasing emission spectra of the ZnO microwire ( $D = 6.35\ \mu\text{m}$ ) excited by a Nd:YAG laser with different excitation power density. The inset shows the SEM image of the selected dodecagonal microrod. (b) The relationship between output lasing intensity and excitation power density. The inset shows the WGM optical path in the dodecagonal cavity. Reproduced with permission from J. Dai *et al.*, *Appl. Phys. Lett.* **97**, 011101 (2010). Copyright 2010 AIP Publishing LLC.

07 June 2024 05:50:37



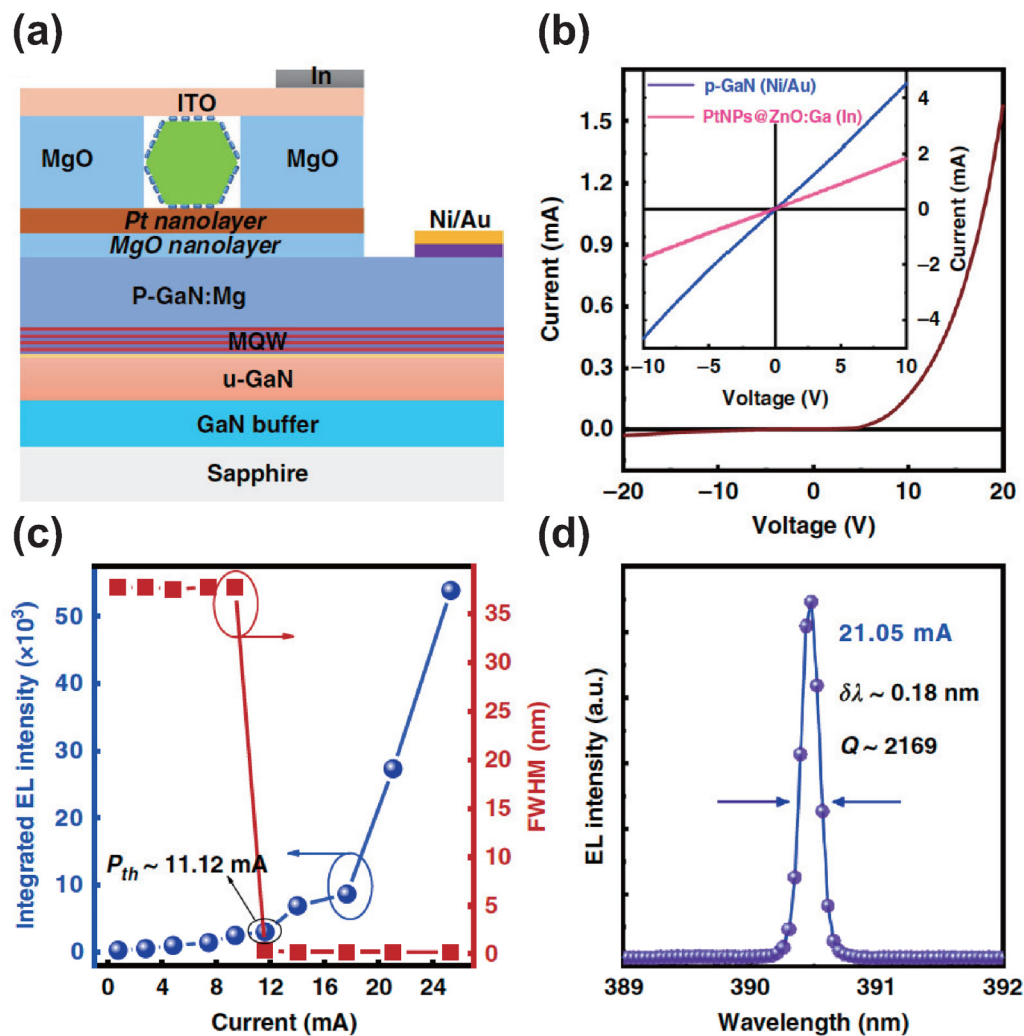


**FIG. 22.** (a) Schematic illustrating the cross section of the laser device architecture based on the n-PtNPs@ZnO:Ga MW/Pt/MgO/p-GaN heterojunction. In the device configuration, ITO and Ni/Au working as electrodes are responsible for the current injection. (b) I–V curve of the fabricated single MW heterojunction emission device. Inset: the I–V curves of Ni/Au electrode contacted to the p-type GaN film, and a single PtNPs@ZnO:Ga MW, respectively. (c) Variations of the integrated EL intensity and spectral FWHM as a function of injection current, showing a lasing threshold of 11.12 mA. (d) EL spectrum via Lorentz fitting at the input current of 21.05 mA, providing the FWHM of the lasing peak  $\delta\lambda \sim 0.18$  nm, and the corresponding Q-factor value is calculated to about 2169. Reproduced with permission from X. Zhou *et al.*, *Light: Sci. Appl.* **11**, 198 (2022). Copyright 2022 Author(s), licensed under a Creative Commons Attribution (CC BY) License.

nanowires combined with p-type Sb-doped ZnO nanowires. An attempt to design and fabricate electrically pumped ZnO nanolasers with p-n heterojunctions<sup>218</sup> as well as those on other II–VI or III–V semiconductors<sup>219–221</sup> have also been reported.

## 2. Whispering gallery mode (WGM) lasing

The FP lasing mentioned in Subsection IV B 1 is historically important in view of nanowire photonics. However, a high level of confinement cannot be in principle obtained in FP lasing due to the low reflectivity ( $R \approx 15.5\%$ ) at the ZnO/air interfaces for the FP

cavity. This drawback can be improved by using another kind of resonator mode: WGM. In WGM lasing, the resonance is generated through total internal reflection (TIR) at the cavity boundary. This results in WGM being ideally free from mirror losses as perfect TIR provides a 100% reflection. Even when perfect TIR occurs in hexagonal microcavities, the light can escape at the corners of the cavity.<sup>222</sup> Figure 17(a) shows a ray with slightly different initial angle of incidence caused by the incident angular fluctuation. The ray is slowly diverging from the central one, eventually reaching the corner on its other side at almost normal incidence. Consequently, it then escapes refractively with probability close to 1, as also

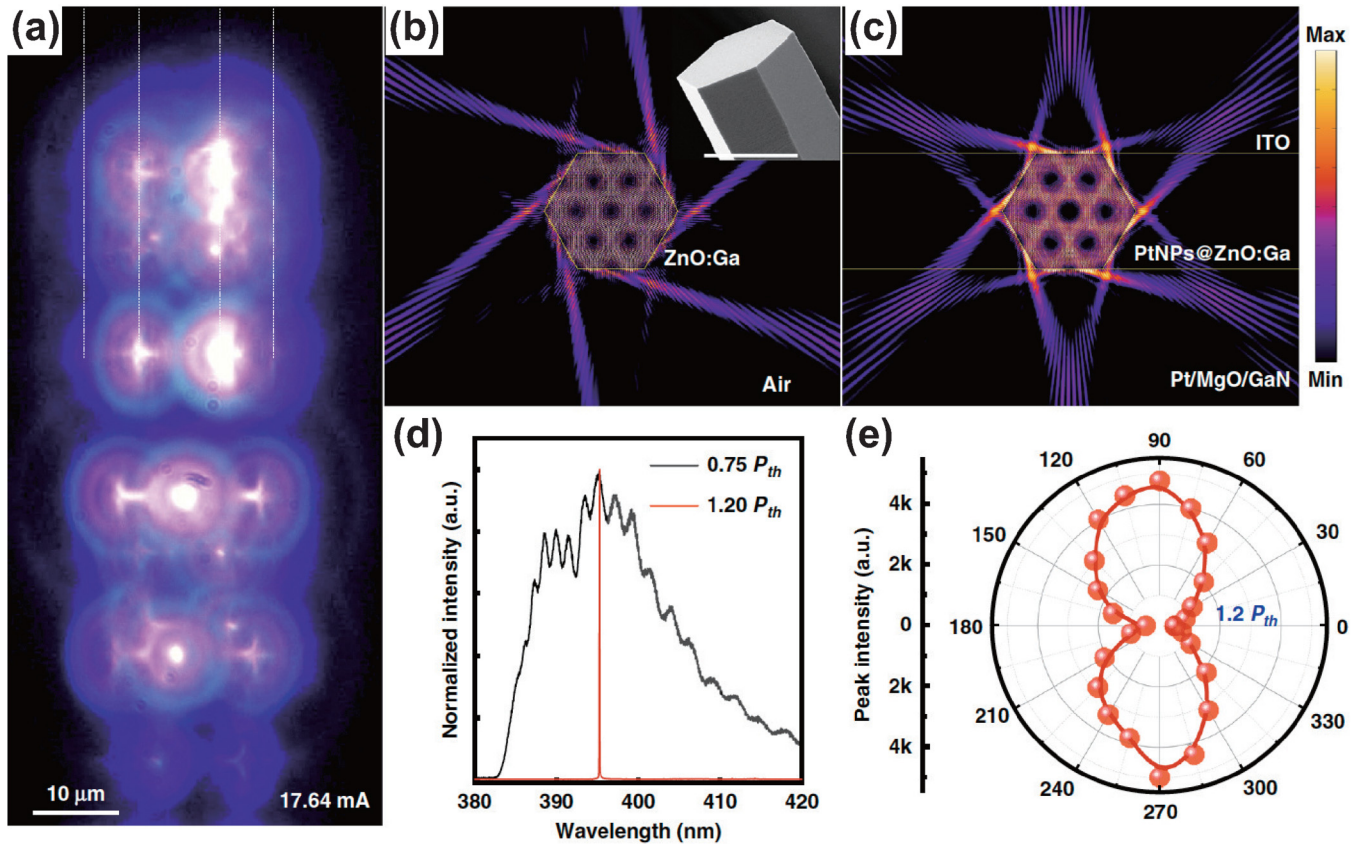


**FIG. 23.** (a) Optical microscopic CCD image of the emission from the fabricated device. (b) Finite-element simulations showing the standing-wave electric-field pattern of a bare ZnO:Ga wire with hexagon-shaped cross section under an optical resonant mode. Inset: SEM observation of a bare ZnO:Ga wire that showing the hexagon-shaped cross section (scale bar:  $15\ \mu\text{m}$ ). (c) The simulated resonant standing-wave electric-field pattern within the cross section of the fabricated n-PtNPs@ZnO:Ga MW/Pt/MgO/p-GaN emission device structure. (d) Normalized EL emission spectra of the fabricated device for two injection currents below ( $0.75 P_{th}$ ) and above ( $1.20 P_{th}$ ) the laser threshold, respectively. (e) Polarization properties of the laser emission for an operating current above the threshold ( $\sim 1.20 P_{th}$ ). The experiment EL data are symbolized by the red dots and the red solid line is the fitting result. Reproduced with permission from X. Zhou *et al.*, *Light: Sci. Appl.* **11**, 198 (2022). Copyright 2022 Author(s), licensed under a Creative Commons Attribution (CC BY) License.

shown in the simulated light-field distribution [Fig. 17(b)]. This phenomenon is referred to as the pseudointegrable leakage. In addition, corner diffraction<sup>223</sup> and boundary-wave leakage associated with the presence of evanescent waves<sup>222</sup> are also responsible for partial leakage of light from the hexagonal cavity. Consequently, the lasing intensity would be distributed with a period angle of  $\pi/3$ , which was confirmed experimentally by Dai *et al.*<sup>224</sup> using a ZnO hexagonal microrod with  $D$  of  $6.67\ \mu\text{m}$  (Fig. 18). The escape rate of the light due to the pseudointegrable leakage in a hexagonal cavity is expected to be nearly inversely proportional to the cavity size  $D$ .<sup>224</sup> Therefore, the lasing threshold of the hexagonal ZnO cavity was found to show an approximately linear dependence on  $1/D$  [Fig. 19(a)].<sup>185,224</sup> A typical lasing threshold for the hexagonal ZnO cavity with  $D > 10\ \mu\text{m}$  is  $100\text{--}200\ \text{kW}/\text{cm}^2$ .<sup>185,224,225</sup> It is also interesting to mention the  $Q$  factor of ZnO WGM microcavities since it is a useful measure of determining the feedback in the resonant cavity. Similar to the case of

lasing threshold, the  $Q$  factor shows a strong dependence on  $D$  [Fig. 19(b)]. For a sufficiently large ( $D \sim 12.6\ \mu\text{m}$ ) high-quality hexagonal ZnO microdisk, a  $Q$  factor as high as 3300 has been reported.<sup>225</sup> This value is much larger than that observed commonly in ZnO F-P cavities ( $Q \sim 500$ ),<sup>103</sup> demonstrating that the feedback performance of WGM microcavities is better than that of the F-P ones. Such a high value of  $Q$  even allows one to realize one-dimensional multimode polariton systems, as will be shown in Sec. VI.

In addition to the hexagonal WGM microcavities, lasing from dodecagonal WGM cavities has also been reported (Fig. 20).<sup>226</sup> During the growth of ZnO microrods by a vapor phase transport method, the deposition area was kept at a very high temperature ( $\sim 1000\ ^\circ\text{C}$ ) so that the evaporated Zn and O atoms have enough energy to bind and diffuse on (01 $\bar{1}$ 0) and ( $\bar{2}$ 110) surface evenly, resulting in the dodecagonal microrods with  $D < \sim 10\ \mu\text{m}$  [Fig. 20(b)]. Compared to the case of hexagonal cavities with

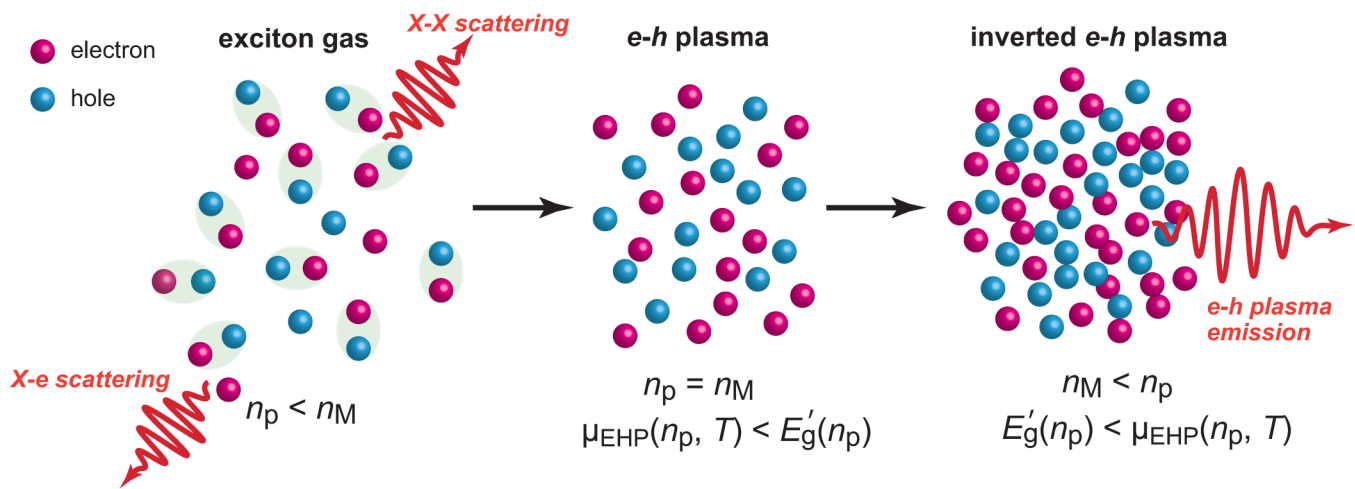


**FIG. 24.** Schematic illustrations of exciton gas and electron–hole ( $e$ – $h$ ) plasma states in photoexcited semiconductors for increasing density of electron–hole pairs  $n_p$ . Principal stimulated emission processes including exciton–exciton (X–X) scattering, exciton–electron (X–e) scattering, and  $e$ – $h$  plasma emission processes are shown.  $n_M$ ,  $E_g'$ , and  $\mu_{\text{EHP}}$  are the Mott density, the reduced bandgap, and the chemical potential of the  $e$ – $h$  system, respectively (see also Fig. 27).

similar sizes, a lower lasing threshold ( $180 \text{ kW/cm}^2$ ) and a higher  $Q$  factor ( $Q \sim 2600$ ) are obtained from the dodecagonal ZnO microrod ( $D = 6.35 \mu\text{m}$ ), as shown in Fig. 21. This is because the WGM optical length in a dodecagonal cavity is longer than that in a hexagonal one with the same cross-sectional diameter.

There have been a few reports on electrically driven ZnO WGM lasers.<sup>227–229</sup> Recently, Zhou *et al.*<sup>229</sup> reported electrically driven lasing from a system consisting of Ga doped ZnO hexagonal microwire (ZnO:Ga) with  $D = 15 \mu\text{m}$  covered partially with platinum nanoparticles and a p-type GaN substrate (Fig. 22). This ZnO:Ga/GaN heterojunction exhibits electrically driven single-mode lasing with a linewidth of  $\sim 0.18 \text{ nm}$ , corresponding to the  $Q$  factor of  $\sim 2169$  [Fig. 22(d)]. The WGM lasing characteristics was confirmed from the optical microscopic CCD image as well as the angle-dependent variation of the laser emission intensity (Fig. 23).

## V. GAIN MECHANISM FOR LASING

Two principal gain mechanisms have been believed to be responsible for lasing in ZnO bulk and nanostructures: excitonic and electron–hole plasma (EHP) recombination processes. When the density of electron–hole pairs  $n_p$  reaches the Mott density  $n_M$ , the transition from an insulating exciton gas to a metal-like state of an EHP occurs,<sup>230</sup> as shown schematically in Fig. 24. This indicates that  $E_X^b$  becomes zero as  $n_p$  reaches  $n_M$ ,<sup>231</sup>

$$E_X^b(n_M, T) = 0. \quad (15)$$

The Mott density can be calculated within various approximations. At zeroth approximation,  $n_M$  can be regarded as the carrier density at which average exciton–exciton distance becomes

approximately equal to  $a_{\text{Bohr}}^{\text{ZnO}}$ , which is given by

$$n_M \approx \frac{1}{(a_{\text{Bohr}}^{\text{ZnO}})^3}. \quad (16)$$

However, this model tends to overestimate the critical density [ $n_M = 1.7 \times 10^{20} \text{ cm}^{-3}$  for  $a_{\text{Bohr}}^{\text{ZnO}} \sim 1.8 \text{ nm}$ ,<sup>19</sup> see also Eq. (5)]. Several more refined and experimentally checked models taking into account the electrostatic screening and the many-body effect have been proposed.<sup>231–235</sup> However, the estimated value of  $n_M$  in ZnO at room temperature shows a variation in the range from  $3 \times 10^{17}$  to  $6 \times 10^{18} \text{ cm}^{-3}$ .<sup>231–234</sup> Its exact determination is of great importance but is still an open question, as will be discussed later.

## A. Excitonic lasing

Historically, exciton-related spontaneous and stimulated emission processes in ZnO as well as in other II–IV and III–V direct gap compounds were extensively investigated both experimentally and theoretically in 1970/1980s using high-quality bulk single crystals.<sup>236–242</sup> From these investigations, it has been revealed that in ZnO, stimulated emissions with excitonic gain occur when the second particle (exciton, electron, phonon) is involved in the recombination process. Among other processes, the following three emission processes are especially of interest:

- (i) Exciton–exciton (X–X) recombination,
- (ii) Exciton–electron (X–e) recombination,
- (iii) Exciton– $m$ LO phonon (X– $m$ LO,  $m = 1, 2, \dots$ ) recombination.

Schematic drawings of the above recombination processes are given in Fig. 25. We will explain the reason why, unlike the case of the simple recombination of a free exciton, the above excitonic processes show stimulated emission, or population inversion, by

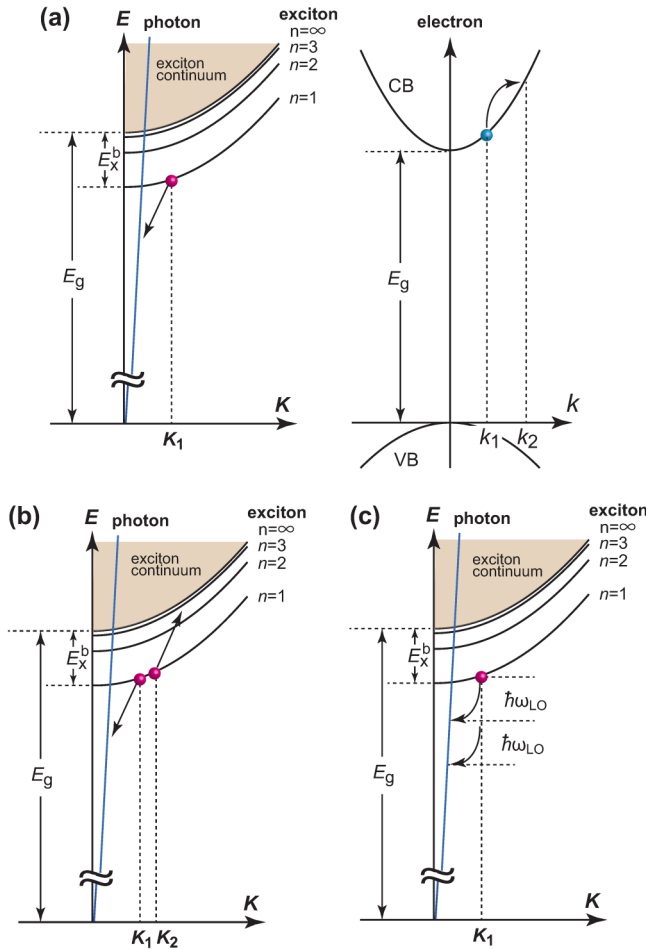


FIG. 25. Schematic representations of (a) exciton–electron, (b) exciton–exciton, and (c) exciton–mLO phonon recombination processes.

considering the optical emission and absorption processes, for example, of the X-X scattering.<sup>238</sup>

If the momentum of the photon is neglected, the recombination energy  $\hbar\omega$  due to the inelastic interaction between two excitons can be described as<sup>238,239</sup>

$$\hbar\omega = (E_g - E_X^b) - E_X^b \left(1 - \frac{1}{n^2}\right) - \frac{\hbar^2}{M} \mathbf{K}_1 \cdot \mathbf{K}_2, \quad (17)$$

$n = 2, 3, \dots$

where  $M$  is the exciton mass,  $\mathbf{K}_1$  and  $\mathbf{K}_2$  are wave vectors of the initial two excitons, and  $n$  is the quantum number of the scattered exciton [see Fig. 25(b)]. When considering the maximum value of  $\hbar\omega$ , we can replace the last term in Eq. (17) by the mean kinetic

energy.<sup>239</sup> Hence, we get

$$\hbar\omega_{\max}^{X-X} = (E_g - E_X^b) - E_X^b \left(1 - \frac{1}{n^2}\right) - \frac{3}{2} k_B T, \quad n = 2, 3, \dots \quad (18)$$

where  $k_B$  is the Boltzmann constant. The resulting emission band is conventionally referred to as the  $P(n)$  band.<sup>238,239</sup> As photons and excitons are bosons, the rate of their generation is not only proportional to their numbers but is also increased by unity.<sup>243</sup> The total rate of photon emission  $w_e$  in the X-X scattering process is given by

$$r_e = AN_{1,K_1}N_{1,K_2}(1 + N_{n,K_1+K_2})(1 + N_w), \quad (19)$$

where  $N_w$  is the density of photons,  $N_{1,K_1}(N_{1,K_2})$  is the density of the initial state of excitons with a wave vector  $\mathbf{K}_1(\mathbf{K}_2)$ ,  $N_{n,K_1+K_2}$  is the density of the final  $n$  state for the scattered exciton, and  $A = A(n, K_1, K_2, \omega)$  is the rate constant containing the optical matrix element and the scattering matrix element. The rate of photo absorption due to an inverse process is given by

$$r_a = A(N_{1,K_1} + 1)(N_{1,K_2} + 1)N_{n,K_1+K_2}N_w. \quad (20)$$

If we neglect the losses caused by the escape of photons from the system, the net emission rate is given by subtracting Eq. (20) from Eq. (19),

$$r_{e, \text{net}} = AN_{1,K_1}N_{1,K_2}(N_{n,K_1+K_2} + 1) + A(N_{1,K_1}N_{1,K_2} - N_{n,K_1+K_2}(N_{1,K_1} + N_{1,K_2} + 1))N_w. \quad (21)$$

The first and second terms in Eq. (21) represent the rates of spontaneous emission  $w_{e, \text{spont}}$  and stimulated emission  $w_{e, \text{stim}}$ , respectively. It is clear that  $r_{e, \text{stim}}$  is increased as the population of the final  $n$  state for the scattered excitons  $N_{n,K_1+K_2}$  is decreased. It is probable that the  $n = \infty$  state is empty even in high excitation conditions, meaning that the condition of a population inversion (optical gain) is realized preferentially for  $n = \infty$ . Hence, in high-quality ZnO crystals with low optical losses, moderate/high optical excitation leads to stimulated emission in the energy region of the  $P(\infty)$  line, which is preceded by the transition from a spontaneous  $P(2)$  to a  $P(\infty)$  process.<sup>237–239,244</sup> From Eq. (18), one sees that the stimulated  $P(\infty)$  line shows a redshift with respect to the recombination energy of the free exciton by the exciton binding energy ( $E_X^b = 60$  meV) at low temperatures ( $k_B T \sim 0$ ). The gain mechanism of the X-e and X-mLO processes can also be explained in a similar manner. For example, the population inversion occurs in the X-mLO process provided that there is one exciton and no LO phonon. The temperature dependence of the emission maximum for the X-e and X-mLO ( $m = 1, 2$ ) processes is described by<sup>239</sup>

$$\hbar\omega_{\max}^{X-e} = (E_g - E_X^b) - \gamma k_B T, \quad (22)$$

$$\hbar\omega_{\max}^{X-m\text{LO}} = (E_g - E_X^b) - m\hbar\omega_{\text{LO}} + \left(\frac{5}{2} - m\right)k_B T, \quad (23)$$

where  $\gamma$  is a constant related to the ratio of exciton effective mass

07 June 2024 05:50:37

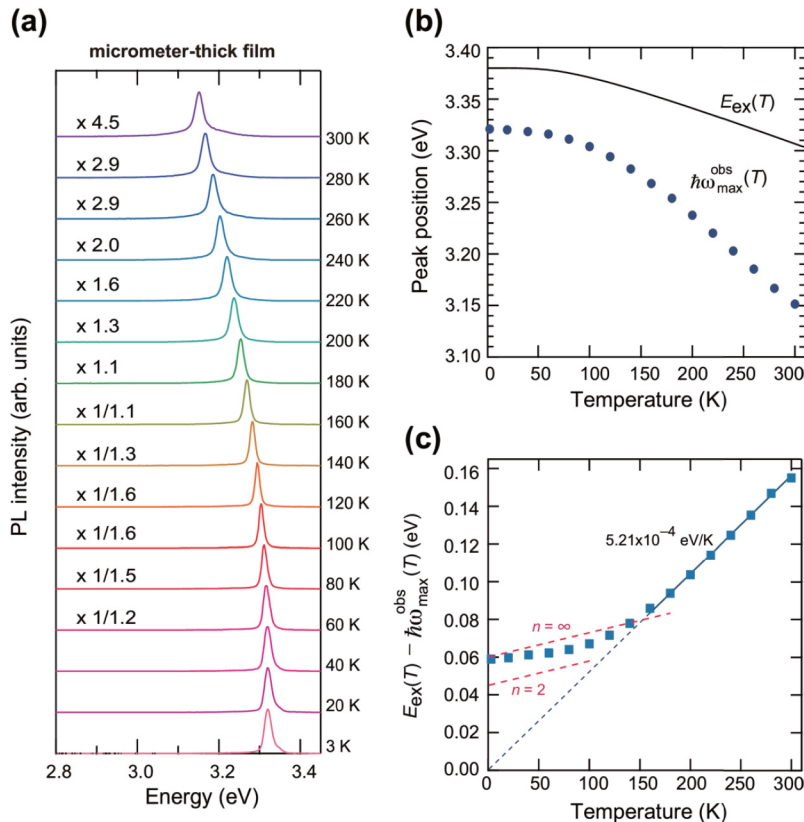


**FIG. 26.** Temperature dependence of the lasing spectra observed for the micrometer-sized ZnO film. (a) Changes in the lasing spectra with increasing temperature from 3 to 300 K measured under a constant excitation fluence of  $10.4 \text{ mJ/cm}^2$ . The peak intensities are normalized among all spectra, which are displaced vertically for clarity. (b) The peak energy  $\hbar\omega_{\text{max}}^{\text{obs}}$  as a function of temperature. The free-exciton transition energy  $E_{\text{ex}} = E_g - E_X^b$  is also shown as a solid line. (c) The energy difference between  $E_{\text{ex}}$  and  $\hbar\omega_{\text{max}}^{\text{obs}}$  as a function of temperature. The solid line shows a least-squares fit of the data in the temperature region from 160 to 300 K to Eq. (22), which represents the temperature dependence of the emission maximum for the X-el process. The energy differences between  $E_{\text{ex}}$  and  $\hbar\omega_{\text{max}}^{\text{obs}}$  for  $n=2$  and  $\infty$  calculated from Eq. (18) are also shown as red dashed lines. One sees that the emission process changes from the X-X process to the X-e process with increasing temperature. Reproduced with permission from R. Matsuzaki *et al.*, Phys. Rev. B **96**, 125306 (2017). Copyright 2017 the American Physical Society.

over electron effective mass and  $\hbar\omega_{\text{LO}}$  is the quantum energy of the LO phonon ( $\hbar\omega_{\text{LO}} = 72 \text{ meV}$ ).<sup>19</sup> It has been demonstrated that  $\gamma$  reaches values as high as 7 in the case of the X-e stimulated emission.<sup>239</sup> The X-*m*LO process is observed preferentially when a large volume with low losses is excited, for example, by two-photon absorption because of its relatively low gain.<sup>239</sup>

Although the stimulated emission due to the X-X process was well documented in bulk ZnO single crystals<sup>237–239</sup> and epitaxial layers<sup>244</sup> at temperatures below  $\sim 70 \text{ K}$ , the claim of its occurrence at room temperature from ZnO thin films<sup>5–8</sup> has been debated.<sup>2,231</sup> This is because the  $n \geq 2$  excitonic states become thermally populated with increasing temperature, leading to thermal ionization of excitons as well as an increase of the threshold of the X-X stimulated emission process. It is, hence, expected that the transition from the X-X to X-e occurs at temperatures above 100 K.<sup>2,231</sup> This expectation was indeed confirmed by Uchino and coworkers<sup>245,246</sup> by measuring the temperature-dependent random laser emission with incoherent feedback in micrometer-thick ZnO and  $\text{Mg}_x\text{Zn}_{1-x}$  films (Fig. 26), whose lasing spectra represent the ASE or the maximum of the net gain of the medium (see Sec. IV A 2).

It should be noted that room-temperature excitonic lasing is not normally observed in nanometer-sized ZnO crystals, such as nanopowders (random laser) and nanowires (F-P cavity), because in these nanocrystals, the optical excitation near the lasing threshold easily reaches the regime of  $n_M$  to yield an EHP emission, as

will be shown in Subsection V B. That is, in order to realize excitonic lasing, the sample size must be comparable to or larger than the diffusion length of the excited carriers ( $\sim 3 \mu\text{m}$ <sup>230</sup>) to suppress the formation of the high-density photoexcited carrier region that exceeds  $n_M$ .<sup>245</sup> The effect of size on the gain mechanism is also recognized in WGM lasing. Hexagonal or dodecagonal ZnO micro-rods with a diameter of  $D \geq \sim 8 \mu\text{m}$  show a feature of excitonic WGM lasing, whose peak positions depend hardly on the excitation density.<sup>224–226</sup> On the other hand, the lasing spectra from those with  $D \leq \sim 3 \mu\text{m}$  exhibit a substantial redshift and broadening with increasing excitation intensity, which is a typical characteristic of an EHP emission<sup>226</sup> (for details, see Subsection V B).

## B. Electron-hole plasma (EHP) lasing

Nonlinear optics and the Mott transitions leading to the formation of an EHP in highly excited semiconductors have attracted considerable interest for many years. Several theoretical approaches have been given to describe the Mott transition and the spectral features of correlated excitons and EHP.<sup>242,247,248</sup> The generation of correlated states results from many-body effects, which should be treated using the many-body Hamiltonian taking into account the full Coulomb interaction.<sup>248</sup> In this Tutorial, however, we concentrate our interest on the estimation of  $n_M$  and the condition of the optical gain for an inverted EHP.

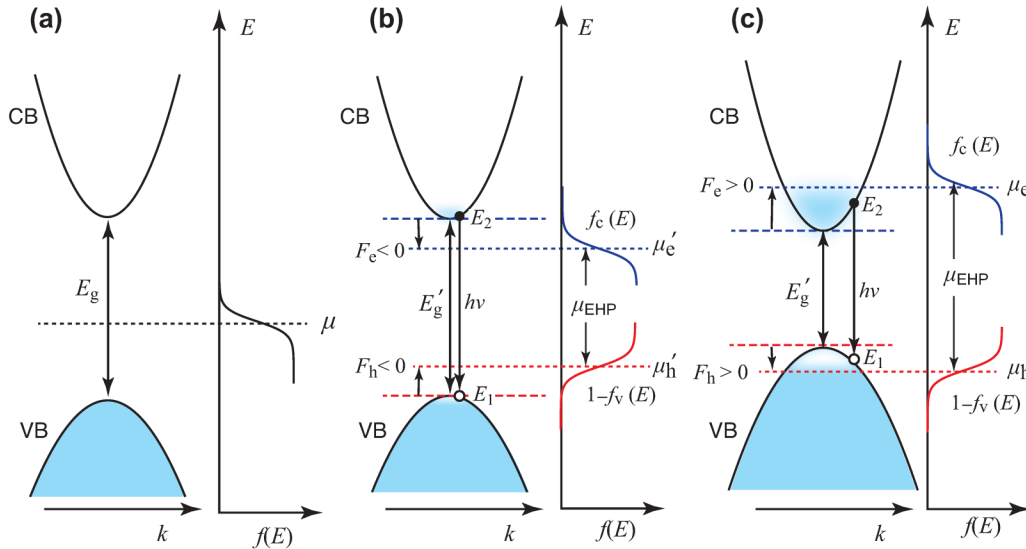


**FIG. 27.** Schematic representation of the conduction band (CB) and valence band (VB) near the high-symmetry  $\Gamma$  point with bandgap energy  $E_g$  and the corresponding Fermi-Dirac distribution function  $f(E)$ . The blue shaded areas indicate the states occupied largely by electrons. (a) Before photoexcitation, (b) under weak photoexcitation condition, and (c) under high photoexcitation condition, in which the condition of optical gain given in Eq. (37) is realized.  $E'_g$  represents the reduced bandgap, and  $\mu'_e$  and  $\mu'_h$  are the quasi-Fermi levels for electrons in CB and for holes in VB, respectively.  $F_e$  and  $F_h$  also represent the quasi-Fermi levels measured from the corresponding band extremes.  $h\nu$  is the photon energy of the electron-hole recombination process indicated.

First, we consider what happens when the density of free excitons increases during photoexcitation. For an isolated free exciton, the attractive force from the Coulomb potential is given by

$$U(r) = -\frac{e^2}{4\pi\epsilon_r\epsilon_0 r}, \quad (24)$$

where  $r$  is the distance between electron and hole. As the temperature of the system increases, some of the excitons are assumed to be ionized, resulting in a certain number of free electron-hole pairs  $n_p$ . Accordingly, the interaction potential should be replaced by the following Yukawa potential to include the effect of effective screening of the Coulomb interaction,<sup>243</sup>

$$U_s(r) = -\frac{e^2}{4\pi\epsilon_r\epsilon_0 r} \exp\left(-\frac{r}{\lambda_s}\right), \quad (25)$$

where  $\lambda_s$  is the screening length. Versteegh *et al.*<sup>232</sup> used the value of 6.56 for  $\epsilon_r$  (see Sec. III A) and demonstrated that the Yukawa potential can be used as long as  $n_p < 2.8 \times 10^{20} \text{ cm}^{-3}$  where the approximation of static screening almost holds. For an isolated free exciton,  $\lambda_s$  is infinite, whereas  $\lambda_s$  becomes shorter with increasing  $n_p$ . When  $\lambda_s$  reaches  $a_{\text{Bohr}}^{\text{ZNO}}$ , the attractive interaction between a single electron and a hole is screened, i.e.,  $E_X^b = 0$ , eventually leading to the transition of the exciton gas to an EHP. If we have knowledge of  $\lambda_s$  as a function of  $n_p$  and  $T$ , we can estimate  $n_M$  at any temperature. However, it is rather a difficult task to get exact knowledge of  $\lambda_s(n_p, T)$ , accounting for a wide range of reported values of  $n_M$ , as noted earlier. Versteegh *et al.*<sup>232</sup> numerically

calculated  $\lambda_s(n_p, T)$  using the following formula:

$$\lambda_{s,i} = \sqrt{\frac{\epsilon_r\epsilon_0}{e^2} \frac{\partial F_i}{\partial n_p}}, \quad (26)$$

$$\lambda_s^{-2} = \sum_i \lambda_{s,i}^{-2}, \quad (27)$$

$$n_p = n_i = \frac{1}{2\pi^2} \left(\frac{2m_i}{\hbar^2}\right)^{3/2} \int_0^\infty d\epsilon \sqrt{\epsilon} \frac{1}{\exp[(\epsilon - F_i)/k_B T] + 1}, \quad (28)$$

where  $i$  stands for  $e$  (electron) or  $h$  (hole) and  $F_i$  is the quasi-Fermi levels (chemical potentials) measured from the corresponding band extremes (see Fig. 27). Thus, in this case, one has to define two separate quasi-Fermi levels for electrons in the conduction band ( $\mu'_e$  or  $F_e$ ) and for holes ( $\mu'_h$  or  $F_h$ ) in the valence band. The resulting relationship between  $\lambda_s$  and  $n_p$  at 300 K is given in Fig. 28, demonstrated that  $n_M = 1.5 \times 10^{18} \text{ cm}^{-3}$ . This procedure reported by Versteegh *et al.*<sup>232</sup> probably yields the most reliable and reasonable value for  $n_M$ , in consistent with the experimentally estimated upper limit of  $n_M$  ( $n_M < 2-3 \times 10^{18} \text{ cm}^{-3}$ ).<sup>233</sup>

The increase in  $n_p$  also leads to a reduction of the bandgap energy or a bandgap renormalization (BGR), which does not affect  $\lambda_s$  at a certain carrier density.<sup>232</sup> The resulting reduced bandgap is often described as  $E'_g$  (see Fig. 27) to distinguish it from the bandgap without renormalization  $E_g$ .<sup>230</sup> In highly photoexcited semiconductors, the exchange energy increases the average distance

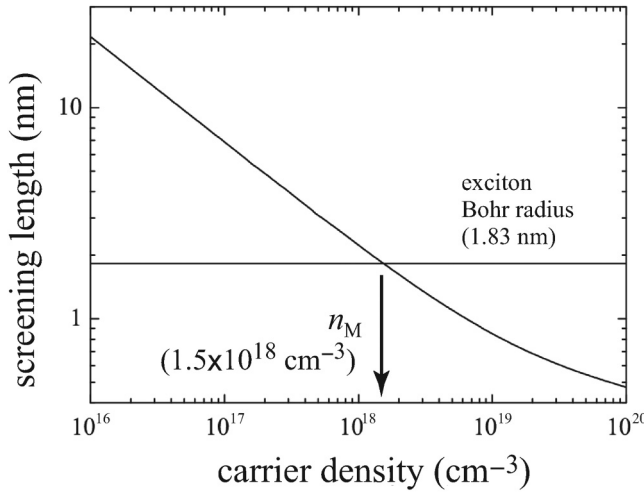


**FIG. 28.** Screening length at 300 K obtained from Eq. (26) vs carrier density. The horizontal line indicates the exciton Bohr radius. The Mott density  $n_M$  is shown as an arrow. Reproduced with permission from M. A. M. Versteegh *et al.*, Phys. Rev. B **84**, 035207 (2011). Copyright 2011 the American Physical Society.

between electrons with parallel spin. This has the effect to reduce their total repulsive Coulomb energy and hence lowers the total energy of the electron system, accounting for the BGR.<sup>230</sup> Also, recent DFT calculations have demonstrated that the nonparabolic nature of the host conduction band is also responsible for the BGR.<sup>249</sup> In uni-polar plasma of electrons in highly chemically doped ZnO,<sup>250–252</sup> the expected bandgap narrowing is not actually observed in the optical gap of ZnO as it is largely compensated by band filling of the conduction band (Burstein–Moss effect).<sup>253,254</sup> It

should be noted, however, that even in an EHP there still exists the Coulomb interaction between photogenerated conduction-band electron and a rather localized valence-band hole.<sup>230</sup> This can lead to an enhancement of the optical absorption and luminescence near the Fermi edge coined as Fermi edge singularity and Mahan exciton,<sup>255</sup> which is still a topic of intense research in the field of highly doped and highly excited semiconductors.<sup>234–260</sup>

Next, we turn to the condition of the optical gain in an EHP. The Femi-Dirac distribution function  $f(E)$  for electrons with energy  $E_1$  in the valence band and for those with energy  $E_2$  in the conduction band can be written by

$$f_v(E_1) = \frac{1}{\exp\left(\frac{E_1 - \mu_h}{k_B T}\right) + 1}, \quad (29)$$

$$f_c(E_2) = \frac{1}{\exp\left(\frac{E_2 - \mu_e}{k_B T}\right) + 1}. \quad (30)$$

As for the interband processes, the rates of stimulated emission  $r_{\text{stim}}$  and absorption  $r_{\text{abs}}$  for light with a spectral distribution  $u(\nu)$  are given by<sup>243</sup>

$$r_{\text{stim}}(h\nu) = B_{21}u(\nu)\rho(\nu)f_e(\nu), \quad (31)$$

$$r_{\text{abs}}(h\nu) = B_{12}u(\nu)\rho(\nu)f_a(\nu), \quad (32)$$

where  $B_{21}(B_{12})$  is the Einstein coefficient of stimulated emission (absorption),  $\rho(\nu)$  is the joint density of electron and hole states in the bands, and  $f_e(\nu) = f_c(E_2)[1 - f_v(E_1)]$  and  $f_a(\nu) = f_v(E_1)[1 - f_c(E_2)]$  are the probabilities of photon emission and absorption, respectively. Considering the equality

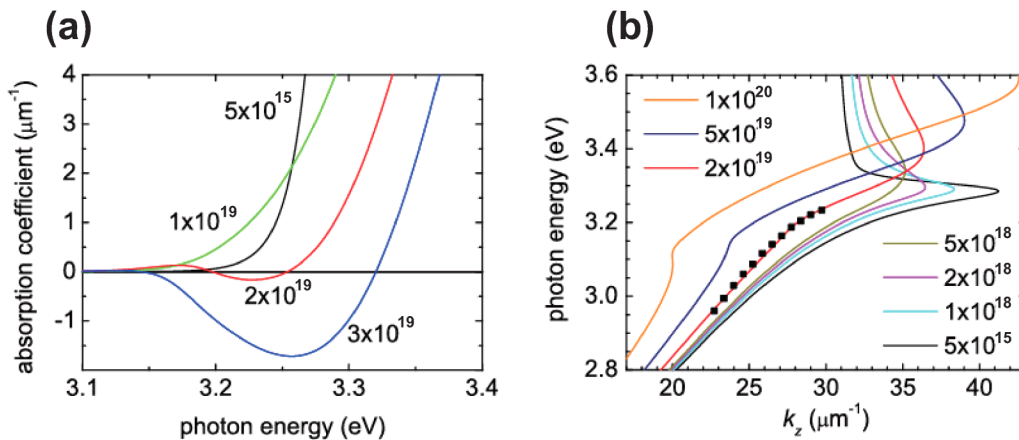


**FIG. 29.** Results of many-body calculations for ZnO at  $T = 300$  K for polarization  $\mathbf{E} \perp \mathbf{c}$ . Electron–hole densities are indicated in  $\text{cm}^{-3}$ . (a) Absorption spectra at four electron–hole pair densities, showing that gain starts at  $2 \times 10^{19} \text{ cm}^{-3}$ . (b) Dispersion relations for light inside a ZnO nanowire with dimensions  $L_x = L_y = 200$  nm for several densities. Squares indicate measured Fabry–Pérot modes reported in Ref. 178. Reproduced with permission from M. A. M. Versteegh *et al.*, Phys. Rev. Lett. **108**, 157402 (2012). Copyright 2012 the American Physical Society.

07 June 2024 05:50:37

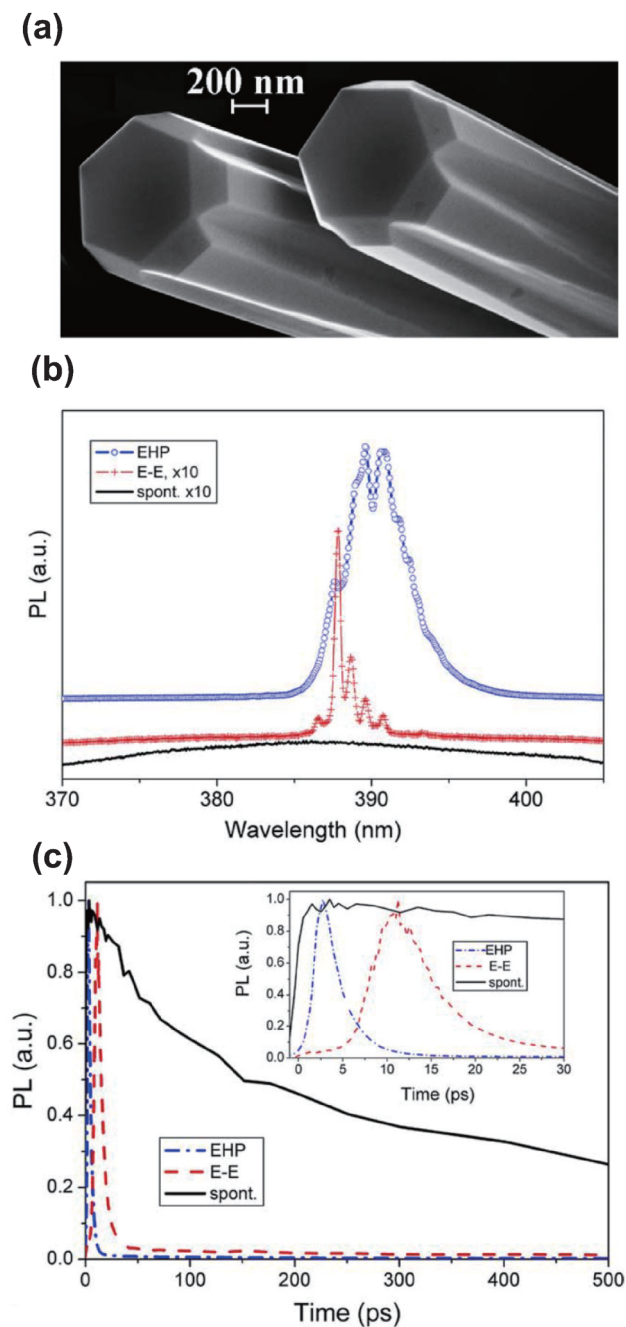


**FIG. 30.** (a) A representative SEM image of ZnO columns grown on Si substrates. (b) Time-resolved PL spectra for spontaneous emission (shown at 4 ps), stimulated emission due to exciton–exciton scattering (shown at 8 ps due to a longer delay time), and stimulated emission due to EHP (shown at 4 ps). Due to very high intensity emission in the EHP regime, the other two spectra have been multiplied by a factor 10 to improve the clarity of presentation. (c) Decay curves for three different emission regimes. The inset shows the enlarged region in the range from  $-1$  to  $30$  ps. Reproduced with permission from W. M. Kwok *et al.*, *Chem. Phys. Lett.* **412**, 141 (2005). Copyright 2005 Elsevier.

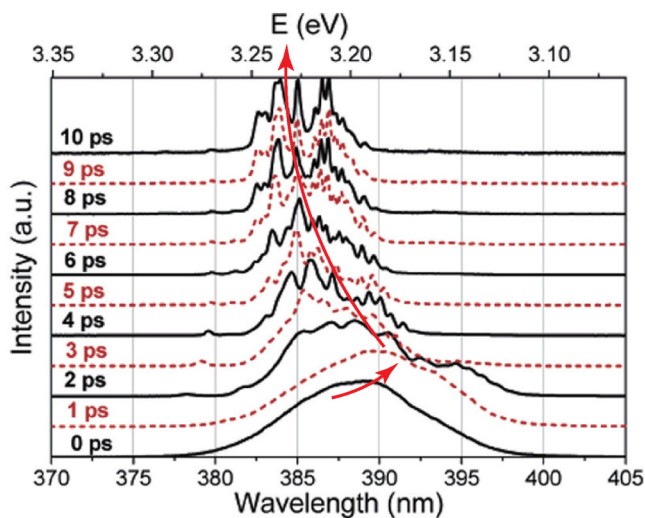


**FIG. 31.** Time-resolved photoluminescence from ZnO tetrapod nanowires, showing the transition from EHP to excitonic lasing regime. Reproduced with permission from A. B. Djurišić *et al.*, *J. Phys. Chem. B* **109**, 19228 (2005). Copyright 2005 American Chemical Society.

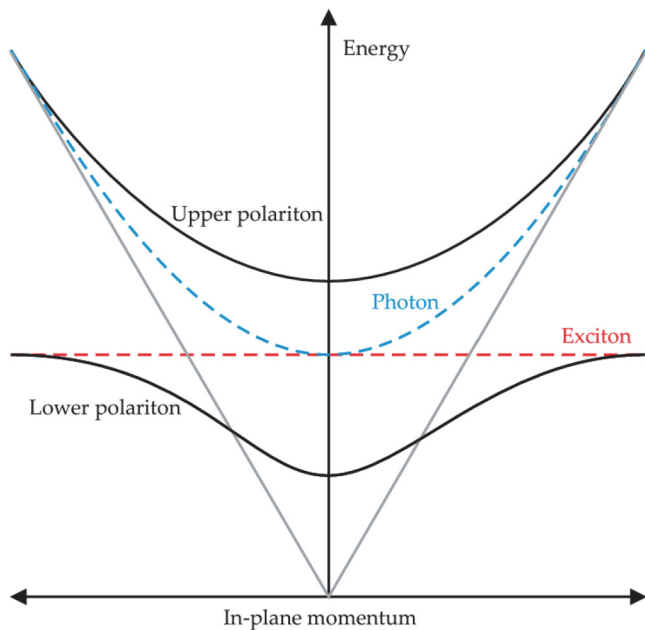


**FIG. 32.** The dispersion relation for a photon in an optical cavity is parabolic for small in-plane momentum and converges to the free photon dispersion (gray lines) at larger momentum. When one mode is tuned to the energy of an electronic excitation, or exciton, exciton–photon coupling inside the cavity gives rise to new hybrid modes (black), known as polaritons. Reproduced with permission from D. W. Snoke and J. Keeling, *Phys. Today* **70**, 54 (2017). Copyright 2017 AIP Publishing LLC.

07 June 2024 05:50:37



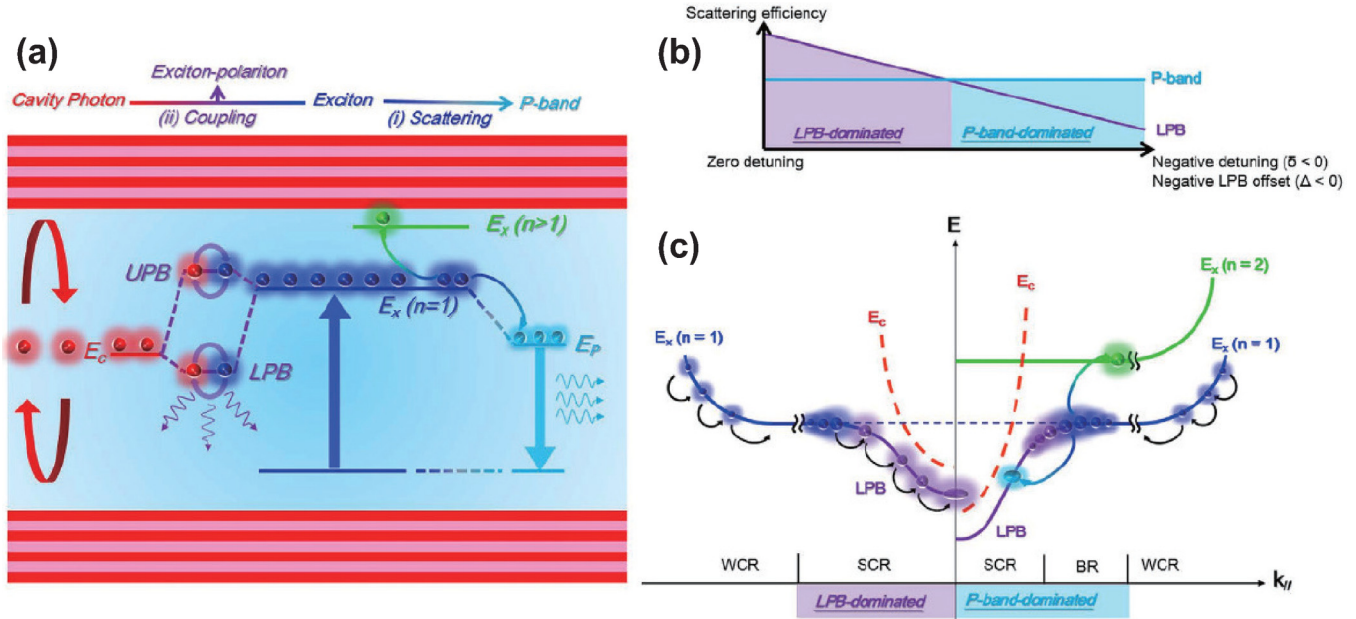


**FIG. 33.** Schematic illustrations of exciton transition channels in a strong coupled ZnO microcavity (MC). (a) Excitonic-related lasing mechanisms in the strongly coupled ZnO MC. Different states in a strongly coupled ZnO MC including photons (red), ground-state excitons (navy blue), exciton–polaritons (blue-violet) and exciton–exciton (X-X, or P-band) recombinations (sky blue) are represented by different colors. (b) Schematic of scattering efficiency trade-off between P-band and polaritons vs the negative detuning and LPB-offset of cavity. The X-X scattering is independent of the detuning parameter but increases with the exciton density, while the polariton scattering decreases with the detuning parameter. (c) Schematic of the dispersions of a small negatively detuned MC (left side) and a large negatively detuned MC (right side). The SCR, WCR, and BR indicate the strong coupling region, weak coupling region, and bottleneck region, respectively. Reproduced with permission from Y.-Y. Lai *et al.*, *Sci. Rep.* **6**, 20581 (2016). Copyright 2016 Author(s), licensed under a Creative Commons Attribution (CC BY) License.

07 June 2024 05:50:37

$B_{12} = B_{21} = B$ , we obtain the resulting rate of observable stimulated emission,

$$R_{\text{stim}}(h\nu) = r_{\text{stim}}(h\nu) - r_{\text{abs}}(h\nu) = Bu(\nu)\rho(\nu)[f_c(E_2) - f_v(E_1)]. \quad (33)$$

Hence, the sign of  $R_{\text{stim}}(h\nu)$  is determined by the sign of the term  $f_c(E_2) - f_v(E_1)$ . From Fig. 27, one sees that

$$E_2 = E_1 + h\nu, \quad (34)$$

$$\mu_{e'} = \mu_{h'} + E_{g'} + F_h + F_e. \quad (35)$$

By using Eqs. (29), (30), (34), and (35), one finds that sign of the term  $f_c(E_2) - f_v(E_1)$  is eventually controlled by the following numerator term:<sup>243</sup>

$$1 - \exp\left(\frac{h\nu - E_{g'} - F_h - F_e}{k_B T}\right). \quad (36)$$

It, thus, follows that  $R_{\text{stim}}(h\nu)$  becomes positive when  $h\nu < E_{g'} + F_h + F_e$ , which limits the high-energy end of the gain. One also notices from Fig. 27 that the lowest photon energy amplified in the quasi-equilibrium state is  $h\nu = E_{g'}$ . Consequently, the

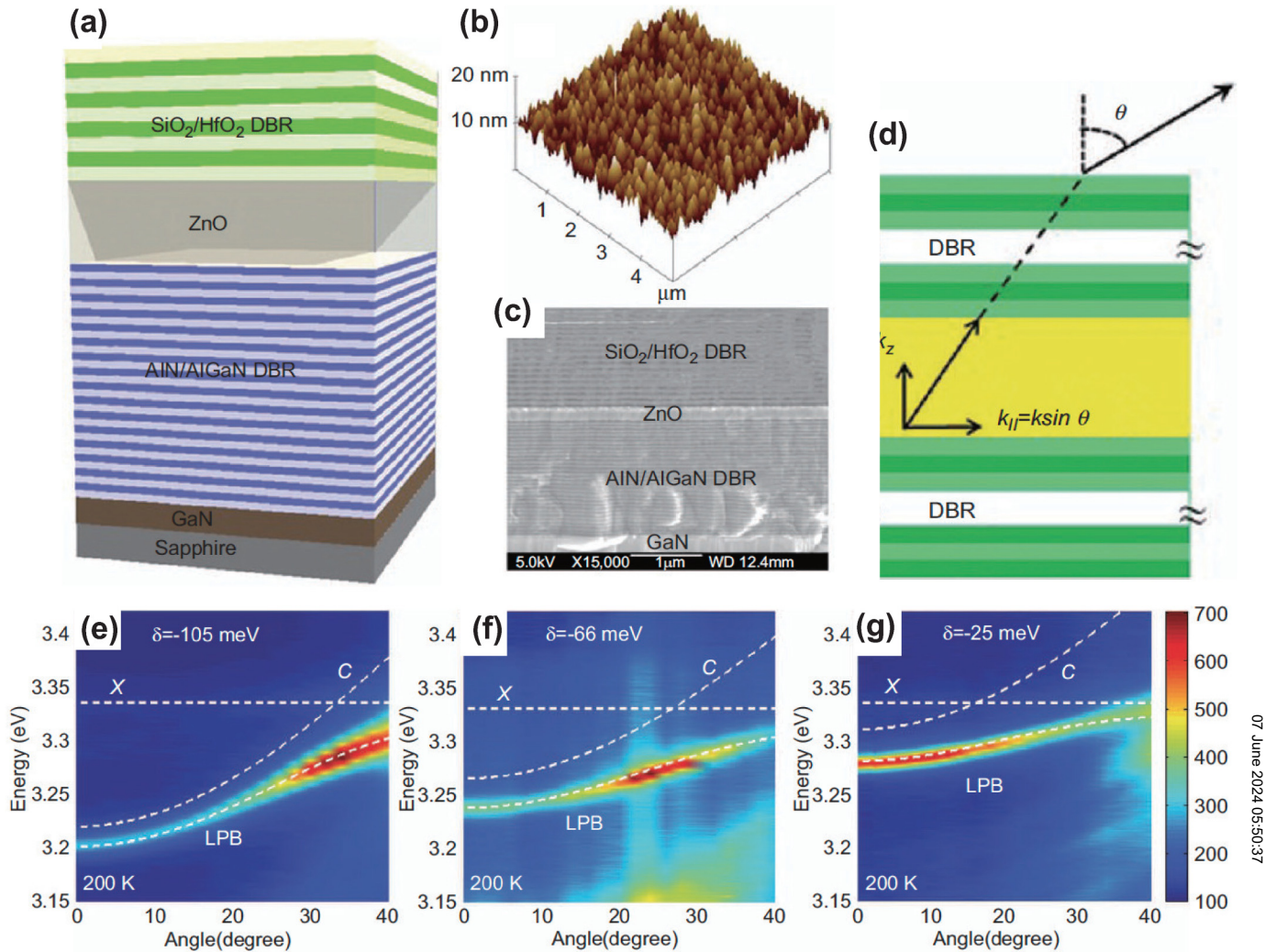
optical gain in an EHP is expected to occur in the following energy range, which is known as the Bernard–Duraffourg condition for net optical gain in semiconductors<sup>261</sup> [see Fig. 27(c)],

$$E_{g'} < h\nu < E_{g'} + F_h + F_e = \mu_{e'} - \mu_{h'}. \quad (37)$$

The term  $\mu_{e'} - \mu_{h'}$  is referred to as the chemical potential of an EHP system ( $\mu_{\text{EHP}}$ ).<sup>230</sup> In the EHP regime, the observed emission spectra show a substantial redshift and spectral broadening with increasing excitation intensity due to the reduction of  $E_{g'}$ .<sup>230,243</sup> According to the quantum many-body theory developed by Versteegh *et al.*<sup>232</sup> it is possible to calculate an optical gain spectrum  $g(\omega)$  for a certain  $n_p$  at a particular temperature of interest using the complex susceptibility  $\chi(\omega)$  as follows:

$$g(\omega) = -\frac{2\omega}{c} \text{Im}\sqrt{1 + \chi(\omega)}, \quad (38)$$

where  $c$  is the vacuum speed of light. As shown in Fig. 29(a), the theoretical gain spectra at 300 K satisfactorily reproduce the changes in the EHP spectra for increasing electron–hole pair densities.<sup>206</sup> One also sees from Fig. 29(a) that an optical gain or a negative absorption coefficient is observed for the spectrum of  $n_p = 2 \times 10^{19} \text{ cm}^{-3}$ , which is about one order of magnitude higher than  $n_M = 1.5 \times 10^{18} \text{ cm}^{-3}$ , indicating the occurrence of an inverted EHP



07 June 2024 05:50:37

**FIG. 34.** (a) Schematic diagram of the hybrid ZnO microcavity (MC9). (b) Atomic force microscopy (AFM) image of the ZnO cavity. (c) Cross-sectional scanning electron microscopy image of the ZnO MC. (d) Schematic diagrams of the one-to-one correspondence between the internal polaritons and the external photons during the angle-resolved photoluminescence (ARPL) measurements. Color maps of the ARPL measurements for the different positions on the ZnO hybrid MC sample with three different detunings: (e)  $\delta = -105$  meV, (f)  $\delta = -66$  meV, and (g)  $\delta = -25$  meV at 200 K. Reproduced with permission from Y.-Y. Lai *et al.*, *Light: Sci. Appl.* **2**, e76 (2013). Copyright 2013 Author(s), licensed under a Creative Commons Attribution (CC BY) License.

for  $n_p > n_M$  at 300 K. This is consistent with the estimation given by Klingshirn *et al.*<sup>262</sup> who showed that the condition of population inversion given in Eq. (37) is achieved for  $n_p \approx 5 \times 10^{18} \text{ cm}^{-3}$  at 300 K.

Then, the room-temperature EHP lasing is expected to occur for  $n_p > \sim 10^{19} \text{ cm}^{-3}$  when an appropriate feedback mechanism is provided. Indeed, the F-P laser modes in ZnO nanowires<sup>206</sup> and the random laser modes in ZnO nanopowders,<sup>263</sup> both of which result most likely from EHP lasing,<sup>206,263</sup> are observed for  $n_p > \sim 10^{19} \text{ cm}^{-3}$  at room temperature. Figure 29(b) shows the theoretical dispersion relation for light inside a ZnO

nanowire with dimensions  $L_x = L_y = 200 \text{ nm}$  calculated for several carrier densities using Eq. (12) where  $n'(\omega, n_p)$  is computed in the many-body theory.<sup>206</sup> The measured F-P laser modes reported in Ref. 178 are also given in Fig. 29(b). A very good fit is obtained for  $n_p = 2 \times 10^{19} \text{ cm}^{-3}$ , giving the evidence of EHP lasing at room temperature.

Lasing characteristics of EHP can be investigated in more detail when measured at low temperatures or by using highly faceted ZnO microcrystals. Fallert *et al.*<sup>264</sup> reported changes in the EHP lasing modes at 15 K for a F-P ZnO nanorod depending on the excitation fluence. It has been demonstrated that every

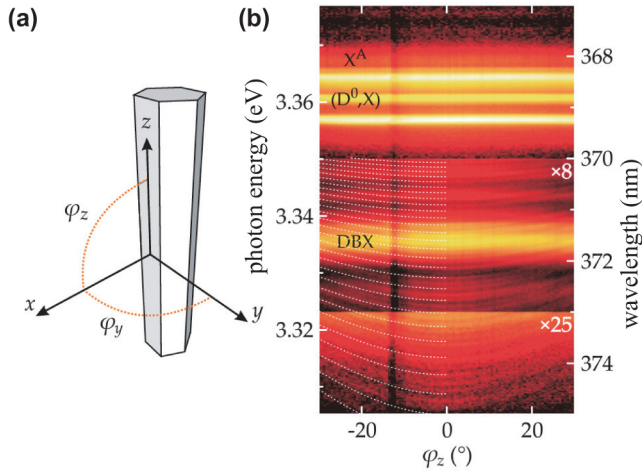


**FIG. 35.** (a) Microwire coordinate system: The  $xy$  plane coincides with the cross section plane, and the wire axis coincides with the  $z$  axis. Angles are defined accordingly. (b) PL image of a ZnO microwire recorded at cryogenic temperature. Respective ZnO-related transitions are labeled: free (X), donor-bound ( $D^0,X$ ), and defect-bound (DBX) excitons. The white dotted lines indicate modeled dispersion curves for TE-polarized polaritons. Reproduced with permission from C. P. Dietrich *et al.*, Phys. Rev. B **91**, 041202(R) (2015). Copyright 2015 the American Physical Society.

individual mode shifts to higher energies with increasing excitation fluence, demonstrating a decrease of  $n'(\omega, n_p)$  with increasing  $n_p$  in EHP. Fallert *et al.*<sup>264</sup> also reported that each individual mode shows a redshift by several meV during its decay, suggesting the recovery of the refractive index due to recombination of the carriers. It is also interesting to note that highly faceted ZnO rods with a lower threshold show a transition in the gain mechanism from excitonic to EHP recombination with increasing excitation intensity,<sup>106,265</sup> which can be identified by the excitation intensity-dependent change in the PL spectra and their decay dynamics. Figure 30 shows examples of highly faceted ZnO rods and their time-resolved PL spectra at 300 K.<sup>106</sup> A broad spontaneous emission with time constant with several hundreds of picoseconds is seen at  $\sim 380$  nm (3.26 eV) under low pump intensity. The threshold for excitonic lasing was observed to occur at  $\sim 45 \mu\text{J}/\text{cm}^2$ , showing narrow F-P lasing modes with a line width of  $\sim 0.4$  nm and rise and decay times in the range 4–5 ps. The delay in the onset of the excitonic lasing could be due to the relatively long ( $>5$  ps) time necessary for the relatively weak excitonic interaction to produce sufficient scattering events required for optical gain.<sup>265</sup> Optical pump-THz measurements also supported such slow evolution of free carriers to excitons in the range 10–100 ps following photoexcitation.<sup>233</sup> As the pump intensity increases to  $\sim 90 \mu\text{J}/\text{cm}^2$ , the spectrum becomes broad and redshifted, accompanied by substantial shortening of rise ( $\sim 1$  ps) and decay (2–3 ps) times. This can be interpreted in terms of the formation of EHP and a very fast ( $<100$  fs) cooling of the hot carriers to a quasi-thermal equilibrium.<sup>233,265</sup> We should note that the reverse transition, i.e., from EHP to excitonic lasing, can also

be observed during the decay process of the EHP emission from ZnO nanostructures with a low excitonic threshold at room temperature ( $\sim 40 \mu\text{J}/\text{cm}^2$ ).<sup>266</sup> Figure 31 shows the time-resolved PL from these ZnO nanostructures in the EHP regime created under high ( $\sim 126 \mu\text{J}/\text{cm}^2$ ) excitation fluence. The PL peak first shift to the red at 1 ps, and then start shrinking back to the blue from 2 ps, resulting in a structured emission observed in the excitonic lasing regime at 10 ps. This temporal change in the PL spectra results from the faster decay (2–3 ps) of the EHP emission and the subsequent decrease in the free carrier concentration and a consequential bandgap recovery, leading to the excitonic lasing.<sup>266</sup> These results indicate that excitons are formed as a result of the thermalization and cooling of the hot EHP gas, ending up with excitonic stimulated emissions.

## VI. EXCITON-POLARITON LASER

The excitonic and EHP lasers mentioned in Secs. V A and V B are based on a conventional concept of laser, i.e., the combination of gain medium, optical cavity, and population inversion. However, in a polariton laser, which results from the strong coupling between excitons and photons confined, for example, in a distributed Bragg reflector microcavity as will be shown later, there is no explicit requirement for electronic population inversion; but rather amplification is possible when the exciton-phonon system is inverted, i.e.,<sup>267</sup>

$$\bar{n}_{\text{exc}}(k) \geq \bar{n}_{\text{ph}}(k), \quad (39)$$

where  $\bar{n}_{\text{exc}}(k)$  and  $\bar{n}_{\text{ph}}(k)$  are the population of exciton and phonon, respectively. This condition indicates that for all modes that are contributing to ground-state exciton-phonon scattering, the exciton reservoir occupancy has to exceed that of the phonons. Qualitatively speaking, polariton lasing occurs when the total scattering rate to the ground state overcomes the polariton decay rate, which is usually dominated by mirror loss.<sup>18</sup> In ZnO, relaxation pathways to the ground state are assisted via acoustic phonons, LO phonons, and exciton-exciton scattering. The condition for polariton lasing can be fulfilled at carrier densities much lower than  $n_M$ . Note, however, that at higher carrier densities beyond  $n_M$ , the exciton binding energy is screened by the carriers (see Sec. V B), and accordingly a polariton laser is expected to continuously transform into a conventional EHP laser.<sup>268</sup> Hence, both polariton and standard lasers can be, in principle, achieved with the same cavity; that is, polariton (standard) lasing occurs in the regime of strong (weak) light-matter coupling, at pump intensities two or three orders of magnitude smaller (larger) than the threshold for standard (polariton) lasing.<sup>269</sup>

The strong interaction between exciton and photon within an optical cavity gives rise to two new sets of states, i.e., upper and lower polariton branches (UPB and LPB, respectively, see Fig. 32). The resulting hybrid states have properties derived both from exciton and photon, yielding an energy minimum at  $k=0$ . Although the concept of polariton has been common for decades in the field of semiconductor optics,<sup>230</sup> especially in ZnO,<sup>2,50,74,270</sup> strong exciton-photon coupling and related lasing phenomena in ZnO-based microcavities have not been realized until

07 June 2024 05:50:37

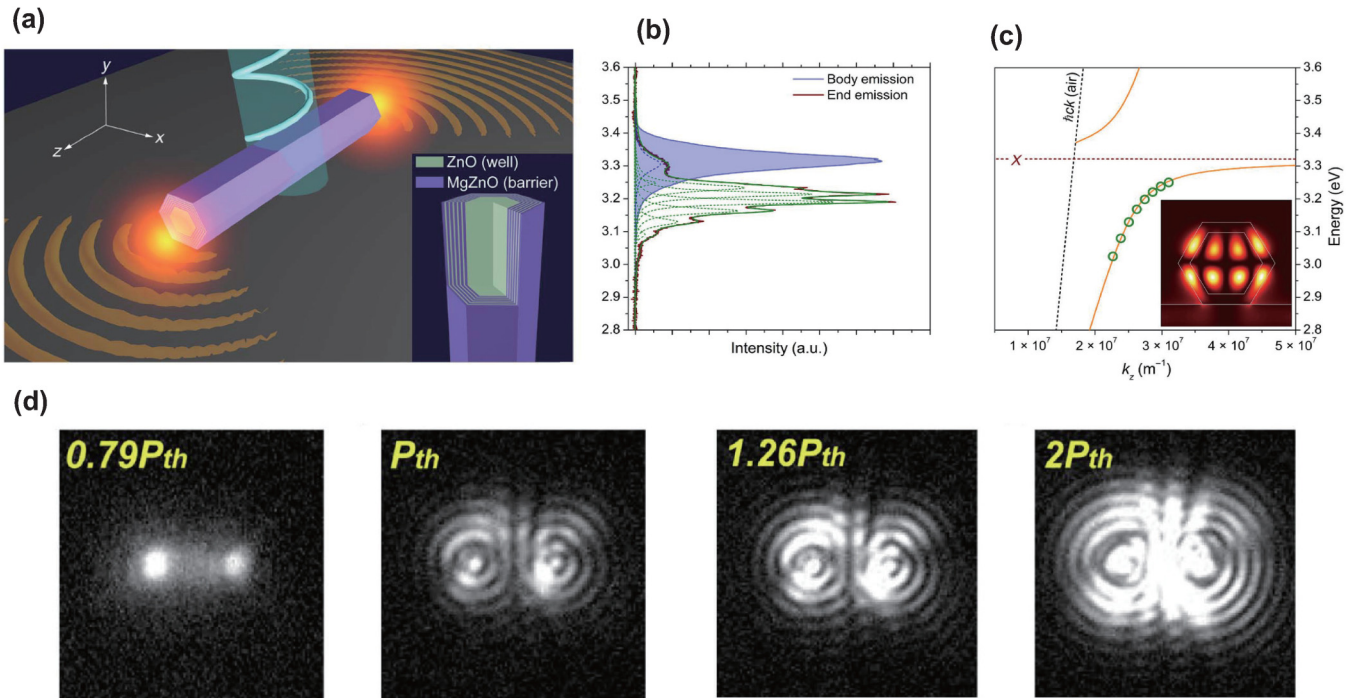


**FIG. 36.** (a) Schematic illustration of a single nanorod polariton laser on an  $\text{SiO}_2$  substrate. The inset shows the shell structure, consisting of five pairs of  $\text{Zn}_{0.9}\text{Mg}_{0.1}\text{O}/\text{ZnO}$  quantum well (QW) layers. (b) Excitonic (blue line) and waveguided (red line) PL spectra from the body center and end of a QW nanorod (diameter, 640 nm; length, 2.75  $\mu\text{m}$ ), respectively. The end emission exhibits multiple resonance peaks, which correspond to the eigenmodes of the exciton polaritons in the quantum heterostructure nanocavity. The dashed green lines represent the fitted Lorentzian line shapes used to determine the resonance energies in the lower polariton branch. The overall fitting line is displayed by the green line. (c) Dispersion relation of the exciton polaritons along the long axis of the QW nanorod. The data points represent measured resonance energies with equidistant momenta at integer values of  $\pi/L_z$ , where  $L_z$  is the length of the nanorod. The orange solid line represents the fit to the theoretical model for the exciton polariton HE22-guided mode, indicating an estimated Rabi splitting energy of  $\sim 370$  meV. The horizontal red dashed line represents the QW exciton energy. The inset shows the calculated electric field intensity ( $|E_y|^2$ ) profile in the radial cross-sectional plane for the HE22-guided mode at an energy of 3.20 eV, where white lines indicate the QW region. (d) Optical images showing a transition from spontaneous to coherent emission with increasing pump fluence. The interference patterns associated with longitudinal Fabry–Pérot cavity modes are observed. Reproduced with permission from J.-W. Kang *et al.*, *Sci. Adv.* **5**, eaau9338 (2019). Copyright 2019 Author(s), licensed under a Creative Commons Attribution (CC BY) License.

recently.<sup>271–282</sup> ZnO is beneficial for exciton–polariton lasers from two standpoints: one is a stable excitonic state up to room temperature and the other is a larger oscillator strength and, thus, the larger coupling coefficient, called the Rabi splitting energy  $\Omega \sim \sqrt{f/V_m}$ ,<sup>18</sup> where  $f$  is the oscillator strength of the excitons and  $V_m$  is the mode volume of the cavities.<sup>283</sup> In Zn-based microcavities, the Rabi splitting energy can exceed  $\sim 100$  meV,<sup>18,276</sup> which is larger than the exciton binding energy of 60 meV, hence allowing the energy overlap between the UPB and the scattering states. It should be noted that the large exciton binding energy in ZnO is beneficial for exciton lasing as well (see Sec. V A). Hence, one can observe a crossover from polariton lasing to exciton lasing in strongly coupled ZnO microcavities depending on the degree of cavity detuning  $\delta = E_c - E_x$ ,<sup>284</sup> where  $E_c$  is the cavity photon energy and  $E_x$  is the exciton energy, as depicted in Fig. 33.<sup>284</sup> When  $\delta$  is close to zero, the polariton lifetime is long enough to exhibit a more efficient stimulated scattering event than that of the exciton–exciton scattering event mentioned in Sec. V A. As the

cavity is more negatively detuned, the polariton lifetime becomes shorter and shorter. When the value of negative detuning draws near to the Rabi splitting energy, the poor polariton scattering leads to the so-called “bottleneck effect” in which polariton accumulates at high energy/momentum state, as illustrated in Fig. 33(c).

Microcavities with strong coupling can be obtained by sandwiching an appropriate ZnO active layer (typically  $5\lambda/4$ - or  $3\lambda/2$ -thick) between two distributed Bragg reflectors (DBRs), which act as the two cavity mirrors.<sup>277–280</sup> DBRs consist of alternating layers of semiconductors having different refractive indices. If each layer is a quarter of a wavelength thick, it follows that the reflections from each interface interfere constructively. The total reflectivity approaches unity as the number of layers increases. An example of the DBR microcavity and the results of angle-resolved PL measurements for the different portions on the microcavity with three different detunings reported by Lai *et al.*<sup>279</sup> are shown in Fig. 34. The effect of detuning mentioned earlier can be clearly recognized. Figure 34(e) shows a larger detuning case

( $\delta = -105$  meV), which is comparable to the Rabi splitting of this system (112 meV), demonstrating the polariton accumulation at  $35^\circ$  due to the bottleneck effect. For a smaller detuning case, a more efficient polariton relaxation occurs, and accordingly polaritons tend to become thermalized to the lower  $k$  state, as shown in Figs. 34(f) and 34(g).

It should be worth mentioning that in ZnO, the strong coupling condition can also be achieved without using DBRs but by exploiting high-quality ( $Q > \sim 1000$ ) hexagonal-cavity WGMs.<sup>272–276</sup> Figure 35(a) shows a coordinate system for a hexagonal microwire, and Fig. 35(b) demonstrates a typical angle-resolved PL image observed for a ZnO microwire with the inner radii of  $\sim 4 \mu\text{m}$  at 10 K.<sup>276</sup> Besides the angle-independent emissions of A-free excitons, donor-bound excitons ( $D^0X$ ), and defect-bound excitons (DBX), the observed image clearly shows dispersion behaviors of confined modes evidenced by the increase in the mode energy with the emission angle, or equivalently the wave vector.

Kang *et al.*<sup>282</sup> have reported room temperature polariton lasing from quantum well (QW) heterostructure nanocavities, each composed of a hexagonal ZnO nanorod core enclosed by a radial QW shell [see Fig. 36(a)]. The radial QW structure allows strong coupling of excitons with photons confined in a small-mode-volume ( $0.1 \mu\text{m}^3$ ) nanocavity, leading to a Rabi splitting energy of  $\sim 370$  meV. Exciton–polariton dispersion [Figs. 36(b) and 36(c)] and lasing features [Fig. 36(d)] have been reported from the QW nanorod at room temperature. Room-temperature exciton polaritons, along with related possible lasing, have also been reported to occur in other ZnO-based microcavities.<sup>272,274,278,285–287</sup> However, the realization of room-temperature polariton lasing relies strongly on the design and fabrications of microcavities with specific dimensionalities and geometries, playing a vital role in enhancing coupling between excitons and photons. The search for stable room-temperature polariton laser and related polaritonic devices using ZnO-based microcavities is still ongoing<sup>18,288</sup> and will require further investigations.

## VII. SUMMARY

In this Tutorial, we have attempted to create a picture of creation, recombination, and screening of excitons in ZnO thin films and micro/nanostructures in view of excitonic and EHP lasing. It has been shown that photoexcitation and the resulting recombination in ZnO are very versatile and rich not only in spontaneous excitonic emissions, but also in stimulated emission processes. This versatility stems partly from their diverse morphologies from one-dimensional to three-dimensional structures in the nanometer to micrometer range, which enables various kinds of feedback, including random lasing in an aggregation of nanoparticles, F–P lasing in a nanowire, and WGM lasing in a hexagonal plate. The other factor of versatility derives from its relatively large exciton binding energy. This leads to various types of excitonic and EHP stimulated emissions below and above  $n_M$ , respectively, along with polariton lasing. Thus, ZnO is a very unique and interesting wide bandgap semiconductor in terms not only of excitonic processes but also of the Mott transition physics although it still suffers from the doping asymmetry problem, i.e., the difficulty in the fabrication of stable and reproducible  $p$ -type ZnO.

## SUPPLEMENTARY MATERIAL

See supplementary material for the details of the preparation and optical absorption measurement procedures of the ZnO thin film shown in Fig. 5.

## AUTHOR DECLARATIONS

### Conflict of Interest

The authors have no conflicts to disclose.

### Author Contributions

**Aika Tashiro:** Data curation (equal); Investigation (equal); Writing – review & editing (equal). **Yutaka Adachi:** Data curation (equal); Investigation (equal); Writing – review & editing (equal). **Takashi Uchino:** Conceptualization (lead); Data curation (equal); Investigation (equal); Writing – original draft (lead); Writing – review & editing (lead).

## DATA AVAILABILITY

The data shown in Fig. 5 are available from the corresponding author upon reasonable request.

## REFERENCES

- <sup>1</sup>G. Heiland, E. Mollwo, and F. Stöckmann, in *Solid State Physics*, edited by F. Seitz and D. Turnbull (Academic, New York, 1959), Vol. 8, pp. 191–323.
- <sup>2</sup>C. Klingshirn, J. Fallert, H. Zhou, J. Sartor, C. Thiele, F. Maier-Flaig, D. Schneider, and H. Kalt, “65 years of ZnO research—Old and very recent results,” *Phys. Status Solidi (B)* **247**, 1424–1447 (2010).
- <sup>3</sup>D. C. Reynolds, D. C. Look, B. Jogai, C. W. Litton, G. Cantwell, and W. C. Harsch, “Valence-band ordering in ZnO,” *Phys. Rev. B* **60**, 2340–2344 (1999).
- <sup>4</sup>A. Teke, Ü. Özgür, S. Doğan, X. Gu, H. Morkoç, B. Nemeth, J. Nause, and H. O. Everitt, “Excitonic fine structure and recombination dynamics in single-crystalline ZnO,” *Phys. Rev. B* **70**, 195207 (2004).
- <sup>5</sup>D. M. Bagnall, Y. F. Chen, Z. Zhu, T. Yao, S. Koyama, M. Y. Shen, and T. Goto, “Optically pumped lasing of ZnO at room temperature,” *Appl. Phys. Lett.* **70**, 2230–2232 (1997).
- <sup>6</sup>D. M. Bagnall, Y. F. Chen, Z. Zhu, T. Yao, M. Y. Shen, and T. Goto, “High temperature excitonic stimulated emission from ZnO epitaxial layers,” *Appl. Phys. Lett.* **73**, 1038–1040 (1998).
- <sup>7</sup>P. Zu, Z. K. Tang, G. K. L. Wong, M. Kawasaki, A. Ohtomo, H. Koinuma, and Y. Segawa, “Ultraviolet spontaneous and stimulated emissions from ZnO microcrystallite thin films at room temperature,” *Solid State Commun.* **103**, 459–463 (1997).
- <sup>8</sup>Z. K. Tang, G. K. L. Wong, P. Yu, M. Kawasaki, A. Ohtomo, H. Koinuma, and Y. Segawa, “Room-temperature ultraviolet laser emission from self-assembled ZnO microcrystallite thin films,” *Appl. Phys. Lett.* **72**, 3270–3272 (1998).
- <sup>9</sup>H. Cao, Y. G. Zhao, S. T. Ho, E. W. Seelig, Q. H. Wang, and R. P. H. Chang, “Random laser action in semiconductor powder,” *Phys. Rev. Lett.* **82**, 2278–2281 (1999).
- <sup>10</sup>M. H. Huang, S. Mao, H. Feick, H. Yan, Y. Wu, H. Kind, E. Weber, R. Russo, and P. Yang, “Room-temperature ultraviolet nanowire nanolasers,” *Science* **292**, 1897–1899 (2001).
- <sup>11</sup>T. Makino, C. H. Chia, N. T. Tuan, H. D. Sun, Y. Segawa, M. Kawasaki, A. Ohtomo, K. Tamura, and H. Koinuma, “Room-temperature luminescence of excitons in ZnO/(Mg,Zn)O multiple quantum wells on lattice-matched substrates,” *Appl. Phys. Lett.* **77**, 975 (2000).

- <sup>12</sup>R. Yan, D. Gargas, and P. Yang, "Nanowire photonics," *Nat. Photonics* **3**, 569–576 (2009).
- <sup>13</sup>D. Vanmaekelbergh and L. K. van Vugt, "ZnO nanowire lasers," *Nanoscale* **3**, 2783 (2011).
- <sup>14</sup>M. Willander, O. Nur, Q. X. Zhao, L. L. Yang, M. Lorenz, B. Q. Cao, J. Z. Pérez, C. Czekalla, G. Zimmermann, and M. Grundmann, "Zinc oxide nanorod based photonic devices: Recent progress in growth, light emitting diodes and lasers," *Nanotechnology* **20**, 332001 (2009).
- <sup>15</sup>D. S. Wiersma, "The physics and applications of random lasers," *Nat. Phys.* **4**, 359–367 (2008).
- <sup>16</sup>D. S. Wiersma, "Disordered photonics," *Nat. Photonics* **7**, 188–196 (2013).
- <sup>17</sup>S. K. Turitsyn, S. A. Babin, D. V. Churkin, I. D. Vatnik, M. Nikulin, and E. V. Podivilov, "Random distributed feedback fibre lasers," *Phys. Rep.* **542**, 133 (2014).
- <sup>18</sup>D. Sanvitto and S. Kéna-Cohen, "The road towards polaritonic devices," *Nat. Mater.* **15**, 1061–1073 (2016).
- <sup>19</sup>Ü. Özgür, Y. I. Alivov, C. Liu, A. Teke, M. A. Reshchikov, S. Doğan, V. Avrutin, S.-J. Cho, and H. Morkoç, "A comprehensive review of ZnO materials and devices," *J. Appl. Phys.* **98**, 041301 (2005).
- <sup>20</sup>A. B. Djurišić and Y. H. Leung, "Optical properties of ZnO nanostructures," *Small* **2**, 944–961 (2006).
- <sup>21</sup>L. Schmidt-Mende and J. L. MacManus-Driscoll, "ZnO—Nanostructures, defects, and devices," *Mater. Today* **10**, 40–48 (2007).
- <sup>22</sup>C. Klingshirn, "ZnO: From basics towards application," *Phys. Status Solidi (B)* **244**, 3027–3073 (2007).
- <sup>23</sup>A. B. Djurišić, A. M. C. Ng, and X. Y. Chen, "ZnO nanostructures for optoelectronics: Material properties and device applications," *Prog. Quant. Electron.* **34**, 191–259 (2010).
- <sup>24</sup>X. S. Fang, Y. Bando, U. K. Gautam, T. Y. Zhai, H. B. Zeng, X. J. Xu, M. Y. Liao, and D. Golberg, "ZnO and ZnS nanostructures: Ultraviolet-light emitters, lasers, and sensors," *Crit. Rev. Solid State Mater. Sci.* **34**, 190 (2009).
- <sup>25</sup>Y. W. Heo, D. P. Norton, L. C. Tien, Y. Kwon, B. S. Kang, F. Ren, S. J. Pearton, and J. R. LaRoche, "ZnO nanowire growth and devices," *Mater. Sci. Eng. Rep.* **47**, 1 (2004).
- <sup>26</sup>S. Rahaa and M. Ahmaruzzaman, "ZnO nanostructured materials and their potential applications: Progress, challenges and perspectives," *Nanoscale Adv.* **4**, 1868–1925 (2022).
- <sup>27</sup>C. F. Klingshirn, B. K. Meyer, A. Waag, A. Hoffmann, and J. Geurts, *Zinc Oxide: From Fundamental Properties Towards Novel Applications*, Springer Series in Materials Science (Springer, Berlin, 2010).
- <sup>28</sup>C. Jagadish and S. Pearton, *Zinc Oxide Bulk, Thin Films and Nanostructures* (Elsevier, Amsterdam, 2006).
- <sup>29</sup>H. Morkoç and Ü. Özgür, *Zinc Oxide: Fundamentals, Materials and Device Technology* (Wiley-VCH, Weinheim, 2009).
- <sup>30</sup>C. Litton, D. C. Reynolds, and T. C. Collins, *Zinc Oxide Materials for Electronic and Optoelectronic Device Applications* (Wiley, Chichester, 2011).
- <sup>31</sup>R. R. Reber, "Lattice parameters of ZnO from 4.2° to 296° K," *J. Appl. Phys.* **41**, 5063–5066 (1970).
- <sup>32</sup>H. Kartzel, W. Potzel, M. Köfferlein, W. Schiessl, M. Steiner, U. Hiller, G. M. Kalvius, D. W. Mitchell, T. P. Das, P. Blaha, K. Schwarz, and M. P. Pasternak, "Lattice dynamics and hyperfine interactions in ZnO and ZnSe at high external pressures," *Phys. Rev. B* **53**, 11425–11438 (1996).
- <sup>33</sup>Y.-N. Xu and W. Y. Ching, "Electronic, optical, and structural properties of some wurtzite crystals," *Phys. Rev. B* **48**, 4335–4351 (1993).
- <sup>34</sup>F. Decremps, F. Datchi, A. M. Saitta, A. Polian, S. Pascarelli, A. Di Cicco, J. P. Itié, and F. Baudalet, "Local structure of condensed zinc oxide," *Phys. Rev. B* **68**, 104101 (2003).
- <sup>35</sup>J. A. Spencer, A. L. Mock, A. G. Jacobs, S. Mathias, Y. Zhang, and M. J. Tadjer, "A review of band structure and material properties of transparent conducting and semiconducting oxides: Ga<sub>2</sub>O<sub>3</sub>, Al<sub>2</sub>O<sub>3</sub>, In<sub>2</sub>O<sub>3</sub>, ZnO, SnO<sub>2</sub>, CdO, NiO, CuO, and Sc<sub>2</sub>O<sub>3</sub>," *Appl. Phys. Rev.* **9**, 011315 (2022).
- <sup>36</sup>L. Y. Lim, S. Lany, Y. Jun Chang, E. Rotenberg, A. Zunger, and M. F. Toney, "Angle-resolved photoemission and quasiparticle calculation of ZnO: The need for *d* band shift in oxide semiconductors," *Phys. Rev. B* **86**, 235113 (2012).
- <sup>37</sup>M. D. Ben, F. H. da Jornada, G. Antonius, T. Rangel, S. G. Louie, J. Deslippe, and A. Canning, "Static subspace approximation for the evaluation of G<sub>0</sub>W<sub>0</sub> quasiparticle energies within a sum-over-bands approach," *Phys. Rev. B* **99**, 125128 (2019).
- <sup>38</sup>P. Schröer, P. Krüger, and J. Pollmann, "First-principles calculation of the electronic structure of the wurtzite semiconductors ZnO and ZnS," *Phys. Rev. B* **47**, 6971–6980 (1993).
- <sup>39</sup>S. Massidda, R. Resta, M. Posternak, and A. Baldereschi, "Polarization and dynamical charge of ZnO within different one-particle schemes," *Phys. Rev. B* **52**, R16977–R16980 (1995).
- <sup>40</sup>B.-C. Shih, Y. Xue, P. Zhang, M. L. Cohen, and S. G. Louie, "Quasiparticle band gap of ZnO: High accuracy from the conventional G<sup>0</sup>W<sup>0</sup> approach," *Phys. Rev. Lett.* **105**, 146401 (2010).
- <sup>41</sup>C. Friedrich, M. C. Müller, and S. Blügel, "Band convergence and linearization error correction of all-electron GW calculations: The extreme case of zinc oxide," *Phys. Rev. B* **83**, 081101(R) (2011). Erratum *Phys. Rev. B* **84**, 039906 (2011).
- <sup>42</sup>L. Hedin, "New method for calculating the one-particle Green's function with application to the electron-gas problem," *Phys. Rev.* **139**, A796–A823 (1965).
- <sup>43</sup>M. S. Hybertsen and S. G. Louie, "Electron correlation in semiconductors and insulators: Band gaps and quasiparticle energies," *Phys. Rev. B* **34**, 5390–5413 (1986).
- <sup>44</sup>D. Vogel, P. Krüger, and J. Pollmann, "Ab initio electronic-structure calculations for II-VI semiconductors using self-interaction-corrected pseudopotentials," *Phys. Rev. B* **52**, R14316–R14319 (1995).
- <sup>45</sup>M. Goano, F. Bertazzi, M. Penna, and E. Bellotti, "Electronic structure of wurtzite ZnO: Nonlocal pseudopotential and ab initio calculations," *J. Appl. Phys.* **102**, 083709 (2007).
- <sup>46</sup>C. A. Ataide, R. R. Pelá, M. Marques, L. K. Teles, J. Furthmüller, and F. Bechstedt, "Fast and accurate approximate quasiparticle band structure calculations of ZnO, CdO, and MgO polymorphs," *Phys. Rev. B* **95**, 045126 (2017).
- <sup>47</sup>L. C. L. Y. Voon, M. Willatzen, M. Cardona, and N. E. Christensen, "Terms linear in *k* in the band structure of wurtzite-type semiconductors," *Phys. Rev. B* **53**, 10703–10714 (1996).
- <sup>48</sup>C. Klingshirn, H. Priller, M. Decker, J. Brückner, H. Kalt, R. Hauschild, J. Zeller, A. Waag, A. Bakin, H. Wehmann, H. W. K. Thonke, R. Sauer, R. Kling, F. Reuss, and C. Kirchner, *Adv. Solid State Phys.* **45**, 275–287 (2005).
- <sup>49</sup>B. K. Meyer, H. Alves, D. M. Hofmann, W. Kriegeis, D. Forster, F. Bertram, J. Christen, A. Hoffmann, M. Straßburg, M. Dworzak, U. Haboek, and A. V. Rodina, "Bound exciton and donor–acceptor pair recombinations in ZnO," *Phys. Status Solidi (B)* **241**, 231–260 (2004).
- <sup>50</sup>C. F. Klingshirn, in *Zinc Oxide From Fundamental Properties Towards Novel Applications*, Springer Series in Materials Science, edited by C. F. Klingshirn, B. K. Meyer, A. Waag, A. Hoffmann, and J. Geurts (Springer, Berlin, 2010), pp. 121–168.
- <sup>51</sup>D. G. Thomas, "The exciton spectrum of zinc oxide," *J. Phys. Chem. Solids* **15**, 86–96 (1960).
- <sup>52</sup>J. Hopfield, "Fine structure in the optical absorption edge of anisotropic crystals," *J. Phys. Chem. Solids* **15**, 97–107 (1960).
- <sup>53</sup>J. E. Rowe, M. Cardona, and F. H. Pollak, "Valence band symmetry and deformation potentials of ZnO," *Solid. State Commun.* **6**, 239–242 (1968).
- <sup>54</sup>Y. S. Park, C. W. Litton, T. C. Collins, and D. C. Reynolds, "Exciton spectrum of ZnO," *Phys. Rev.* **143**, 512–519 (1966).
- <sup>55</sup>B. Gil, "Oscillator strengths of A, B, and C excitons in ZnO films," *Phys. Rev. B* **64**, 201310(R) (2001).
- <sup>56</sup>S. F. Chichibu, T. Sota, G. Cantwell, D. B. Eason, and C. W. Litton, "Polarized photoreflectance spectra of excitonic polaritons in a ZnO single crystal," *J. Appl. Phys.* **93**, 756–758 (2003).
- <sup>57</sup>S. F. Chichibu, A. Uedono, A. Tsukazaki, T. Onuma, M. Zamfirescu, A. Ohtomo, A. Kavokin, G. Cantwell, C. W. Litton, T. Sota, and M. Kawasaki, "Exciton–polariton spectra and limiting factors for the room-temperature photoluminescence efficiency in ZnO," *Semicond. Sci. Technol.* **20**, S67–S77 (2005).

- <sup>58</sup>K. Hazu, S. F. Chichibu, S. Adachi, and T. Sota, "Valence-band-ordering of a strain-free bulk ZnO single crystal identified by four-wave-mixing spectroscopy technique," *J. Appl. Phys.* **111**, 093522 (2012).
- <sup>59</sup>A. Takagi, A. Nakamura, A. Yoshioka, S. Yoshioka, S. Adachi, S. F. Chichibu, and T. Sota, "Signatures of  $\Gamma_1$ - $\Gamma_5$  mixed-mode polaritons in polarized reflectance spectra of ZnO," *J. Phys.: Condens. Matter* **24**, 415801 (2012).
- <sup>60</sup>K. Hümmer, "Manifestation of k-linear term effects on the Zeeman splitting of the A1-exciton emission lines in ZnO," *Phys. Status Solidi (B)* **86**, 527–533 (1978).
- <sup>61</sup>G. Blattner, G. Kurtze, G. Schmieder, and C. Klingshirn, "Influence of magnetic fields up to 20 T on excitons and polaritons in CdS and ZnO," *Phys. Rev. B* **25**, 7413–7427 (1982).
- <sup>62</sup>A. V. Rodina, M. Strassburg, M. Dworzak, U. Haboek, A. Hoffmann, A. Zeuner, H. R. Alves, D. M. Hofmann, and B. K. Meyer, "Magneto-optical properties of bound excitons in ZnO," *Phys. Rev. B* **69**, 125206 (2004).
- <sup>63</sup>L. Ding, B. K. Li, H. T. He, W. K. Ge, J. N. Wang, J. Q. Ning, X. M. Dai, C. C. Ling, and S. J. Xu, "Classification of bound exciton complexes in bulk ZnO by magnetophotoluminescence spectroscopy," *J. Appl. Phys.* **105**, 053511 (2009).
- <sup>64</sup>L. Ding, C. Yang, H. He, J. Wang, Z. Tang, B. A. Foreman, F. Jiang, and W. Ge, "Verification of  $\Gamma_7$  symmetry assignment for the top valence band of ZnO by magneto-optical studies of the free A exciton state," *New J. Phys.* **15**, 033015 (2013).
- <sup>65</sup>M. R. Wagner, G. Callsen, J. S. Reparaz, R. Kirste, A. Hoffmann, A. V. Rodina, A. Schleife, F. Bechstedt, and M. R. Phillips, "Effects of strain on the valence band structure and exciton-polariton energies in ZnO," *Phys. Rev. B* **88**, 235210 (2013).
- <sup>66</sup>W. R. L. Lambrecht, A. V. Rodina, S. Limpijumngong, B. Segall, and B. K. Meyer, "Valence-band ordering and magneto-optic exciton fine structure in ZnO," *Phys. Rev. B* **65**, 075207 (2002).
- <sup>67</sup>R. Laskowski and N. Egede Christensen, "Ab initio calculation of excitons in ZnO," *Phys. Rev. B* **73**, 045201 (2006).
- <sup>68</sup>A. Schleife, C. Rödl, F. Fuchs, J. Furthmüller, and F. Bechstedt, "Strain influence on valence-band ordering and excitons in ZnO: An ab initio study," *Appl. Phys. Lett.* **91**, 241915 (2007).
- <sup>69</sup>B. Hönerlage, R. Lévy, J. B. Grun, C. Klingshirn, and K. Bohnert, "The dispersion of excitons, polaritons and biexcitons in direct-gap semiconductors," *Phys. Rep.* **124**, 161–253 (1985).
- <sup>70</sup>W. Y. Liang and A. D. Yoffe, "Transmission spectra of ZnO single crystals," *Phys. Rev. Lett.* **20**, 59–62 (1968).
- <sup>71</sup>S. F. Chichibu, A. Tsukazaki, M. Kawasaki, K. Tamura, Y. Segawa, T. Sota, and H. Koinuma, "Photoreflectance spectra of a ZnO heteroepitaxial film on the nearly lattice matched  $\text{ScAlMgO}_4$  (0001) substrate grown by laser molecular-beam epitaxy," *Appl. Phys. Lett.* **80**, 2860 (2002).
- <sup>72</sup>S. Tsoi, X. Lu, A. K. Ramdas, H. Alawadhi, M. Grimsditch, M. Cardona, and R. Lauck, "Isotopic-mass dependence of the A, B, and C excitonic band gaps in ZnO at low temperatures," *Phys. Rev. B* **74**, 165203 (2006).
- <sup>73</sup>K. Hümmer, "Interband magnetoreflection of ZnO," *Phys. Status Solidi (B)* **56**, 249–260 (1973).
- <sup>74</sup>J. Fryar, E. McGlynn, M. O. Henry, and J.-P. Mosnier, "Study of exciton-polariton modes in nanocrystalline thin films of ZnO using reflectance spectroscopy," *Nanotechnology* **16**, 2625–2632 (2005).
- <sup>75</sup>D. W. Hamby, D. A. Lucca, and M. J. Klopffstein, "Temperature dependent exciton photoluminescence of bulk ZnO," *J. Appl. Phys.* **93**, 3214–3217 (2003).
- <sup>76</sup>J. Rodrigues, N. B. Sedrine, M. R. Correia, and T. Monteiro, "Photoluminescence investigations of ZnO micro/nanostructures," *Mater. Today Chem.* **16**, 100243 (2020).
- <sup>77</sup>T. Nobis, E. M. Kaidashev, A. Rahm, M. Lorenz, J. Lenzner, and M. Grundmann, "Spatially inhomogeneous impurity distribution in ZnO micropillars," *Nano Lett.* **4**, 797–800 (2004).
- <sup>78</sup>L. J. Brillson, W. T. Ruane, H. Gao, Y. Zhang, J. Luo, H. von Wenckstern, and M. Grundmann, "Spatially-resolved cathodoluminescence spectroscopy of ZnO defects," *Mater. Sci. Semicond. Process.* **57**, 197–209 (2017).
- <sup>79</sup>A. R. Hutson, "Hall effect studies of doped zinc oxide single crystals," *Phys. Rev.* **108**, 222–230 (1957).
- <sup>80</sup>E. O. Kane, "Pollmann-Büttner variational method for excitonic polarons," *Phys. Rev. B* **18**, 6849–6855 (1978).
- <sup>81</sup>N. Ashkenov, B. N. Mbenkum, C. Bundesmann, V. Riede, M. Lorenz, D. Spemann, E. M. Kaidashev, A. Kasic, M. Schubert, M. Grundmann, G. Wagner, H. Neumann, V. Darakchieva, H. Arwin, and B. Monemar, "Infrared dielectric functions and phonon modes of high-quality ZnO films," *J. Appl. Phys.* **93**, 126–133 (2003).
- <sup>82</sup>N. N. Syrbu, I. M. Tiginyanu, V. V. Zalamai, V. V. Ursaki, and E. V. Rusu, "Exciton polariton spectra and carrier effective masses in ZnO single crystals," *Phys. B: Condens. Matter* **353**, 111–115 (2004).
- <sup>83</sup>R. Hauschild, H. Priller, M. Decker, J. Brückner, H. Kalt, and C. Klingshirn, "Temperature dependent band gap and homogeneous line broadening of the exciton emission in ZnO," *Phys. Status Solidi (C)* **3**, 976 (2006).
- <sup>84</sup>R. C. Rai, M. Guminiak, S. Wilser, B. Cai, and M. L. Nakarmi, "Elevated temperature dependence of energy band gap of ZnO thin films grown by e-beam deposition," *J. Appl. Phys.* **111**, 073511 (2012).
- <sup>85</sup>J. F. Muth, R. M. Kolbas, A. K. Sharma, S. Oktyabrsky, and J. Narayan, "Excitonic structure and absorption coefficient measurements of ZnO single crystal epitaxial films deposited by pulsed laser deposition," *J. Appl. Phys.* **85**, 7884–7887 (1999).
- <sup>86</sup>Y. P. Varshni, "Temperature dependence of the energy gap in semiconductors," *Physica* **34**, 149–154 (1967).
- <sup>87</sup>P. Lautenschlager, M. Garriga, S. Logothetidis, and M. Cardona, "Interband critical points of GaAs and their temperature dependence," *Phys. Rev. B* **35**, 9174–9189 (1987).
- <sup>88</sup>G. D. Cody, "Hydrogenated amorphous silicon," in *Semiconductors and Semimetals, Vol. 21, Part b*, edited by J. I. Pankove (Academic, New York, 1984), Chap. 2, pp. 42–47.
- <sup>89</sup>R. Passler, "Basic model relations for temperature dependencies of fundamental energy gaps in semiconductors," *Phys. Status Solidi (B)* **200**, 155–172 (1997).
- <sup>90</sup>L. Wang and N. C. Giles, "Temperature dependence of the free-exciton transition energy in zinc oxide by photoluminescence excitation spectroscopy," *J. Appl. Phys.* **94**, 973–978 (2003).
- <sup>91</sup>A. Tereshchenko, M. Bechelany, R. Viter, V. Khranovskyy, V. Smyntyna, N. Starodub, and R. Yakimova, "Optical biosensors based on ZnO nanostructures: Advantages and perspectives. A review," *Sens. Actuators B: Chem.* **229**, 664–677 (2016).
- <sup>92</sup>J. Rodrigues, S. O. Pereira, J. Zanoni, C. R. M. Brás, F. M. Costa, and T. Monteiro, "ZnO transducers for photoluminescence-based biosensors: A review," *Chemosensors* **10**, 39 (2022).
- <sup>93</sup>M. R. Wagner, G. Callsen, J. S. Reparaz, J.-H. Schulze, R. Kirste, M. Cobet, I. A. Ostapenko, S. Rodt, C. Nienstiel, M. Kaiser, A. Hoffmann, A. V. Rodina, M. R. Phillips, S. Lautenschlager, S. Eisermann, and B. K. Meyer, "Bound excitons in ZnO: Structural defect complexes versus shallow impurity centers," *Phys. Rev. B* **84**, 035313 (2011).
- <sup>94</sup>R. Heinhold, A. Neiman, J. V. Kennedy, A. Markwitz, R. J. Reeves, and M. W. Allen, "Hydrogen-related excitons and their excited-state transitions in ZnO," *Phys. Rev. B* **95**, 054120 (2017).
- <sup>95</sup>J. Grabowska, A. Meaney, K. K. Nanda, J.-P. Mosnier, M. O. Henry, J.-R. Duclère, and E. McGlynn, "Surface excitonic emission and quenching effects in ZnO nanowire/nanowall systems: Limiting effects on device potential," *Phys. Rev. B* **71**, 115439 (2005).
- <sup>96</sup>L. Wischmeier, T. Voss, I. Rückmann, J. Gutowski, A. C. Mofor, A. Bakin, and A. Waag, "Dynamics of surface-excitonic emission in ZnO nanowires," *Phys. Rev. B* **74**, 195333 (2006).
- <sup>97</sup>M. Biswas, Y. S. Jung, H. K. Kim, K. Kumar, G. J. Hughes, S. Newcomb, M. O. Henry, and E. McGlynn, "Microscopic origins of the surface exciton photoluminescence peak in ZnO nanostructures," *Phys. Rev. B* **83**, 235320 (2011).
- <sup>98</sup>M. Schirra, R. Schneider, A. Reiser, G. M. Prinz, M. Feneberg, J. Biskupek, U. Kaiser, C. E. Krill, K. Thonke, and R. Sauer, "Stacking fault related 3.31-eV luminescence at 130-meV acceptors in zinc oxide," *Phys. Rev. B* **77**, 125215 (2008).

- <sup>99</sup>D. Tainoff, B. Masenelli, P. Mélinon, A. Belsky, G. Ledoux, D. Amans, C. Dujardin, N. Fedorov, and P. Martin, "Competition between exciton-phonon interaction and defects states in the 3.31 eV band in ZnO," *Phys. Rev. B* **81**, 115304 (2010).
- <sup>100</sup>H. He, Q. Yang, C. Liu, L. Sun, and Z. Ye, "Size-dependent surface effects on the photoluminescence in ZnO nanorods," *J. Phys. Chem. C* **115**, 58–64 (2011).
- <sup>101</sup>L. Sun, H. He, S. Li, and Z. Ye, "Annealing-induced changes of the 3.31 eV emission in ZnO nanorods," *Appl. Phys. A* **115**, 879–883 (2014).
- <sup>102</sup>J. Rodrigues, T. Holz, R. F. Allah, D. Gonzalez, T. Ben, M. R. Correia, T. Monteiro, and F. M. Costa, "Effect of N<sub>2</sub> and H<sub>2</sub> plasma treatments on band edge emission of ZnO microrods," *Sci. Rep.* **5**, 10783 (2015).
- <sup>103</sup>D. J. Sirbully, M. Law, H. Yan, and P. Yang, "Semiconductor nanowires for subwavelength photonics integration," *J. Phys. Chem. B* **109**(32), 15190–15213 (2005).
- <sup>104</sup>S. L. Chen, S. K. Lee, W. M. Chen, H. X. Dong, L. Sun, Z. H. Chen, and I. A. Buyanova, "On the origin of suppression of free exciton no-phonon emission in ZnO tetrapods," *Appl. Phys. Lett.* **96**, 033108 (2010).
- <sup>105</sup>J. Fallert, R. Hauschild, F. Stelzl, A. Urban, M. Wissinger, H. Zhou, C. Klingshirn, and H. Kalt, "Surface-state related luminescence in ZnO nanocrystals," *J. Appl. Phys.* **101**, 073506 (2007).
- <sup>106</sup>W. M. Kwok, A. B. Djurišić, Y. H. Leung, W. K. Chan, D. L. Phillips, H. Y. Chen, C. L. Wu, S. Gwo, and M. H. Xie, "Study of excitonic emission in highly faceted ZnO rods," *Chem. Phys. Lett.* **412**, 141–144 (2005).
- <sup>107</sup>K. Appavou, X. Liu, V. Menon, and M. Y. Sfeir, "Excitonic lasing in solution-processed subwavelength nanosphere assemblies," *Nano Lett.* **16**, 2004–2010 (2016).
- <sup>108</sup>A. B. Djurišić, W. C. H. Choy, V. A. L. Roy, Y. H. Leung, C. Y. Kwong, K. W. Cheah, T. K. Gundu Rao, W. K. Chan, H. Fei Lui, and C. Surya, "Photoluminescence and electron paramagnetic resonance of ZnO tetrapod structure," *Adv. Funct. Mater.* **14**, 856–864 (2004).
- <sup>109</sup>G. Z. Xing, D. D. Wang, B. Yao, A. Q. Lloyd, F. Nien, and Y. S. Yan, "Structural characteristics, low threshold ultraviolet lasing and ultrafast carrier dynamics in high crystalline ZnO nanowire arrays," *Chem. Phys. Lett.* **515**, 132–136 (2011).
- <sup>110</sup>S.-K. Lee, S. L. Chen, D. Hongxing, L. Sun, Z. Chen, W. M. Chen, and I. A. Buyanova, "Long lifetime of free excitons in ZnO tetrapod structures," *Appl. Phys. Lett.* **96**, 083104 (2010).
- <sup>111</sup>J. Lapp, D. Thapa, J. Huso, A. Canul, M. G. Norton, M. D. McCluskey, and L. Bergman, "Enhancement of the ultraviolet photoluminescence of ZnO films: Coatings, annealing, and environmental exposure studies," *AIP Adv.* **10**, 085217 (2020).
- <sup>112</sup>W. Shan, W. Walukiewicz, J. W. Ager, III, K. M. Yu, H. B. Yuan, H. P. Xin, G. Cantwell, and J. J. Song, "Nature of room-temperature photoluminescence in ZnO," *Appl. Phys. Lett.* **86**, 191911 (2005).
- <sup>113</sup>Y. Yang, X. W. Sun, B. K. Tay, P. H. T. Cao, J. X. Wang, and X. H. Zhang, "Revealing the surface origin of green band emission from ZnO nanostructures by plasma immersion ion implantation induced quenching," *J. Appl. Phys.* **103**, 064307 (2008).
- <sup>114</sup>M. Li, G. Xing, G. Xing, B. Wu, T. Wu, X. Zhang, and T. C. Sum, "Origin of green emission and charge trapping dynamics in ZnO nanowires," *Phys. Rev. B* **87**, 115309 (2013).
- <sup>115</sup>X. Zhou, Q. Kuang, Z.-Y. Jiang, Z.-X. Xie, T. Xu, R.-B. Huang, and L.-S. Zheng, "The origin of green emission of ZnO microcrystallites: surface-dependent light emission studied by cathodoluminescence," *J. Phys. Chem. C* **111**, 12091–12093 (2007).
- <sup>116</sup>A. Gokarna, R. Aad, J. Zhou, K. Nomenyo, A. Lusson, P. Miska, and G. Lerondel, "On the origin of the enhancement of defect related visible emission in annealed ZnO micropods," *J. Appl. Phys.* **126**, 145104 (2019).
- <sup>117</sup>J. A. Röhr, J. Sá, and S. J. Konezny, "The role of adsorbates in the green emission and conductivity of zinc oxide," *Commun. Chem.* **2**, 52 (2019).
- <sup>118</sup>M. Zhang, F. Averseng, F. Haque, P. Borghetti, J.-M. Krafft, B. Baptiste, G. Costentin, and S. Stankic, "Defect-related multicolour emissions in ZnO smoke: From violet, over green to yellow," *Nanoscale* **11**, 5102–5115 (2019).
- <sup>119</sup>J. Zhou, K. Nomenyo, C. C. Cesar, A. Lusson, A. Schwartzberg, C.-C. Yen, W.-Y. Woon, and G. Lerondel, "Giant defect emission enhancement from ZnO nanowires through desulfurization process," *Sci. Rep.* **10**, 4237 (2020).
- <sup>120</sup>R. Müller, M. Mangold, F. Huber, M. Schreck, U. Herr, and K. Thonke, "Fe–Li complex emission in ZnO," *J. Appl. Phys.* **129**, 085701 (2021).
- <sup>121</sup>J. V. Foreman, H. O. Everitt, J. Yang, and J. Liu, "Influence of temperature and photoexcitation density on the quantum efficiency of defect emission in ZnO powders," *Appl. Phys. Lett.* **91**, 011902 (2007).
- <sup>122</sup>B. K. Meyer, in *Zinc Oxide from Fundamental Properties Towards Novel Applications*, Springer Series in Materials Science, edited by C. F. Klingshirn, B. K. Meyer, A. Waag, A. Hoffmann, and J. Geurts (Springer, Berlin, 2010), pp. 169–199.
- <sup>123</sup>L. Ge, Y. D. Chong, and A. Douglas Stone, "Steady-state ab initio laser theory: Generalizations and analytic results," *Phys. Rev. A* **82**, 063824 (2010).
- <sup>124</sup>H. Cao, R. Chriki, S. Bittner, A. A. Friesem, and N. Davidson, "Complex lasers with controllable coherence," *Nat. Rev. Phys.* **1**, 156–168 (2019).
- <sup>125</sup>A. Forbes, M. de Oliveira, and M. R. Dennis, "Structured light," *Nat. Photonics* **15**, 253–262 (2021).
- <sup>126</sup>D. Saxena, A. Arnaudon, O. Cipolato, M. Gaio, A. Quentel, S. Yaliraki, D. Pisignano, A. Camposeo, M. Barahona, and R. Sapienza, "Sensitivity and spectral control of network lasers," *Nat. Commun.* **13**, 6493 (2022).
- <sup>127</sup>M. C. T. Bahaa and E. A. Saleh, *Fundamentals of Photonics* (John Wiley and Sons Inc., 1991).
- <sup>128</sup>M. A. Noginov, G. Zhu, A. M. Belgrave, R. Bakker, V. M. Shalaev, E. E. Narimanov, S. Stout, E. Herz, T. Suteewong, and U. Wiesner, "Demonstration of a spaser-based nanolaser," *Nature* **460**, 1110–1112 (2009).
- <sup>129</sup>B. Bahari, A. Ndao, F. Vallini, A. El Amili, Y. Fainman, and B. Kanté, "Nonreciprocal lasing in topological cavities of arbitrary geometries," *Science* **358**, 636–640 (2017).
- <sup>130</sup>M. A. Bandres, S. Wittek, G. Harari, M. Parto, J. Ren, M. Segev, D. N. Christodoulides, and M. Khajavikhan, "Topological insulator laser: Experiments," *Science* **359**, eaar4005 (2018).
- <sup>131</sup>S. Gottardo, R. Sapienza, P. D. García, A. Blanco, D. S. Wiersma, and C. López, "Resonance-driven random lasing," *Nat. Photonics* **2**, 429–432 (2008).
- <sup>132</sup>H. Cao, "Lasing in random media," *Waves Random Media* **13**, R1–R39 (2003).
- <sup>133</sup>M. A. Noginov, *Solid-State Random Lasers* (Springer, New York, 2005).
- <sup>134</sup>A. Boschetti, A. Taschin, P. Bartolini, A. K. Tiwari, L. Pattelli, R. Torre, and D. S. Wiersma, "Spectral super-resolution spectroscopy using a random laser," *Nat. Photonics* **14**, 177–182 (2020).
- <sup>135</sup>R. Sapienza, "Determining random lasing action," *Nat. Rev. Phys.* **1**, 690–695 (2019).
- <sup>136</sup>R. Sapienza, "Controlling random lasing action," *Nat. Phys.* **18**, 976–979 (2022).
- <sup>137</sup>F. Luan, B. Gu, A. S. L. Gomes, K.-T. Yong, S. Wen, and P. N. Prasad, "Lasing in nanocomposite random media," *Nano Today* **10**, 168–192 (2015).
- <sup>138</sup>L. Sznitko, J. Mysliwiec, and A. Miniewicz, "The role of polymers in random lasing," *J. Polym. Sci. Part B: Polym. Phys.* **53**, 951–974 (2015).
- <sup>139</sup>A. S. L. Gomes, A. L. Moura, C. B. de Araújo, and E. P. Raposo, "Recent advances and applications of random lasers and random fiber lasers," *Prog. Quantum Electron.* **78**, 100343 (2021).
- <sup>140</sup>N. Padiyakkuth, S. Thomas, R. Antoine, and N. Kalarikkal, "Recent progress and prospects of random lasers using advanced materials," *Mater. Adv.* **3**, 6687–6706 (2022).
- <sup>141</sup>H. Cao, Y. G. Zhao, H. C. Ong, S. T. Ho, J. Y. Dai, J. Y. Wu, and R. P. H. Chang, "Ultraviolet lasing in resonators formed by scattering in semiconductor polycrystalline films," *Appl. Phys. Lett.* **73**, 3656–3658 (1998).
- <sup>142</sup>H. Cao, J. Y. Xu, D. Z. Zhang, S.-H. Chang, S. T. Ho, E. W. Seelig, X. Liu, and R. P. H. Chang, "Spatial confinement of laser light in active random media," *Phys. Rev. Lett.* **84**, 5584–5587 (2000).
- <sup>143</sup>H. Cao and Y. Eliezer, "Harnessing disorder for photonic device applications," *Appl. Phys. Rev.* **9**, 011309 (2022).
- <sup>144</sup>V. Milner and A. Z. Genack, "Photon localization laser: Low-threshold lasing in a random amplifying layered medium via wave localization," *Phys. Rev. Lett.* **94**, 073901 (2005).



- <sup>145</sup>P. Stano and P. Jacquod, "Suppression of interactions in multimode random lasers in the anderson localized regime," *Nat. Photonics* **7**, 66–71 (2013).
- <sup>146</sup>H. E. Türeci, L. Ge, S. Rotter, and A. D. Stone, "Strong interactions in multimode random lasers," *Science* **320**, 643–646 (2008).
- <sup>147</sup>M. Leonetti, C. Conti, and C. Lopez, "The mode-locking transition of random lasers," *Nat. Photonics* **5**, 615–617 (2011).
- <sup>148</sup>F. Antenucci, G. Lerario, B. S. Fernández, L. De Marco, M. De Giorgi, D. Ballarini, D. Sanvitto, and L. Leuzzi, "Demonstration of self-starting nonlinear mode locking in random lasers," *Phys. Rev. Lett.* **126**, 173901 (2021).
- <sup>149</sup>S. Schönhuber, M. Brandstetter, T. Hisch, C. Deutsch, M. Krall, H. Detz, A. M. Andrews, G. Strasser, S. Rotter, and K. Unterrainer, "Random lasers for broadband directional emission," *Optica* **3**, 1035 (2016).
- <sup>150</sup>P. W. Anderson, "Absence of diffusion in certain random lattices," *Phys. Rev.* **109**, 1492–1505 (1958).
- <sup>151</sup>M. Lee, S. Callard, C. Seassal, and H. Jeon, "Taming of random lasers," *Nat. Photonics* **13**, 445–448 (2019).
- <sup>152</sup>C. Conti and A. Fratallocchi, "Dynamic light diffusion, three-dimensional Anderson localization and lasing in inverted opals," *Nat. Phys.* **4**, 794–798 (2008).
- <sup>153</sup>J. Liu, P. D. Garcia, S. Ek, N. Gregersen, T. Suhr, M. Schubert, J. Mørk, S. Stobbe, and P. Lodahl, "Random nanolasing in the anderson localized regime," *Nat. Nanotechnol.* **9**, 285–289 (2014).
- <sup>154</sup>M. Gaio, D. Saxena, J. Bertolotti, D. Pisignano, A. Camposo, and R. Sapienza, "A nanophotonic laser on a graph," *Nat. Commun.* **10**, 226 (2019).
- <sup>155</sup>B. Kumar, R. Homri, Priyanka, S. K. Maurya, M. Lebental, and P. Sebbah, "Localized modes revealed in random lasers," *Optica* **8**, 1033 (2021).
- <sup>156</sup>S. P. Lau, H. Y. Yang, S. F. Yu, H. D. Li, M. Tanemura, T. Okita, H. Hatano, and H. H. Hng, "Laser action in ZnO nanoneedles selectively grown on silicon and plastic substrates," *Appl. Phys. Lett.* **87**, 013104 (2005).
- <sup>157</sup>X. H. Wu, A. Yamilov, H. Noh, H. Cao, E. W. Seelig, and R. P. H. Chang, "Random lasing in closely packed resonant scatterers," *J. Opt. Soc. Am. B* **21**, 159 (2004).
- <sup>158</sup>O. Svelto, *Principles of Lasers* (Plenum Press, New York, 1998), Chap. 2.
- <sup>159</sup>M. A. Noginov, N. E. Noginova, H. J. Caulfield, P. Venkateswarlu, T. Thompson, M. Mahdi, and V. Ostroumov, "Short-pulsed stimulated emission in the powders of  $\text{NdAl}_3(\text{BO}_3)_4$ ,  $\text{NdSc}_3(\text{BO}_3)_4$ , and  $\text{Nd}_2\text{Sr}_5(\text{PO}_4)_3\text{F}$  laser crystals," *J. Opt. Soc. Am. B* **13**, 2024 (1996).
- <sup>160</sup>M. A. Noginov, N. E. Noginova, S. U. Egarievwe, H. J. Caulfield, P. Venkateswarlu, A. Williams, and S. B. Mirov, "Color-center powder laser: The effect of pulverization on color-center characteristics," *J. Opt. Soc. Am. B* **14**, 2153 (1997).
- <sup>161</sup>T. Uchino and D. Okutsu, "Broadband laser emission from color centers inside MgO microcrystals," *Phys. Rev. Lett.* **101**, 117401 (2008).
- <sup>162</sup>T. Uchino, D. Okutsu, R. Katayama, and S. Sawai, "Mechanism of stimulated optical emission from MgO microcrystals with color centers," *Phys. Rev. B* **79**, 165107 (2009).
- <sup>163</sup>Y. Uenaka and T. Uchino, "Photoexcitation, trapping, and recombination processes of the F-type centers in lasing MgO microcrystals," *Phys. Rev. B* **83**, 195108 (2011).
- <sup>164</sup>V. M. Apalkov, M. E. Raikh, and B. Shapiro, "Random resonators and prelocalized modes in disordered dielectric films," *Phys. Rev. Lett.* **89**, 016802 (2002).
- <sup>165</sup>P. Sebbah and C. Vanneste, "Random laser in the localized regime," *Phys. Rev. B* **66**, 144202 (2002).
- <sup>166</sup>S. Mujumdar, M. Ricci, R. Torre, and D. S. Wiersma, "Amplified extended modes in random lasers," *Phys. Rev. Lett.* **93**, 053903 (2004).
- <sup>167</sup>S. Mujumdar, V. Türeci, R. Torre, and D. S. Wiersma, "Chaotic behavior of a random laser with static disorder," *Phys. Rev. A* **76**, 033807 (2007).
- <sup>168</sup>C. Vanneste, P. Sebbah, and H. Cao, "Lasing with resonant feedback in weakly scattering random systems," *Phys. Rev. Lett.* **98**, 143902 (2007).
- <sup>169</sup>J. Andreasen, A. A. Asatryan, L. C. Botten, M. A. Byrne, H. Cao, L. Ge, L. Labonté, P. Sebbah, A. D. Stone, H. E. Türeci, and C. Vanneste, "Modes of random lasers," *Adv. Opt. Photonics* **3**, 88 (2011).
- <sup>170</sup>J. Fallert, R. J. B. Dietz, J. Sartor, D. Schneider, C. Klingshirn, and H. Kalt, "Co-existence of strongly and weakly localized random laser modes," *Nat. Photonics* **3**, 279–282 (2009).
- <sup>171</sup>Z. L. Wang, "ZnO nanowire and nanobelt platform for nanotechnology," *Mater. Sci. Eng.: R. Rep.* **64**, 33–71 (2009).
- <sup>172</sup>Z. Fan and J. G. Lu, "Zinc oxide nanostructures: Synthesis and properties," *J. Nanosci. Nanotechnol.* **5**, 1561 (2005).
- <sup>173</sup>A. Kołodziejczak-Radzimska and T. Jesionowski, "Zinc oxide—From synthesis to application: A review," *Materials* **7**, 2833–2881 (2014).
- <sup>174</sup>Z. L. Wang, "Zinc oxide nanostructures: Growth, properties and applications," *J. Phys.: Condens. Matter* **16**, R829–R858 (2004).
- <sup>175</sup>M. H. Huang, Y. Wu, H. Feick, N. Tran, E. Weber, and P. Yang, "Catalytic growth of zinc oxide nanowires by vapor transport," *Adv. Mater.* **13**, 113–116 (2001).
- <sup>176</sup>Z. W. Pan, Z. R. Dai, and Z. L. Wang, "Nanobelts of semiconducting oxides," *Science* **291**, 1947–1949 (2001).
- <sup>177</sup>S. H. Dalal, D. L. Baptista, K. B. K. Teo, R. G. Lacerda, D. A. Jefferson, and W. I. Milne, "Controllable growth of vertically aligned zinc oxide nanowires using vapour deposition," *Nanotechnology* **17**, 4811–4818 (2006).
- <sup>178</sup>H.-Y. Li, S. Rühle, R. Khedoe, A. F. Koenderink, and D. Vanmaekelbergh, "Polarization, microscopic origin, and mode structure of luminescence and lasing from single ZnO nanowires," *Nano Lett.* **9**, 3515–3520 (2009).
- <sup>179</sup>D. W. Bahnemann, C. Kormann, and M. R. Hoffmann, "Preparation and characterization of quantum size zinc oxide: A detailed spectroscopic study," *J. Phys. Chem.* **91**, 3789–3798 (1987).
- <sup>180</sup>A. van Dijken, E. A. Meulenkaamp, D. Vanmaekelbergh, and A. Meijerink, "Influence of adsorbed oxygen on the emission properties of nanocrystalline ZnO particles," *J. Phys. Chem. B* **104**(18), 4355–4360 (2000).
- <sup>181</sup>G. Shi, C. M. Mo, W. L. Cai, and L. D. Zhang, "Photoluminescence of ZnO nanoparticles in alumina membrane with ordered pore arrays," *Solid State Commun.* **115**, 253–256 (2000).
- <sup>182</sup>M. Kohls, M. Bonanni, L. Spanhel, D. Su, and M. Giersig, "Green  $\text{Er}^{\text{III}}$  luminescence in fractal ZnO nanolattices," *Appl. Phys. Lett.* **81**, 3858–3860 (2002).
- <sup>183</sup>Z. Qiu, K. S. Wong, M. Wu, W. Lin, and H. Xu, "Microcavity lasing behavior of oriented hexagonal ZnO nanowhiskers grown by hydrothermal oxidation," *Appl. Phys. Lett.* **84**, 2739–2741 (2004).
- <sup>184</sup>S. Baruah and J. Dutta, "Hydrothermal growth of ZnO nanostructures," *Sci. Technol. Adv. Mater.* **10**, 013001 (2009).
- <sup>185</sup>C. Xu, J. Dai, G. Zhu, G. Zhu, Y. Lin, J. Li, and Z. Shi, "Whispering-gallery mode lasing in ZnO microcavities," *Laser Photonics Rev.* **8**, 469–494 (2014).
- <sup>186</sup>H. Dong, B. Zhou, J. Li, J. Zhan, and L. Zhang, "Ultraviolet lasing behavior in ZnO optical microcavities," *J. Materiomics* **3**, 255–266 (2017).
- <sup>187</sup>K. J. Vahala, "Optical microcavities," *Nature* **424**, 839–846 (2003).
- <sup>188</sup>D. Saxena, S. Mokkapati, P. Parkinson, N. Jiang, Q. Gao, H. H. Tan, and C. Jagadish, "Optically pumped room-temperature GaAs nanowire lasers," *Nat. Photonics* **7**, 963–968 (2013).
- <sup>189</sup>S. A. Church, R. A. Abri, P. Parkinson, and D. Saxena, "Optical characterization of nanowire lasers," *Prog. Quantum Electron.* **85**, 100408 (2022).
- <sup>190</sup>Y. Ma, X. Guo, X. Wu, L. Dai, and L. Tong, "Semiconductor nanowire lasers," *Adv. Opt. Photonics* **5**, 216 (2013).
- <sup>191</sup>M. A. Zimmmer, F. Capasso, S. Müller, and C. Ronning, "Optically pumped nanowire lasers: Invited review," *Semicond. Sci. Technol.* **25**, 024001 (2010).
- <sup>192</sup>F. Vollmer and S. Arnold, "Whispering-gallery-mode biosensing: Label-free detection down to single molecules," *Nat. Methods* **5**, 591–596 (2008).
- <sup>193</sup>V. S. Ilchenko and A. B. Matsko, "Optical resonators with whispering-gallery modes—part II: Applications," *IEEE J. Sel. Top. Quantum Electron.* **12**, 15–32 (2006).
- <sup>194</sup>A. Chiasera, Y. Dumeige, P. Féron, M. Ferrari, Y. Jestin, G. Nunzi Conti, S. Pelli, S. Soria, and G. C. Righini, "Spherical whispering-gallery-mode microresonators," *Laser Photonics Rev.* **4**, 457–482 (2010).
- <sup>195</sup>L. He, S. K. Özdemir, and L. Yang, "Whispering gallery microcavity lasers," *Laser Photonics Rev.* **7**, 60–82 (2013).

- <sup>196</sup>S. Yang, Y. Wang, and H. Sun, "Advances and prospects for whispering gallery mode microcavities," *Adv. Opt. Mater.* **3**, 1136–1162 (2015).
- <sup>197</sup>Y. Chen, Y. Yin, L. Ma, and O. G. Schmidt, "Recent progress on optoplasmonic whispering-gallery-mode microcavities," *Adv. Opt. Mater.* **9**, 2100143 (2021).
- <sup>198</sup>A. V. Maslov and C. Z. Ning, "Reflection of guided modes in a semiconductor nanowire laser," *Appl. Phys. Lett.* **83**, 1237–1239 (2003).
- <sup>199</sup>J. P. Richters, J. Kalden, M. Gnauck, C. Ronning, C. P. Dietrich, H. von Wenckstern, M. Grundmann, J. Gutowski, and T. Voss, "Modal gain and its diameter dependence in single-ZnO micro- and nanowires," *Semicond. Sci. Technol.* **27**, 015005 (2012).
- <sup>200</sup>K. L. Shaklee and R. F. Leheny, "Direct determination of optical gain in semiconductor crystals," *Appl. Phys. Lett.* **18**, 475–477 (1971).
- <sup>201</sup>K. L. Shaklee, R. E. Nahory, and R. F. Leheny, "Optical gain in semiconductors," *J. Lumin.* **7**, 284–309 (1973).
- <sup>202</sup>P. L. Knight and A. Miller, *Vertical-Cavity Surface Emitting Laser* (Springer-Verlag, Berlin, 1999).
- <sup>203</sup>H. Yan, J. Johnson, M. Law, R. He, K. Knutsen, J. R. McKinney, J. Pham, R. Saykally, and P. Yang, "ZnO nanoribbon microcavity lasers," *Adv. Mater.* **15**, 1907–1911 (2003).
- <sup>204</sup>B. Zou, R. Liu, F. Wang, A. Pan, L. Cao, and Z. L. Wang, "Lasing mechanism of ZnO nanowires/nanobelts at room temperature," *J. Phys. Chem. B* **110**(26), 12865–12873 (2006).
- <sup>205</sup>J. M. Szarko, J. K. Song, C. W. Blackledge, I. Swart, S. R. Leone, S. Li, and Y. Zhao, "Optical injection probing of single ZnO tetrapod lasers," *Chem. Phys. Lett.* **404**, 171–176 (2005).
- <sup>206</sup>M. A. M. Versteegh, D. Vanmaekelbergh, and J. I. Dijkhuis, "Room-temperature laser emission of ZnO nanowires explained by many-body theory," *Phys. Rev. Lett.* **108**, 157402 (2012).
- <sup>207</sup>C. Johnson, H. Yan, P. Yang, and R. J. Saykally, "Optical cavity effects in ZnO nanowire lasers and waveguides," *J. Phys. Chem. B* **107**, 8816–8828 (2003).
- <sup>208</sup>M. A. Zimmler, J. Bao, F. Capasso, S. Müller, and C. Ronning, "Laser action in nanowires: Observation of the transition from amplified spontaneous emission to laser oscillation," *Appl. Phys. Lett.* **93**, 051101 (2008).
- <sup>209</sup>V. V. Zalamai, V. V. Ursaki, I. M. Tiginyanu, A. Burlacu, E. V. Rusu, C. Klingshirn, J. Fallert, J. Sartor, and H. Kalt, "Impact of size upon lasing in ZnO microtetrapods," *Appl. Phys. B* **99**, 215–222 (2010).
- <sup>210</sup>J. C. Johnson, H. Yan, R. D. Schaller, L. H. Haber, R. J. Saykally, and P. Yang, "Single nanowire lasers," *J. Phys. Chem. B* **105**, 11387–11390 (2001).
- <sup>211</sup>A. E. Siegman, *Lasers* (University Science Books, Sausalito, 1986), Chap. 13.
- <sup>212</sup>T. P. H. Sidropoulos, R. Röder, S. Geburt, O. Hess, S. A. Maier, C. Ronning, and R. F. Oulton, "Ultrafast plasmonic nanowire lasers near the surface plasmon frequency," *Nat. Phys.* **10**, 870–876 (2014).
- <sup>213</sup>J. Lu, M. Jiang, M. Wei, C. Xu, S. Wang, Z. Zhu, F. Qin, Z. Shi, and C. Pan, "Plasmon-induced accelerated exciton recombination dynamics in ZnO/Ag hybrid nanolasers," *ACS Photonics* **4**, 2419–2424 (2017).
- <sup>214</sup>Y.-J. Lu, J. Kim, H.-Y. Chen, C. Wu, N. Dabidian, C. E. Sanders, C.-Y. Wang, M.-Y. Lu, B.-H. Li, X. Qiu, W.-H. Chang, L.-J. Chen, G. Shvets, C.-K. Shih, and S. Gwo, "Plasmonic nanolaser using epitaxially grown silver film," *Science* **337**, 450–453 (2012).
- <sup>215</sup>J. Li, M. Jiang, C. Xu, Y. Wang, Y. Lin, J. Lu, and Z. Shi, "Plasmon coupled Fabry-Perot lasing enhancement in graphene/ZnO hybrid microcavity," *Sci. Rep.* **5**, 9263 (2015).
- <sup>216</sup>Y.-H. Chou, K.-B. Hong, C.-T. Chang, T.-C. Chang, Z.-T. Huang, P.-J. Cheng, J.-H. Yang, M.-H. Lin, T.-R. Lin, K.-P. Chen, S. Gwo, and T.-C. Lu, "Ultra-compact pseudowedge plasmonic lasers and laser arrays," *Nano Lett.* **18**(2), 747–753 (2018).
- <sup>217</sup>S. Chu, G. Wang, W. Zhou, Y. Lin, L. Chernyak, J. Zhao, J. Kong, L. Li, J. Ren, and J. Liu, "Electrically pumped waveguide lasing from ZnO nanowires," *Nat. Nanotechnol.* **6**, 506–510 (2011).
- <sup>218</sup>J. Y. Zhang, Q. F. Zhang, T. S. Deng, and J. L. Wu, "Electrically driven ultraviolet lasing behavior from phosphorus-doped pZnO nanonail array/n-Si heterojunction," *Appl. Phys. Lett.* **95**, 211107 (2009).
- <sup>219</sup>X. Duan, Y. Huang, R. Agarwal, and C. M. Lieber, "Single nanowire electrically driven lasers," *Nature* **421**, 241–245 (2003).
- <sup>220</sup>K. H. Li, X. Liu, Q. Wang, S. Zhao, and Z. Mi, "Ultralowthreshold electrically injected AlGaIn nanowire ultraviolet lasers on Si operating at low temperature," *Nat. Nanotechnol.* **10**, 140–144 (2015).
- <sup>221</sup>S. Zhao, S. Y. Woo, M. Bugnet, X. Liu, J. Kang, G. A. Botton, and Z. Mi, "Three-dimensional quantum confinement of charge carriers in self-organized AlGaIn nanowires: A viable route to electrically injected deep ultraviolet lasers," *Nano Lett.* **15**, 7801–7807 (2015).
- <sup>222</sup>J. Wiersig, "Hexagonal dielectric resonators and microcrystal lasers," *Phys. Rev. A* **67**, 023807 (2003).
- <sup>223</sup>C. P. Dietrich, M. Lange, T. Böntgen, and M. Grundmann, "The corner effect in hexagonal whispering gallery microresonators," *Appl. Phys. Lett.* **101**, 141116 (2012).
- <sup>224</sup>J. Dai, C. X. Xu, K. Zheng, C. G. Lv, and Y. P. Cui, "Whispering gallery-mode lasing in ZnO microrods at room temperature," *Appl. Phys. Lett.* **95**, 241110 (2009).
- <sup>225</sup>R. Chen, B. Ling, X. Wei Sun, and H. D. Sun, "Room temperature excitonic whispering gallery mode lasing from high-quality hexagonal ZnO microdisks," *Adv. Mater.* **23**, 2199–2204 (2011).
- <sup>226</sup>J. Dai, C. X. Xu, P. Wu, J. Y. Guo, Z. H. Li, and Z. L. Shi, "Exciton and electron-hole plasma lasing in ZnO dodecagonal whispering-gallery-mode microcavities at room temperature," *Appl. Phys. Lett.* **97**, 011101 (2010).
- <sup>227</sup>J. Dai, C. X. Xu, and X. W. Sun, "ZnO-microrod/p-GaN heterostructured whispering-gallery-mode microlaser diodes," *Adv. Mater.* **23**, 4115–4119 (2011).
- <sup>228</sup>Q. Zhang, J. Qi, X. Li, F. Yi, Z. Wang, and Y. Zhang, "Electrically pumped lasing from single ZnO micro/nanowire and poly(3,4-ethylenedioxythiophene): Poly(styrene-sulfonate) hybrid heterostructures," *Appl. Phys. Lett.* **101**, 043119 (2012).
- <sup>229</sup>X. Zhou, M. Jiang, K. Xu, M. Liu, S. Sha, S. Cao, C. Kan, and D. N. Shi, "Electrically driven single microwire-based single-mode microlaser," *Light: Sci. Appl.* **11**, 198 (2022).
- <sup>230</sup>C. F. Klingshirn, *Semiconductor Optics*, 2nd ed. (Springer, Berlin, 2005).
- <sup>231</sup>C. Klingshirn, R. Hauschild, J. Fallert, and H. Kalt, "Room-temperature stimulated emission of ZnO: Alternatives to excitonic lasing," *Phys. Rev. B* **75**, 115203 (2007).
- <sup>232</sup>M. A. M. Versteegh, T. Kuis, H. T. C. Stoof, and J. I. Dijkhuis, "Ultrafast screening and carrier dynamics in ZnO: Theory and experiment," *Phys. Rev. B* **84**, 035207 (2011).
- <sup>233</sup>E. Hendry, M. Koeberg, and M. Bonn, "Exciton and electron-hole plasma formation dynamics in ZnO," *Phys. Rev. B* **76**, 045214 (2007).
- <sup>234</sup>A. Schleife, C. Rödl, F. Fuchs, K. Hannewald, and F. Bechstedt, "Optical absorption in degenerately doped semiconductors: Mott transition or mahan excitons?," *Phys. Rev. Lett.* **107**, 236405 (2011).
- <sup>235</sup>M. Wille, C. Sturm, T. Michalsky, R. Röder, C. Ronning, R. Schmidt-Grund, and M. Grundmann, "Carrier density driven lasing dynamics in ZnO nanowires," *Nanotechnology* **27**, 225702 (2016).
- <sup>236</sup>C. B. à la Guillaume, J.-M. Debever, and F. Salvan, "Radiative recombination in highly excited CdS," *Phys. Rev.* **177**, 567–580 (1969).
- <sup>237</sup>M. Hvam, "Exciton-exciton interaction and laser emission in high-purity ZnO," *Solid. State Commun.* **12**, 95–97 (1973).
- <sup>238</sup>J. M. Hvam, "Exciton interaction in photoluminescence from ZnO," *Phys. Status Solidi (B)* **63**, 511–517 (1974).
- <sup>239</sup>C. Klingshirn, "The luminescence of ZnO under high one- and two-quantum excitation," *Phys. Status Solidi (B)* **71**, 547–556 (1975).
- <sup>240</sup>B. Hönerlage, C. Klingshirn, and J. B. Grun, "Spontaneous emission due to exciton-electron scattering in semiconductors," *Phys. Status Solidi (B)* **78**, 599–608 (1976).
- <sup>241</sup>H. Haug and S. Koch, "On the theory of laser action in dense exciton systems," *Phys. Status Solidi (B)* **82**, 531–543 (1977).
- <sup>242</sup>C. Klingshirn and H. Haug, "Optical properties of highly excited direct gap semiconductors," *Phys. Rep.* **70**, 315–398 (1981).
- <sup>243</sup>I. Pelant and J. Valenta, *Luminescence Spectroscopy of Semiconductors* (Oxford University Press, Oxford, 2012).
- <sup>244</sup>H. Priller, J. Brückner, T. Gruber, C. Klingshirn, H. Kalt, A. Waag, H. J. Ko, and T. Yao, "Comparison of linear and nonlinear optical spectra of various ZnO epitaxial layers and of bulk material obtained by different experimental techniques," *Phys. Status Solidi (B)* **241**, 587–590 (2004).

- <sup>245</sup>R. Matsuzaki, H. Soma, K. Fukuoka, K. Kodama, A. Asahara, T. Suemoto, Y. Adachi, and T. Uchino, "Purely excitonic lasing in ZnO microcrystals: Temperature-induced transition between exciton-exciton and exciton-electron scattering," *Phys. Rev. B* **96**, 125306 (2017).
- <sup>246</sup>S. Fujii, Y. Adachi, and T. Uchino, "Excitonic stimulated emission from  $Mg_xZn_{1-x}O$  films due to enhanced exciton binding energy," *Phys. Rev. B* **102**, 075204 (2020).
- <sup>247</sup>R. Zimmermann, "Nonlinear optics and the mott transition in semiconductors," *Phys. Status Solidi (B)* **146**, 371–384 (1988).
- <sup>248</sup>M. Kira and S. W. Koch, "Many-body correlations and excitonic effects in semiconductor spectroscopy," *Prog. Quantum Electron.* **30**, 155–296 (2006).
- <sup>249</sup>A. Walsh, J. L. F. Da Silva, and S.-H. Wei, "Origins of band-gap renormalization in degenerately doped semiconductors," *Phys. Rev. B* **78**, 075211 (2008).
- <sup>250</sup>B. E. Sernelius, K.-F. Berggren, Z.-C. Jin, I. Hamberg, and C. G. Granqvist, "Band-gap tailoring of ZnO by means of heavy Al doping," *Phys. Rev. B* **37**, 10244–10248 (1988).
- <sup>251</sup>S. C. Jain, J. M. McGregor, and D. J. Roulston, "Band-gap narrowing in novel III-V semiconductors," *J. Appl. Phys.* **68**, 3747–3749 (1990).
- <sup>252</sup>J. A. Sans, J. F. Sánchez-Royo, A. Segura, G. Tobias, and E. Canadell, "Chemical effects on the optical band-gap of heavily doped  $ZnO:M_{III}$  ( $M = Al, Ga, In$ ): An investigation by means of photoelectron spectroscopy, optical measurements under pressure, and band structure calculations," *Phys. Rev. B* **79**, 195105 (2009).
- <sup>253</sup>E. Burstein, "Anomalous optical absorption limit in InSb," *Phys. Rev.* **93**, 632–633 (1954).
- <sup>254</sup>T. S. Moss, *Optical Properties of Semiconductors* (Butterworths, London, 1961).
- <sup>255</sup>G. D. Mahan, "Excitons in degenerate semiconductors," *Phys. Rev.* **153**, 882–889 (1967).
- <sup>256</sup>F. Fuchs, K. Kheng, P. Koidl, and K. Schwarz, "Fermi-edge singularity in degenerate n-type bulk InAs," *Phys. Rev. B* **48**, 7884–7888 (1993).
- <sup>257</sup>M. Feneberg, J. Däubler, K. Thonke, R. Sauer, P. Schley, and R. Goldhahn, "Mahan excitons in degenerate wurtzite InN: Photoluminescence spectroscopy and reflectivity measurements," *Phys. Rev. B* **77**, 245207 (2008).
- <sup>258</sup>P. Plochocka-Polack, J. G. Groshaus, M. Rappaport, V. Umansky, Y. Gallais, A. Pinczuk, and I. Bar-Joseph, "Fermi-edge singularity of spin-polarized electrons," *Phys. Rev. Lett.* **98**, 186810 (2007).
- <sup>259</sup>T. Palmieri, E. Baldini, A. Steinhoff, A. Akrap, M. Kollár, E. Horváth, L. Forró, F. Jahnke, and M. Chergui, "Mahan excitons in room-temperature methyllumonium lead bromide perovskites," *Nat. Commun.* **11**, 850 (2020).
- <sup>260</sup>S. Richter, O. Herrfurth, S. Espinoza, M. Rebarz, M. Kloz, J. A. Leveillee, A. Schleife, S. Zollner, M. Grundmann, J. Andreasson, and R. Schmidt-Grund, "Ultrafast dynamics of hot charge carriers in an oxide semiconductor probed by femtosecond spectroscopic ellipsometry," *New J. Phys.* **22**, 083066 (2020).
- <sup>261</sup>M. G. A. Bernard and G. Duraffourg, "Laser conditions in semiconductors," *Phys. Status Solidi (B)* **1**, 699–703 (1961).
- <sup>262</sup>C. Klingshirn, J. Fallert, O. Gogolin, M. Wissinger, R. Hauschild, M. Hauser, H. Kalt, and H. Zhou, "Linear and nonlinear optics, dynamics, and lasing in ZnO bulk and nanostructures," *J. Lumin.* **128**, 792–796 (2008).
- <sup>263</sup>T. Nakamura, K. Firdaus, and S. Adachi, "Electron-hole plasma lasing in a ZnO random laser," *Phys. Rev. B* **86**, 205103 (2012).
- <sup>264</sup>J. Fallert, F. Stelzl, H. Zhou, A. Reiser, K. Thonke, R. Sauer, C. Klingshirn, and H. Kalt, "Lasing dynamics in single ZnO nanorods," *Opt. Express* **16**, 1125 (2008).
- <sup>265</sup>J. C. Johnson, K. P. Knutsen, H. Yan, M. Law, Y. Zhang, P. Yang, and R. J. "Saykally ultrafast carrier dynamics in single ZnO nanowire and nanoribbon lasers," *Nano Lett.* **4**, 197–204 (2004).
- <sup>266</sup>A. B. Djurišić, W. M. Kwok, Y. H. Leung, D. L. Phillips, and W. K. Chan, "Stimulated emission in ZnO nanostructures: A time-resolved study," *J. Phys. Chem. B* **109**, 19228–19233 (2005).
- <sup>267</sup>A. Imamoglu, R. J. Ram, S. Pau, and Y. Yamamoto, "Nonequilibrium condensates and lasers without inversion: Exciton-polariton lasers," *Phys. Rev. A* **53**, 4250–4253 (1996).
- <sup>268</sup>M. D. Fraser, S. Höfling, and Y. Yamamoto, "Physics and applications of exciton-polariton lasers," *Nat. Mater.* **15**, 1049–1052 (2016).
- <sup>269</sup>M. Yamaguchi, K. Kamide, R. Nii, T. Ogawa, and Y. Yamamoto, "Second thresholds in BEC-BCS-laser crossover of exciton-polariton systems," *Phys. Rev. Lett.* **111**, 026404 (2013). Erratum *Phys. Rev. Lett.* **113**, 239902 (2014).
- <sup>270</sup>R. Hauschild, H. Priller, M. Decker, H. Kalt, and C. Klingshirn, "The exciton polariton model and the diffusion of excitons in ZnO analyzed by time-dependent photoluminescence spectroscopy," *Phys. Status Solidi (C)* **3**, 980 (2006).
- <sup>271</sup>L. K. van Vugt, S. Rühle, P. Ravindran, H. C. Gerritsen, L. Kuipers, and D. Vanmaekelbergh, "Exciton polaritons confined in a ZnO nanowire cavity," *Phys. Rev. Lett.* **97**, 147401 (2006).
- <sup>272</sup>J. Dai, C. X. Xu, X. W. Sun, and X. H. Zhang, "Exciton-polariton microphotoluminescence and lasing from ZnO whispering-gallery mode microcavities," *Appl. Phys. Lett.* **98**, 161110 (2011).
- <sup>273</sup>A. Trichet, L. Sun, G. Pavlovic, N. A. Gippius, G. Malpuech, W. Xie, Z. Chen, M. Richard, and L. S. Dang, "One-dimensional ZnO exciton polaritons with negligible thermal broadening at room temperature," *Phys. Rev. B* **83**, 041302(R) (2011).
- <sup>274</sup>W. Xie, H. Dong, S. Zhang, L. Sun, W. Zhou, Y. Ling, J. Lu, X. Shen, and Z. Chen, "Room-temperature polariton parametric scattering driven by a one-dimensional polariton condensate," *Phys. Rev. Lett.* **108**, 166401 (2012).
- <sup>275</sup>A. Trichet, E. Durupt, F. Médard, S. Datta, A. Minguzzi, and M. Richard, "Long-range correlations in a 97% excitonic one-dimensional polariton condensate," *Phys. Rev. B* **88**, 121407(R) (2013).
- <sup>276</sup>C. P. Dietrich, R. Johne, T. Michalsky, C. Sturm, P. Eastham, H. Franke, M. Lange, M. Grundmann, and R. Schmidt-Grund, "Parametric relaxation in whispering gallery mode exciton-polariton condensates," *Phys. Rev. B* **91**, 041202(R) (2015).
- <sup>277</sup>T. Guillet, M. Mexis, J. Levrat, G. Rossbach, C. Brimont, T. Bretagnon, B. Gil, R. Butté, N. Grandjean, L. Orosz, F. Réveret, J. Leymarie, J. Zúñiga-Pérez, M. Leroux, F. Semond, and S. Bouchoule, "Polariton lasing in a hybrid bulk ZnO microcavity," *Appl. Phys. Lett.* **99**, 161104 (2011).
- <sup>278</sup>F. Li, L. Orosz, O. Kamoun, S. Bouchoule, C. Brimont, P. Disseix, T. Guillet, X. Lafosse, M. Leroux, J. Leymarie, M. Mexis, M. Mihailovic, G. Patriarche, F. Réveret, D. Solnyshkov, J. Zuniga-Perez, and G. Malpuech, "From excitonic to photonic polariton condensate in a ZnO-based microcavity," *Phys. Rev. Lett.* **110**, 196406 (2013).
- <sup>279</sup>Y.-Y. Lai, Y.-P. Lan, and T.-C. Lu, "Strong light-matter interaction in ZnO microcavities," *Light: Sci. Appl.* **2**, e76–e76 (2013).
- <sup>280</sup>L. Orosz, F. Réveret, F. Médard, P. Disseix, J. Leymarie, M. Mihailovic, D. Solnyshkov, G. Malpuech, J. Zuniga-Pérez, F. Semond, M. Leroux, S. Bouchoule, X. Lafosse, M. Mexis, C. Brimont, and T. Guillet, "LO-phonon-assisted polariton lasing in a ZnO-based microcavity," *Phys. Rev. B* **85**, 121201(R) (2012).
- <sup>281</sup>O. Jamadi, F. Reveret, P. Disseix, F. Medard, J. Leymarie, A. Moreau, D. Solnyshkov, C. Deparis, M. Leroux, E. Cambil, S. Bouchoule, J. Zuniga-Perez, and G. Malpuech, "Edge-emitting polariton laser and amplifier based on a ZnO waveguide," *Light: Sci. Appl.* **7**, 82 (2018).
- <sup>282</sup>J.-W. Kang, B. Song, W. Liu, S.-J. Park, R. Agarwal, and C.-H. Cho, "Room temperature polariton lasing in quantum heterostructure nanocavities," *Sci. Adv.* **5**, eaau9338 (2019).
- <sup>283</sup>J. P. Reithmaier, G. Şek, A. Löffler, C. Hofmann, S. Kuhn, S. Reitzenstein, L. V. Keldysh, V. D. Kulakovskii, T. L. Reinecke, and A. Forchel, "Strong coupling in a single quantum dot-semiconductor microcavity system," *Nature* **432**, 197–200 (2004).
- <sup>284</sup>Y.-Y. Lai, Y.-H. Chou, Y.-P. Lan, T.-C. Lu, S.-C. Wang, and Y. Yamamoto, "Crossover from polariton lasing to exciton lasing in a strongly coupled ZnO microcavity," *Sci. Rep.* **6**, 20581 (2016).
- <sup>285</sup>D. Xu, W. Xie, W. Liu, J. Wang, L. Zhang, Y. Wang, S. Zhang, L. Sun, X. Shen, and Z. Chen, "Polariton lasing in a ZnO microwire above 450 K," *Appl. Phys. Lett.* **104**, 082101 (2014).
- <sup>286</sup>K. Shima, K. Furusawa, and S. F. Chichibu, "Room-temperature cavity-polaritons in planar ZnO microcavities fabricated by a top-down process," *Appl. Phys. Lett.* **117**, 071103 (2020).
- <sup>287</sup>H. Franke, C. Sturm, R. Schmidt-Grund, G. Wagner, and M. Grundmann, "Ballistic propagation of exciton-polariton condensates in a ZnO-based microcavity," *New J. Phys.* **14**, 013037 (2012).
- <sup>288</sup>T. Guillet and C. Brimont, "Polariton condensates at room temperature," *Compt. Rend. Phys.* **17**, 946–956 (2016).